MODEL CALCULATIONS OF RAMAN RESPONSES FOR MULTIBAND IRON-BASED SUPERCONDUCTORS

BY CHRISTOPH SAUER

A thesis submitted to the

Graduate School—New Brunswick

Rutgers, The State University of New Jersey

in partial fulfillment of the requirements

for the degree of

Master of Science

Graduate Program in Physics and Astronomy

Written under the direction of

Prof. Girsh Blumberg

and approved by

_____

_____

_____

New Brunswick, New Jersey

October, 2009

ABSTRACT OF THE THESIS

Model calculations of Raman responses for multiband iron-based superconductors

by Christoph Sauer

Thesis Director: Prof. Girsh Blumberg

In this thesis I compute Raman responses for a free electron band structure model based on ARPES measurements on multiband iron-based superconductors. First a constant and then a k-dependent superconducting gap is used. Applying an effective mass approximation leaves A_{1g} and B_{2g} as the only nonvanishing symmetry channels. In the latter only one band contributes and a square root singularity is observed for a constant gap. The k-dependent gap leads to a threshold-*log*-singularity structure. The unscreened A_{1g} channel shows the same features but all bands contribute and sum up. The screened single band A_{1g} response vanishes for both gaps. Two band responses with the same constant gap are perfectly screened with identical Raman verteces, unscreened with opposite signs and equal mass ratios and partially screened in all other cases. With two different constant gaps the singularities are removed and a dome-like shape appears except for the vanishing case of equal verteces. The n-band response consists of a sum of two band terms normalized by all n bands and the singularities corresponding to all uniquely present gap values are removed. With the k-dependent gap the singularities are removed and a dome-like shape appears in all combinations of two band responses and in the response for all bands. The dome in the response for all bands shows a flat continuum in between a threshold and a sharp peak produced by the two band terms containing bands of opposite signs.

Acknowledgements

First of all I would like to thank Prof Girsh Blumberg for being such a great advisor over the whole period of time I was working on this thesis. I highly appreciated the numerous discussions about superconductivity, Raman spectroscopy and scientific working in general. Especially the constant fight against Mathematica would have been a lot harder without your permanent supply of valuable tips and tricks. It seems to me that in the end we are looking at a satisfying outcome of a well executed plan B.

Furthermore I would like to thank everybody who is involved in the "Amerika Progamm" of the University Würzburg namely Prof Assad and Ursula Shahmary in Würzburg and Prof Ransome and Shirley Hinds at Rutgers. Without your work in all kinds of different issues this exchange program would not be possible. Moreover I would like to show gratitude to the "Deutscher Akademischer Auslandsdienst" (DAAD) for the financial support that made the expensive stay in the United States affordable for me.

Further thanks goes out to the two other members of team Würzburg at Rutgers, Fabian and Heiko, for representing a stable ground to start from in this new world and for making so many new experiences with me. Also thanks to my other compatriots Jessica, Felix, Florin and Fabian for taking part in the German invasion. A big thanks to all the people I met in New Jersey, you made that stay very enjoyable on so many occasions and you certainly extended my mind with new ideas and ways of thinking. Thanks to all the visitors from back home that brought a little bit of home with them, spiritually as well as materially, especially Andi and Fabienne. Andi, I hope the BBQ season will reach its peak when I return. Moreover I would like to show gratitude to all the people who were constantly communicating with me through all kinds of possible ways: My whole family, especially my little sister Nadja and all my friends. Metro, you seem to be an infinite source of mischief and new musical experiences, thanks for the exclusive mixes and I can't wait to have the next

Dedication

To those who prefer to see borders from both sides.

Table of Contents

List of Tables

List of Figures

Chapter 1

Introduction

With the discovery of superconductivity in a mercury probe by H. Kamerlingh Onnes in 1911 [1], only three years after he managed to liquefy helium, a whole new field of physics opened up. Below 4.2K, now reachable with the new refrigeration technique, the specimen showed a vanishing DC electrical resistance and a persistent current could be observed in a loop which he graphically demonstrated later by carrying such a superconducting loop from Leiden to Cambridge [2]. In 1933 another characterizing feature of superconductors was discovered by W. Meissner and R. Ochsenfeld [3]. They found that superconducting specimen act like perfect diamagnets, so that magnetic fields cannot exist in the bulk and can only penetrate a superconductor up to a certain penetration length λ. One year later C. J. Gorter and H. G. B. Casimir [4, 5] came up with a phenomenological two fluid model seperating the electron fluid in a superconducting and a normal part and in 1935 the London-theory [6, 7] was published. In this famous phenomenological theory Fritz and Hans London explained the electrodynamic properties of the superconducting state on the assumption that the diamagnetic rather than the electric aspects are basic. This theory was extended in 1950 by V. L. Ginzburg and L. D. Landau [8] who allowed the super fluid density to vary in space and introduced the coherence length $\xi(T)$ as an important length scale and the Ginzburg-Landau-parameter κ as the quotient of $\lambda(T)$ and $\xi(T)$. In the same year E. Maxwell [9] and, independently, C. A. Reynolds [10] discovered the isotope effect which showed that electron-lattice interactions were important for the microscopic mechanism of superconductivity. This supported the theory by H. Fröhlich [11] which was based on those interactions and yielded the isotope effect but was unable to obtain superconducting properties. A nonlocal generalization of the London-theory was done by A. B. Pippard [12] in 1953. Based on experimental facts he emphasized the importance of a

coherence length ξ_0 which determines the distance from a certain point which is influenced by a perturbation at that point. Then in 1955 J. Bardeen [13, 14] showed that this nonlocal behavior follows from an energy gap model. One year later L. N. Cooper [15] managed to derive the formation of a bound state within an isolated pair model including an attractive interaction between the pair of electrons. Then finally, almost 50 years after the discovery of superconductivity, a microscopic theory was published by J. Bardeen, L. N. Cooper and J. R. Schrieffer [16, 17] named the BCS-theory after the names of its inventors. Based on the pairing of two electrons, a Cooper-pair, by an attractive interaction mediated by phonons leading to a split off of the superconducting ground state by an energy gap this theory explained almost every aspect of superconductivity observed so far. After that in the same year theoretical investigations of A. A. Abrikosov [18] on the Ginzburg-Landau-theory (GL-theory) assuming κ to be large lead to a different behavior of the superconductor in an external magnetic field and Abrikosov called such materials type II superconductors. In 1959 L. P. Gor'kov [19] managed to derive the GL-theory from the microscopic BCS-Theory with the GL wave function Ψ being proportional to the BCS order parameter Δ near the transition temperature T_c. This was extended to all temperatures under suitable conditions by N. R. Werthamer [20] and L. Tewordt [21] in 1963. Another important feature of superconductivity was discovered in 1961 by B. S. Deaver and W. M. Fairbank [22] and independently by R. Doll and M. Näbauer [23] who observed the quantization of magnetic flux previously introduced by F. London [24]. The prediction of an entirely new aspect was made in the following year by B.D. Josephson [25]. He stated that between a superconductor-isolator-superconductor junction a DC current should be observed without a bias voltage which was later used by tunneling spectroscopic measurements of the density of states. Furthermore he predicted an AC current when a bias voltage is applied to the junction which lead to high precision measurements of the fundamental constants of the electrons charge e and Planck constant h and the currently used definition of the unit Volt. Despite its complexity and richness of different applications the field of superconductivity became less exciting within the following two decades and part of that was the problem of the still quite low transition temperatures with the record (at that time) of $26K$ obtained by J. R. Galaver in 1973 [26]. The discovery of High-T_c superconductivity in the cuprates in

1986 by Bednorz and Müller [27] can therefore be seen as a revolution in the field. Quickly reaching temperatures above the boiling point of liquid N_2, up to about $130K$ and even higher under pressure, a whole new world of applications opened up. Recently a new family of interesting materials also showing superconducting behavior was found with iron-based superconductors [28] with transition temperatures up to $56K$ [29]. The similarities of this material to the cuprates and its own unique features gave rise to tremendous research efforts and raised hope to finally solve the so far unsolved problem of the microscopic mechanism responsible for high temperature superconductivity.

In this thesis model calculations of Raman responses will be performed with a free electron band structure model of a multisheeted Fermi surface based on data obtained by Angular Resolved Photo Emission Spectroscopy (ARPES) on a member of the iron-based superconductor family. With the assumption of a constant superconducting gap parameter an analytical treatment will be possible and single band, two band and n-band responses including screening effects for the fully symmetric A_{1g} channel will be discussed. The results from the constant gap case will then be used to explain the numerically computed Raman responses with a k-dependent gap of extended s-wave symmetry together with a simplifying model of a gap with just an angular dependence. Finally the expected Raman response of the entire first Brillouin zone will be calculated for both gaps which will serve as a help for interpreting data of electronic Raman scattering on this material in the future. Raman scattering experiments might be able to give clear evidence for the nature of the gap parameter which is crucial for revealing the superconducting pairing mechanism present in these materials.

This thesis will start with an overview of the phenomenology and theory of superconductivity together with examples of experiments verifying the microscopic BCS theory. Then the lattice structure of the iron based superconductors will be discussed and a classification of the different families will be done. Moreover the electronic structure with an emphasis on the superconducting gap will be presented and a brief summary of the physical properties including the phase diagram will be given. After that the theory of Raman scattering will be discussed with a short development of the general theory followed by the application of the effective mass approximation for the Raman vertex and a specialization of the theory

on electronic Raman scattering on superconductors. Examples for electronic Raman spectroscopy on different kinds of superconductors done in the past will also be shown. Then the original work of this thesis will be presented. It consist of model calculations of Raman responses of a multiband iron-based superconductor in a free electron model with a constant and an angular dependent gap.

Chapter 2

Superconductivity

This chapter is an overview of superconductivity containing phenomenology, theories and examples for experimental verification of the BCS-theory. In the first part the unique electromagnetic properties of superconductors will be summarized and the difference between type I and type II superconductors will be explained. After that the basic aspects of high temperature superconductors will be presented. The second part will start with a discussion of the thermodynamics of superconductors followed by a short overview of the different phenomenological theories. Then the BCS-theory, the microscopic theory of superconductivity, will be presented briefly. The third part will show two experimental verifications of the BCS-theory namely original measurements of the superconducting density of states by tunneling spectroscopy and a verification of the coherence factors by nuclear spin relaxation.

2.1 Phenomenology

2.1.1 Electromagnetic properties

The probably most characteristic feature of superconductivity and therefore responsible for its name is the perfect conductivity or in other words the vanishing resistivity below the transition temperature T_c. As shown in Fig. 2.1 the DC resistivity ρ_{DC} drops within a tiny temperature interval to a vanishingly small value. In a superconducting loop a persistent current for over a year has been observed and with nuclear resonance measurements of the produced magnetic field the decay time of the current was found to be at the order of 10^5 years [30]. So the resistivity is in fact zero and superconductors are actually perfect conductors. Below T_c the AC resistivity, also shown in Fig. 2.1, is vanishing as well as long as one does not apply a voltage of frequency larger than ω_g. Above this certain frequency,
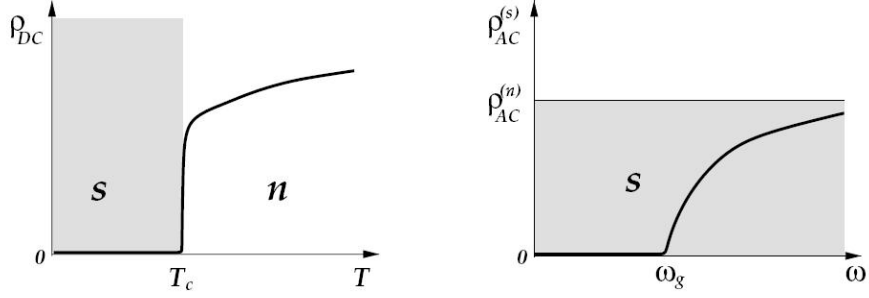
Figure 2.1: Resistivity of a superconductor in the superconducting (shaded) and the normal state (unshaded) denoted with s and n respectively. **Left:** DC resistivity as a function of temperature. Approaching the critical temperature from above the resistivity suddenly drops to zero. **Right:** AC resistivity as a function of frequency. Below a certain frequency ω_g the resistivity is vanishingly small and converges to the normal resistivity for higher frequencies. Taken from [31].

related to the critical temperature by $\hbar\omega_g \approx 3.5 k_B T_c$ [31], the superconducting AC resistance $\rho_{AC}^{(s)}$ is approaching its normal value $\rho_{AC}^{(n)}$, visible as the horizontal line in Fig. 2.1, with increasing frequency. This points towards an energy gap dividing the superconducting and the normal state which has to be overcome before a scattering mechanism leading to resistance is possible. A superconductor undergoes the phase transition to the normal state not only if it is heated up above its critical temperature but also if a sufficiently large magnetic field H_c is applied. Thus magnetism also plays an important role.

Below the critical magnetic field H_c a superconductor acts like a perfect diamagnet expelling a magnetic field completely from its bulk region. This is done by dissipationless surface currents that produce a magnetic field shielding the interior of the specimen. So magnetic fields do only penetrate superconductors up to a characteristic length λ and are eliminated further inside by a negative magnetization $M = 4\pi m$ [31], see Fig. 2.2 left. The exclusion of the magnetic field is influenced by the geometry of the specimen and it can happen that superconductivity only breaks down in certain regions while others stay superconducting, called the intermediate state. Those areas extend over macroscopic scales and changes in magnetization happen abruptly since they are coupled to a phase transition. The preceding behavior in a magnetic field is observed in so called type I superconductors which exhibit a small penetration depth λ and a rather long coherence length ξ. The latter is a length scale which determines the ability of the superconducting electrons to react on
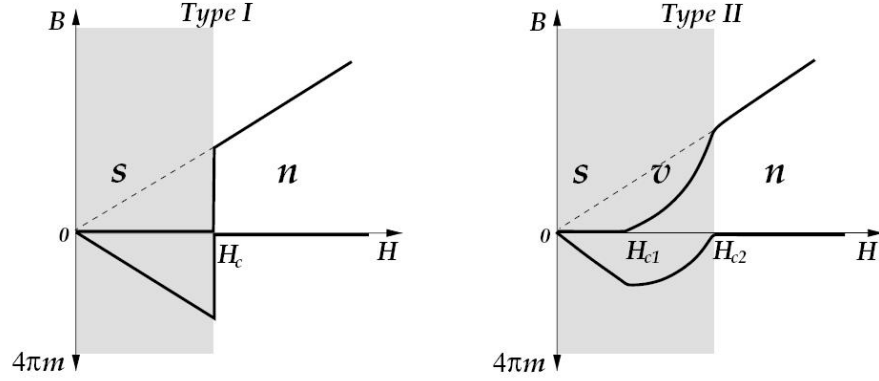
Figure 2.2: Magnetic field B and magnetization $M = 4\pi m$ inside type I and type II super-conductors as a function of external field H in the superconducting (shaded) and normal (unshaded) state denoted by s and n respectively. **Left:** In a type I superconductor total shielding of H by magnetization is observed up to the critical field H_c and completely breaks down above. **Right:** In a type II superconductor the magnetization shields the external field only until a lower critical field H_{c1} is reached. Then the external field partially pene-trates the superconductor which is now in the vortex state denoted by v. Superconductivity breaks down above the upper critical field H_{c2} and total penetration occurs. Taken from [31].

a perturbation as well as the distance of strong correlations stabilizing superconductivity and is discussed in detail later on in Pippard's non local theory and the Ginzburg-Landau Theory. The important thing at this point is only the size of the quotient of these two length scales $\kappa = \lambda/\xi$ called the Ginzburg-Landau Parameter. If it is small the surface energy of a superconducting-normal interface is positive, the surface will therefore be minimized and the superconductor is of type I. If it gets large, $\kappa > 1/\sqrt{2}$ as shown by Abrikosov [18], the surface energy will get negative, the formation of superconducting-normal interface will be energetically favorable and a different behavior will be observed. Such superconductors are called type II and above a certain applied magnetic field H_{c1} the external field starts to penetrate the specimen. This state is called vortex state and consists of vorteces containing a microscopic cylindrical normal core region in which the external magnetic field is nonzero. Such cores contain exactly one flux quantum $\Phi_0 = hc/2e$ [30] and form a triangular lattice on a plane perpendicular to the lines. The superconductivity breaks down completely at a larger field H_{c2} and the external field completely penetrates the specimen, see Fig. 2.2 right.
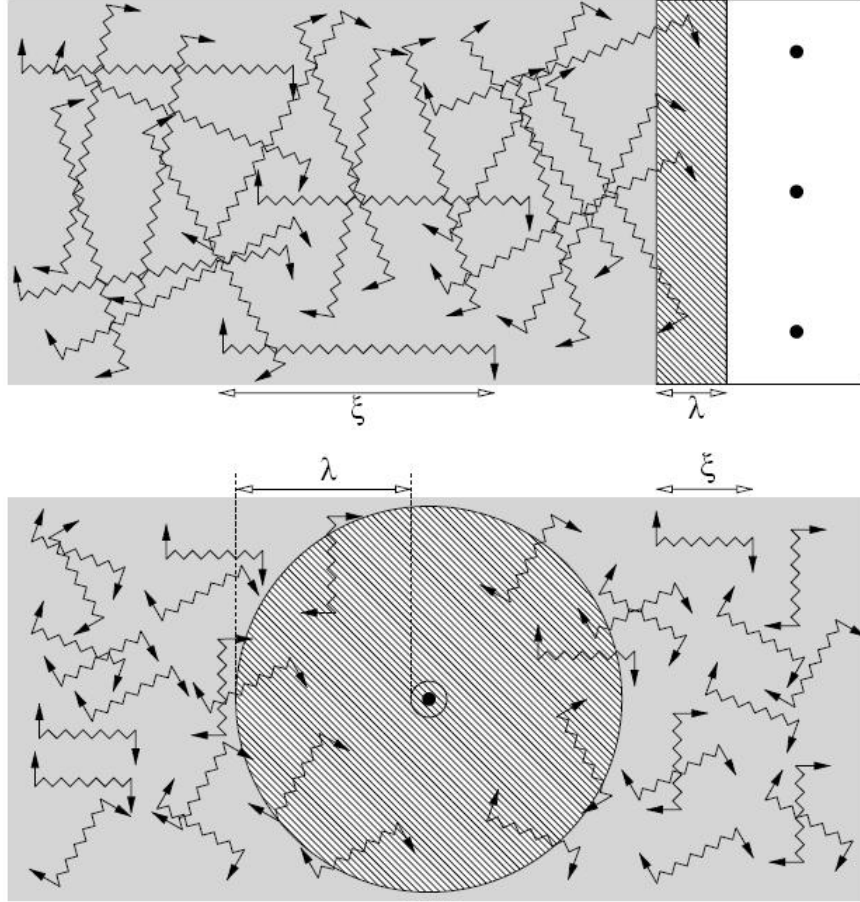
Figure 2.3: Comparison of the penetration depth λ and coherence length ξ in type I and type II superconductors and their consequences on magnetic field penetration. The shaded areas represent the superconducting and the white areas the normal phase. In the dashed area the magnetic field decays to zero from the normal to the superconducting phase and the density of superconducting electrons decays to zero in the opposite direction. Magnetic field lines are shown as black dots. **Upper panel:** A typical type I superconductor with ξ being larger than λ causing a superconducting phase that is too rigid to shield the magnetic field inside the specimen so it is energetically favourable to exclude it. **Lower panel:** Now λ is larger than ξ characteristic for a type II superconductor resulting in a superconducting phase nimble enough to shield the magnetic field surrounded by a normal area inside the bulk of the probe. Taken from [31].

In Fig. 2.3 a heuristic explanation of the microscopic causes for this behavior is displayed. The upper part shows the total exclusion of the magnetic field in a type I superconductor with a small Ginzburg-Landau Parameter κ and thus ξ being larger than λ. The coherence length ξ can be seen as the distance between two correlated electrons that are responsible for the superconducting behavior. (They are called cooper pairs and are discussed extensively in the BCS-Theory section.) Therefore the superconducting electron fluid is not flexible enough to react on perturbations, like a magnetic field, on scales smaller than ξ. So with λ being smaller than that flexibility scale the magnetic field can not be effectively shielded inside the specimen and it is energetically favorable to completely exclude it. In the lower part the situation is reversed with ξ being smaller than λ. This results in a superconducting condensate flexible enough to shield the magnetic field in the bulk region and magnetic field lines may penetrate the superconductor. This is now energetically favorable since bending the field lines around the specimen is related to a cost of energy.

The above mentioned flux quantization can also be observed in a superconducting loop carrying a current. The trapped flux within the loop can only take integer values of Φ_0 which can be explained by the phase coherence of the superconducting condensate. As it will be seen in the following theoretical discussions this turns out to be a real macroscopic quantum phenomenon with a large number of quantum particles occupying a single state.

2.1.2 High temperature superconductors

Beside the just discussed type I and type II superconductors composed of elementary metals or alloys of metals there are much more complex materials displaying superconducting behavior called high temperature superconductors. While the previous two could not exceed transition temperatures of 30K the high T_c materials rapidly reached T_c's of 130K and above. The first discovered high temperature superconductor was a mixed oxide of lanthanum, barium and copper called LBCO [27] having a transition temperature of about 35K. A huge jump in T_c was made by the discovery of $Y_1Ba_2Cu_3O_{7-\delta}$ (YBCO) a so called "123"-material with a T_c=93K [32]. Even higher T_c's were found in mixed oxides of bismuth, strontium, calcium and copper (BSCCO) [33] and mixed oxide of thallium, barium, calcium and copper (TBCCO) [34] with T_c's of about $110K$ and $130K$ respectively. The common feature of all

those materials are the CuO_2 planes which most probably dominate the superconducting behavior. Their number varies within the different structures and the "123"-materials have an additional CuO chains that influence the electron density in the planes [30]. In between those planes are block layers of the different mentioned elements serving as charge carrier reservoirs donating holes or electrons to the copper oxide planes. Two examples of such superconducting cuprates are shown in Fig. 2.4 one of them of the hole-doped the other one of the electron doped type. With the lattice constants in the ab-plane (copper oxide plane) being much smaller than the lattice constant in the perpendicular c-direction these materials are highly anisotropic and they can be seen as essentially two-dimensional in their physical properties.
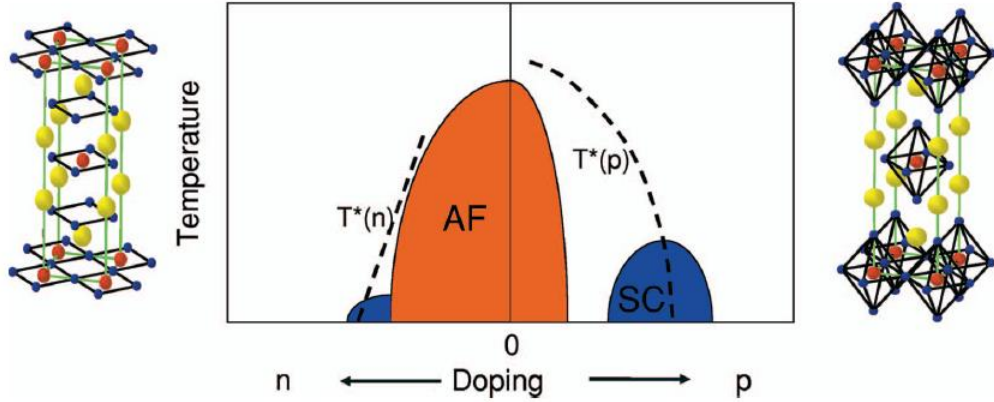
Figure 2.4: Examples for the lattice structure of the high temperature superconducting cuprates together with a schematic phase diagram. The colors symbolize Cu: red; O: blue; La,Sr and Nd,Ce: yellow. On the left hand side $Nd_{2-x}Ce_xCuO_4$ is shown as an example for an electron-doped (n) compound. It crystallizes in the T' structure in which the top and bottom O-atoms are missing in the ocrahedra. The displayed example for a hole-doped (p) compound is $La_{2-x}Sr_xCuO_4$ crystallizing in T stucture with complete O octahedra. The phase diagram shows antiferromangetic (AF) and superconducting (SC) regions depending on doping as well as on temperature. With higher doping the antiferromagnetic ordering disappears and a superconducting phase is reached at low enough temperatures. In the electron doped case the antiferromagnetism survives up to higher dopings and the super-conducting phase extends over a smaler doping and temperature region than in the hole doped case. The dashed T* curve sybolizes the crossover temperature to the pseudogap regime in the middle. Taken from [35].

The high temperature superconductors show a very interesting phase diagram, see Fig. 2.4, consisting of several different phases with some of them not well understood at the time of this writing. The undoped parent compounds are antiferromagnetic Mott insulators with

one hole per CuO_2 plane and therefore at half filling. With the Cu-3d orbitals being very localized at the Cu sites screening is not effective enough to overcome the repulsive Coulomb force in between the holes at neighboring sites which results in the insulating behavior. The antiferromagnetic ordering is a consequence of a superexchange interaction between two Cu sites. Only if the spins are aligned antiparallel a virtual hopping of the neighboring holes is allowed according to the Pauli exclusion principle and thus this ordering is energetically favorable [36]. The antiferromagnetic 3D long range order gets lost above a Néel temperature of about 300K and disappears quickly with hole doping at lower temperatures. In the electron doped case it breaks down at higher doping levels but in both cases short-ranged antiferromagnetic correlations are still present at high doping levels. So strong electronic correlations are not only present in the undoped case but exist almost over the entire phase diagram [35]. After the the antiferromagnetic phase is destroyed by doping a less understood phase, called pseudogap phase, is observed, shown in Fig. 2.4 between the dashed line and the orange AF-phase. Here the Fermi surface is gaped with the gap evolving continuously into the superconducting gap [36]. At lower temperatures the superconducting phase is reached with a dome shaped form in the phase diagram. On the hole-doped side the dome extends over a larger doping and temperature range than on the electron-doped side and the SC-phase does not directly emerge from the AF-phase. Superconductivity in the cuprates is also caused by electron pairs but the cause of the necessary attractive interaction between those pairs is still not definitely known. Magnetic interactions are a good candidate simply by their vicinity to the superconducting phase in the phase diagram but at this point no total consensus is reached. Furthermore the superconducting gap is highly anisotropic and even nodes in some directions are observed [37, 38]. With in plane coherence lengths of $\xi_{ab} \sim 20$Å, out of plane coherence lengths of $\xi_c \sim 3$Å and penetration depths of $\lambda_{ab} \sim 3000$Å for the hole doped compounds [39, 40] these materials are extreme type II superconductors with huge upper critical magnetic fields H_{c2}. In the electron doped case the coherence length is larger and thus the upper critical fields are smaller which means they are accessible in a laboratory in contrast to those of the hole doped cuprates. The region above the superconducting dome also shows strange behavior and is often referred to as a strange metal phase. Here the Fermi liquid theory, with its one to one correspondence

between the noninteracting Fermi gas and the weakly interacting electron liquid, is unable to describe the observations. This shows that strong correlations must be present and the assumption of weak interaction is inappropriate. With very high doping the strange metal behavior disappears and rather normal metal features are present on both sides of the phase diagram.

2.2 Theory

2.2.1 Thermodynamics

With all the interesting features of the superconducting state mentioned above the question arises why this state is energetically favorable and what happens at the point of the phase transition. Answers based on first physical principles can only be given by the microscopic BCS-Theory but a brief thermodynamical investigation can at least deepen the insight into the properties of the superconducting phase in a more phenomenological way. We start with a simplified model of a superconducting probe of type I in a homogeneous external magnetic field H and a complete magnetization of $M = -\frac{\Omega_s}{4\pi}H$ in the Volume Ω_s of the superconducting part of the specimen. The usual form of the variation of the Gibbs free energy is given by [31]

$$dG = -SdT - MdH \tag{2.1}$$

Taking the temperature to be constant and inserting the above given magnetization the superconducting dG_s becomes

$$dG_s = \frac{\Omega_s}{4\pi}HdH \tag{2.2}$$

Now integrating Eq. (2.2) we obtain for the change in the Gibbs free energy per volume

$$g_s(H) - g_s(0) = \frac{H^2}{8\pi} \tag{2.3}$$

Neglecting the small susceptibility of a normal metal the magnetization $M = 0$ and so the Gibbs free energy is independent of the field

$$g_n(H) = g_n(0) \tag{2.4}$$

Since the superconducting and the normal Gibbs free energy are equal at the critical field we can write using Eq. (2.3)

$$g_n(H_c) = g_s(H_c) = g_s(0) + \frac{H_c^2}{8\pi} \tag{2.5}$$

And inserting Eq. (2.4) leads to

$$g_s(0) - g_n(0) = -\frac{H_c^2}{8\pi} \tag{2.6}$$

Eq. (2.6) shows that there is a finite difference between the Gibbs free energy in the normal and the superconducting state and with the right hand side being negative it is obvious that the superconducting state is energetically favorable at zero magnetic field. The whole argumentation breaks down as soon as either T_c or H_c is reached and the normal state will be realized.
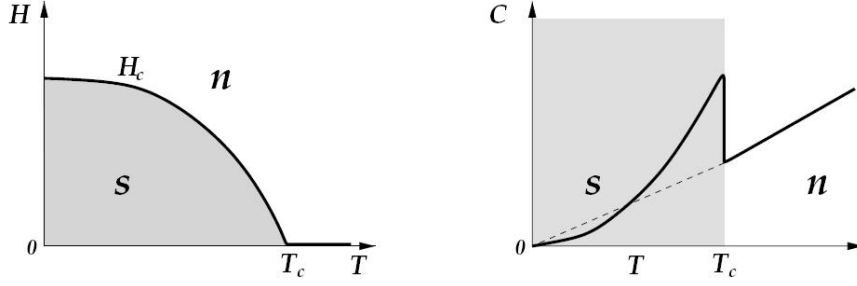
Figure 2.5: Critical magnetic field H_c and specific heat C as functions of temperature. The superconducting (shaded) and normal (unshaded) areas are denoted with s and n respectively. **Left:** H_c shows a square like temperature dependence with a nonvanishing slope at T_c. **Right:** C has a discontinuity at T_c and jumps to a higher value in the superconducting phase. Taken from [31].

Now a specimen consisting of a superconducting an a normal part with a volume of $\Omega = \Omega_s + \Omega_n$ is considered. The magnetic field is given by $B(\mathbf{r}) = H + 4\pi m(\mathbf{r})$ and vanishing in the superconducting part while it is equal to H in the normal part of the probe. This results in a Gibbs free energy of

$$G = F_0 + \frac{1}{8\pi} \int_\Omega [B(\mathbf{r})]^2 d\mathbf{r} - HM = F_0 + \frac{1}{8\pi} H^2 \Omega_n - H \left(-\frac{1}{4\pi} H \Omega_s \right) \tag{2.7}$$

where F_0 stands for the Helmholtz free energy arising from the nonmagnetic contributions [31]. With the nonmagnetic contributions per volume written as $f_0^{(n)}$ and $f_0^{(s)}$ for the

normal and superconducting part respectively and $H = -4\pi m$ in the superconducting part we obtain

$$G = f_0^{(n)}\Omega_n + f_0^{(s)}\Omega_s + \frac{1}{8\pi}H^2\Omega + 2\pi m^2\Omega_s \tag{2.8}$$

In equilibrium the derivative of G with respect to Ω_n and Ω_s is equal to zero because of a balance between the two parts determined by H and T. Furthermore $d\Omega_n = -d\Omega_a$ since the growth of one is the shrinking of the other part. Taking the derivative with respect to either one of the Ω's therefore results in

$$f_0^{(s)} - f_0^{(n)} = -2\pi m^2 = -\frac{1}{8\pi}H^2 \tag{2.9}$$

Now taking the derivative with respect to T together with the standard definition of entropy [31]

$$\left(\frac{\partial f^{(i)}}{\partial T}\right)_{M=0} = -s_0^{(i)} \tag{2.10}$$

with $i = s, n$ leads to

$$s^{(n)} - s^{(s)} = -\frac{H_c}{4\pi}\frac{dH_c}{dT} \tag{2.11}$$

in which the 0 index of the entropies has been dropped. Since Eq. (2.10) only holds true in the superconducting part if $H = H_c$ this had to be inserted to obtain Eq. (2.11). The observed temperature dependence of the critical magnetic field is shown in the left hand side of Fig. 2.5 and can be well described with [31]

$$H_c(T) = H_0\left[1 - \left(\frac{T}{T_c}\right)^2\right] \tag{2.12}$$

where H_0 is a material specific constant. With Eq. (2.12) one can see that $\frac{dH_c}{dT}$ is always negative for finite temperatures. This leads to the right hand side of Eq. (2.11) being positive and thus the entropy being larger in the normal state. In Fig. 2.6 this behavior is displayed for an aluminum probe. Below T_c the entropy in the superconducting phase is always smaller than that in the normal phase so the superconducting phase is more ordered. Another very interesting result can be extracted from Eq. (2.11) when the definition of the latent heat $L = T\Delta s$ is inserted ($\Delta s = s^{(n)} - s^{(s)}$):

$$\frac{dH_c}{dT} = -\frac{4\pi}{H_c}\frac{L}{T} \tag{2.13}$$

As discussed above the right hand side of Eq. (2.13) is negative which makes L a positive quantity since H_c and T are assumed to be positive as well. This means that with a nonvanishing critical magnetic field the superconducting phase transition is of first order since this is associated with a positive latent heat. At T_c these arguments can not be made because $H_c = 0$ at this point. Therefore L has to be zero as well since otherwise Eq. (2.13) would not be fulfilled because of the finite value of the left hand side. A vanishing latent heat at T_c shows that the superconducting phase transition is of second order at this point.
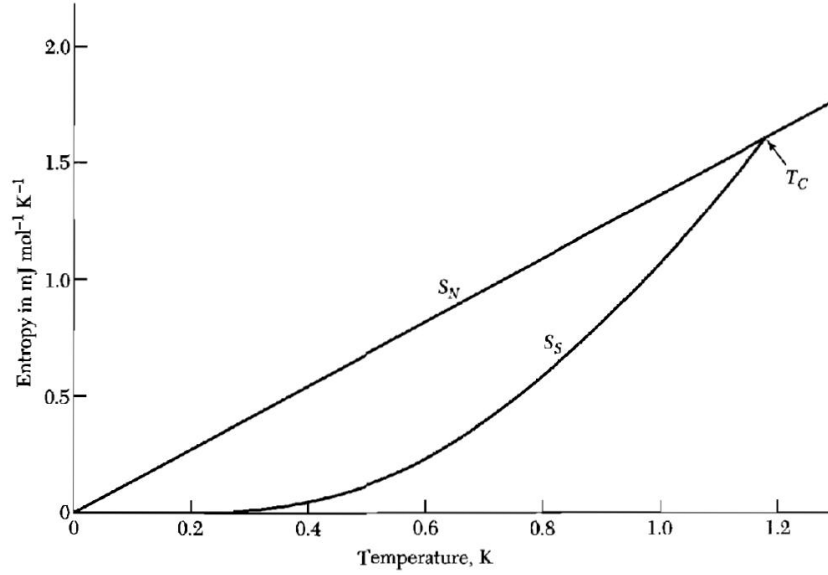
Figure 2.6: Entropy S of aluminum in the superconducting (S_S) and normal (S_N) state. Below T_c the entropy is smaller in the superconducting state which shows that this state is more ordered. No discontinuity is seen at the phase transition. Taken from [41].

Using the standard definition of the specific heat $C = T\frac{dS}{dT}$ one can obtain a temperature dependent expression for the difference of the specific heat per volume between the superconducting and normal state from Eq. (2.11). Differentiating Eq. (2.11) with respect to T and inserting Eq. (2.12) leads to

$$c^{(s)}(T) - c^{(n)}(T) = \frac{H_0^2}{2\pi}\frac{T}{T_c^2}\left[3\left(\frac{T}{T_c}\right)^2 - 1\right] \tag{2.14}$$

and at $T = T_c$ we obtain

$$c^{(s)}(T_c) - c^{(n)}(T_c) = \frac{H_0^2}{\pi T_c} \tag{2.15}$$

Eq. (2.15) shows that there is a discontinuity in the specific heat at the superconducting phase transition. It jumps to a higher value when entering the superconducting phase which

can be seen in the right hand side of Fig. 2.5. From Eq. (2.14) one obtains that in between T_c and $\frac{T_c}{\sqrt{3}}$ the superconducting specific heat keeps being bigger than the normal one and is smaller below $T = \frac{T_c}{\sqrt{3}}$. This behavior is also displayed in the right hand side of Fig. 2.5.

2.2.2 Phenomenological theories

After the discussion of the superconducting phase transition and basic thermodynamic properties in the preceding section a phenomenological approach towards the electrodynamic characteristics of superconductivity will be given now. As a first phenomenological theory the London-Theory by the London brothers [6, 7] was able to describe the observed electromagnetic phenomena of a superconductor. By writing down two basic equations and combining them with the Maxwell equations the observed superconducting properties could be obtained. I will start here with a quantum mechanical motivation given by F. London himself [24] which uses an extension of the momentum with the vector potential $\mathbf{A}$ as a starting point. In quantum mechanics the canonical momentum $\mathbf{p}$ is given by $\mathbf{p} = m\mathbf{v} + \frac{e\mathbf{A}}{c}$ which is called principle of least coupling since for example orbit spin coupling is neglected. Now taking the net momentum to be zero in the absence of an applied external field, according to a famous but unpublished [30] theorem of Bloch, leads to the following expression of the local average velocity:

$$\langle \mathbf{v}_S \rangle = -\frac{e\mathbf{A}}{mc} \tag{2.16}$$

This relates $\langle \mathbf{v}_S \rangle$ to an external field and one could think that the above theorem is violated and Eq. (2.16) does not hold true but the superconducting ground state exhibits a rigidity towards perturbations so that $\langle \mathbf{p} \rangle = 0$ is still the case. The superconducting current density follows as:

$$\mathbf{J}_S = n_S e \langle \mathbf{v}_S \rangle = -\frac{n_S e^2 \mathbf{A}}{mc} = -\frac{\mathbf{A}}{\Lambda c} \tag{2.17}$$

with n_S being the number density of electrons participating in the super-current and $\Lambda = \frac{m}{n_s e^2}$. Super-current conservation requires a proper gauge choice with $\nabla \mathbf{A} = 0$, called the London gauge. Taking the time derivative of both sides and using the fact that $\mathbf{E} = -\frac{1}{c}\frac{\partial}{\partial t}\mathbf{A}$ we obtain

$$\mathbf{E} = \frac{\partial}{\partial t}(\Lambda \mathbf{J}_S) \tag{2.18}$$

This is the first London equation which describes a perfect conductor since a microscopic local value of an electric field $\mathbf{E}$ leads to a change in time of the current density. There is no dissipation term and therefore no resistivity. Eq. (2.18) additionally shows that the above defined Λ is the proportionality constant in this relation of perfect conductivity. Now taking the curl of both sides of Eq. (2.17) and using $\mathbf{h} = curl\,(\mathbf{A})$ leads to

$$\mathbf{h} = -c\ curl\,(\Lambda \mathbf{J}_S) \tag{2.19}$$

This is the second London equation that, combined with the Maxwell equation $curl\,(\mathbf{h}) = \frac{4\pi}{c}\mathbf{J}$, results in

$$\nabla^2 \mathbf{h} = \frac{1}{\lambda^2}\mathbf{h} \tag{2.20}$$

with the definition of $\lambda = \sqrt{\frac{c^2\Lambda}{4\pi}} = \sqrt{\frac{mc^2}{4\pi n_S e^2}}$. The solution of this differential equation is an exponentially decreasing local magnetic flux density $\mathbf{h}$ with a penetration depth λ after which the field reached $\frac{1}{e}$-th of its value. So Eq. (2.19) describes, together with the mentioned Maxwell equation, the perfect diamagnetism inside the bulk beneath a material dependent length scale λ. The value of n_S remains unspecified but has an upper limit with the total electron density n. Another problem of the London-Theory is that even if the experimental results of the penetration depth are extrapolated to $T = 0$, where $n_S = n$ is assumed, they are still too large compared to the theoretical ones. A quantitative explanation of this is possible with the concept of nonlocality and the introduction of a coherence length ξ_0.

The principle of nonlocality was already introduced by Chambers to generalize Ohm's law $\mathbf{J}(\mathbf{r}) = \sigma \mathbf{E}(\mathbf{r})$ in a way that a current at a point $\mathbf{r}$ depends on an electric field $\mathbf{E}(\mathbf{r}')$ throughout a volume around $\mathbf{r}$ [30]. The radius of this volume is given by the mean free path l in the material. This means that the local field dependence, in other words the relation of the current and the field at the same point, is replaced by a space average field dependence. Pippard applied that concept on Eq. (2.17) with the coherence length ξ replacing l [12]. In the case that l is smaller than ξ_0 the actual coherence length ξ should be further reduced. Thinking about ξ_0 as a minimum size for a wave packet formed by superconducting electrons, the super-current response to a vector potential $\mathbf{A}(\mathbf{r})$ would be reduced if $\mathbf{A}(\mathbf{r})$ decreases within a volume of radius ξ_0 around $\mathbf{r}$. Since the penetration

depth $\lambda \gg \xi_0$ in a type I superconductor there actually is such a decrease of $\mathbf{A(r)}$ and therefore a weakened super-current shielding of an external field. Hence this explains the larger value of the observed penetration depths. The generalization of Eq. (2.17) with this concept can be written as [30]

$$\mathbf{J}_S(\mathbf{r}) = -\frac{3}{4\pi\xi_0\Lambda c} \int \frac{\mathbf{R}[\mathbf{R} \cdot \mathbf{A(r')}]}{R^4} e^{-\frac{R}{\xi}} d\mathbf{r'} \tag{2.21}$$

with $\mathbf{R} = \mathbf{r} - \mathbf{r'}$. Pippard assumed the actual coherence length to be related to the scattering, determined by l, and the coherence length of the pure metal ξ_0 in the following way

$$\frac{1}{\xi} = \frac{1}{\xi_0} + \frac{1}{l} \tag{2.22}$$

Now one needs a good estimate for the value of ξ_0 which can be given by a uncertainty-principle argument. Since only electrons within $\sim k_B T_c$ of the Fermi energy can be responsible for a phenomenon that occurs below T_c, the superconducting electrons should have a momentum range of

$$\Delta p \approx \frac{k_B T_c}{v_F} \tag{2.23}$$

with v_F representing the Fermi velocity. The combination of Eq. (2.23) with the Heisenberg uncertainty-principle leads to

$$\Delta x \gtrsim \frac{\hbar}{\Delta p} \approx \frac{\hbar v_F}{k_B T_c} \tag{2.24}$$

which can be used to define the value of the pure metal's coherence length

$$\xi_0 = a \frac{\hbar v_F}{k_B T_c} \tag{2.25}$$

The parameter a is supposed to be at the order of unity and fits to experimental data gave a value of $a = 0.15$ in tin and aluminum [42]. With type II superconductors often being alloys with small mean free paths Eq. (2.22) explains why they have small coherence lengths leading to the behavior shown in Fig. 2.3 in the previous section.

The most advanced phenomenological treatment of superconductivity was given by Ginsburg and Landau [8]. In the Ginsburg-Landau theory (GL-theory) the focus lies on the superconducting electrons rather than on excitations from the superconducting ground state. A pseudo wave function ψ with a spacial dependence is introduced as an order parameter in Landau's general theory of second order phase transitions. This ψ can be interpreted in a

physical way, being the wave function of the center of mass motion of the superconducting electron pairs. It is related to the density of the superconducting electrons in the following way [30]:

$$n_S = |\psi(\mathbf{r})|^2 \tag{2.26}$$

Therefore n_S is allowed to vary in space and react on perturbations for example by an external field. Hence a theoretical description of superconductivity in fields, strong enough to influence n_S, is possible for example the intermediate state in type I superconductors near $H = H_c$. The GL-theory uses an expansion of the total free energy density in orders of $|\psi|^2$ and $|\nabla\psi|^2$ [30]

$$f = f_{n0} + \alpha|\psi|^2 + \frac{\beta}{2}|\psi|^4 + \frac{1}{m^*}\left|\left(\frac{\hbar}{i}\nabla - \frac{e^*}{c}\mathbf{A}\right)\psi\right|^2 + \frac{h^2}{8\pi} \tag{2.27}$$

with α and β being temperature dependent expansion coefficients. To make this a good approximation $|\psi|$ must be small and should not vary extremely in space to keep $|\nabla\psi|$ small as well. The former is satisfied if T is near T_c but of course still smaller. Now a variational approach is done minimizing f in Eq. (2.27) with respect to the order parameter leading to a differential equation [30]

$$\frac{1}{m^*}\left(\frac{\hbar}{i}\nabla - \frac{e^*}{c}\mathbf{A}\right)\psi + \beta|\psi|^2\psi = -\alpha(T)\psi \tag{2.28}$$

Here only the leading temperature dependence, the one in α, is kept making β approximately temperature independent. Eq. (2.28) looks exactly like the Schrödinger equation for a free particle including a magnetic field coupling except for the nonlinear term in ψ. It thus leads to a form of the super-current that is also equivalent to the quantum mechanical one [30].

$$\mathbf{J}_S = \frac{e^*\hbar}{i2m^*}\left(\psi^*\nabla\psi - \psi\nabla\psi^*\right) - \frac{e^*}{m^*c}|\psi|^2\mathbf{A} \tag{2.29}$$

The best agreement with experimental data is obtained when the values of the effective charge e^* and the effective mass m^*, used in Eq. (2.28) and Eq. (2.29), are taken to be $m^* = 2m$ and $e^* = 2e$. This points towards pairs of electrons being responsible for superconducting behavior. Furthermore a temperature dependent characteristic length scale $\xi(T)$, called the GL coherence length, has to be introduced. It describes the distance over which the pseudo wave function can vary without undue energy increase. Despite the usage

of the same symbol as the Pippard coherence length, $\xi(T)$ has a diffenrent origin and is in general a different quantity. Only in pure superconductors far below T_c it is possible to say that $\xi_0 \approx \xi(T)$. The GL coherence length can be written as [30]

$$\xi(T) = \frac{\hbar}{|2m^*\alpha(T)|^{\frac{1}{2}}} \tag{2.30}$$

Also introduced within the GL theory is the GL parameter [30]

$$\kappa = \frac{\lambda}{\xi} \tag{2.31}$$

which is, due to the same temperature dependences of λ and ξ near T_c, approximately temperature independent. As seen in the discussion of the magnetic properties of supercon- ductors, the value of this parameter distinguishes between type I and type II. In Fig. 2.7 the behavior of the magnetic field and the value of the pseudo wave function are shown as they determine the two just mentioned length scales λ and ξ. Using a variational method
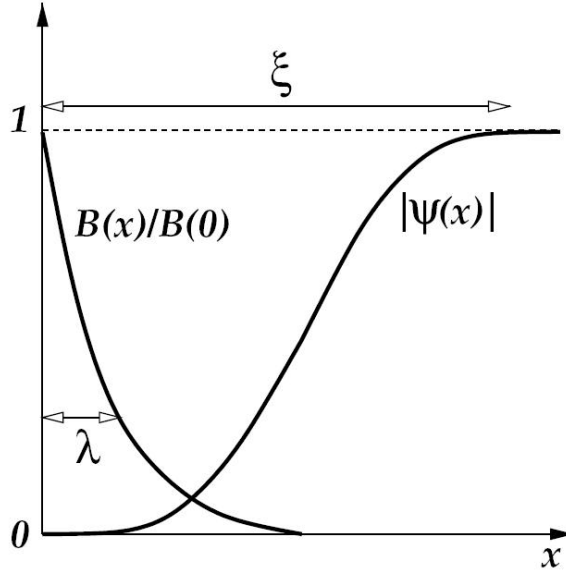
Figure 2.7: Spatial variation of the magnetic field $B(x)$ and the order parameter $|\psi(x)|$ of the Ginzburg-Landau Theory inside a type I superconductor. Both quantities are normalized to unity. The superconducting region begins at $x = 0$ and continues up to larger x-values. The decay of $B(x)$ and the growth of $|\psi(x)|$ determine the value of the penetration length λ and the coherence length ξ respectively. Taken from [31].

on a thermodynamical quantity certainly makes the GL-theory a rather macroscopic one but surprisingly it is closely tied to the microscopic BCS-theory. As shown by Gor'kov

[19] it can be derived directly from the BCS-theory if it is suitably reformulated in terms of Greens functions. The GL theory turns out to be an expansion of BCS for fields that are too large to be treated perturbatively but is limited to temperatures near below T_c. (Under suitable conditions it was extended to all temperatures by Werthamer [20] and by Tewordt [21].) In this case $\psi(\mathbf{r})$ is proportional to the BCS gap parameter $\Delta(\mathbf{r})$ which will be discussed in detail in the following part.

2.2.3 BCS-Theory

As pointed out before there was much evidence that pairs of electrons were responsible for superconductivity but an exact mechanism of how this pairing occurs and why it is energetically favorable was unknown. A first step towards the correct solution, given in the BCS-Theory, was a simplified model by Cooper [15] with one pair of electrons above the fully occupied Fermi sea. The two electrons interact with each other but the noninteracting Fermi sea only acts as a background, blocking the states below the Fermi energy through the Pauli exclusion principle. Additionally the ground state of the electron pair is assumed to have zero momentum which means that the two electrons have momentum $\mathbf{k}$ and $-\mathbf{k}$. This leads to an expansion into plane waves which depends on $\mathbf{k}$ as well as on the difference of the two electrons positions $\mathbf{r}_1 - \mathbf{r}_2$. Since the interaction potential is taken to be attractive, the cosinusodial and therefore symmetric part of the wave function is a better choice because it gives a larger probability amplitude when the electrons are close to each other. This forces an antisymmetric spin singlet function, with the spins pointing in opposite directions, giving the total wave function the necessary antisymmetry. Hence the wave function has the form [30]

$$\psi_0(\mathbf{r}_1 - \mathbf{r}_2) = \left[\sum_{k > k_F} g_{\mathbf{k}} \cos \mathbf{k}(\mathbf{r}_1 - \mathbf{r}_2) \right] (\alpha_1 \beta_2 - \beta_1 \alpha_2) \tag{2.32}$$

with α_1 denoting particle 1 being in spin up state and β_1 meaning particle 1 being in spin down state. The sum runs over all k above the Fermi surface since the states below are occupied and are thus blocked for the pair electrons. Inserting Eq. (2.32) into the Schrödinger equation with an interaction potential $V(\mathbf{r}_1 - \mathbf{r}_2)$ results in [30]

$$(E - 2\epsilon_{\mathbf{k}}) g_{\mathbf{k}} = \sum_{k' > k_F} V_{\mathbf{k}\mathbf{k}'} g_{\mathbf{k}'} \tag{2.33}$$

Here $\epsilon_\mathbf{k}$ stands for the unperturbed plane-wave energy and $V_{\mathbf{kk}'}$ represents the regular Fourier transform of the interaction potential which describes the strength of electron pair scattering. A solution of Eq. (2.33) with a set of $g_\mathbf{k}$ having energies $E < 2E_F$ would symbolize a bound state for electron pairs within the system. To find such a solution with a general $V_{\mathbf{kk}'}$ is quite difficult so an approximation is made which seems to be very crude at the moment. $V_{\mathbf{kk}'}$ is taken to be constant and negative within an energy interval $\hbar\omega_c$ and zero outside, with ω_c denoting the corresponding cutoff frequency. This will actually turn out to be a good approximation since the physically important changes will take place in the very vicinity of the Fermi energy. This then allows to cancel out the weighting coefficients in Eq. (2.33) and after a transformation of the sum into an integral and the assumption of a constant density of states $N(0)$ at the Fermi level we arrive at [30]

$$\frac{1}{V} = N(0) \int_{E_F}^{E_F + \hbar\omega_c} \frac{d\epsilon}{2\epsilon - E} = \frac{1}{2} N(0) \ln \frac{2E_F - E + 2\hbar\omega_c}{2E_F - E} \tag{2.34}$$

In the weak coupling limit, meaning $N(0)V \ll 1$, one can write this as [30]

$$E \approx 2E_F - 2\hbar\omega_c e^{-\frac{2}{N(0)V}} \tag{2.35}$$

This result shows that there is negative binding energy, no matter how small the interaction between the electrons is, and therefore a bound state for a pair exists. This is a remarkable result since these electrons have larger kinetic energies than those in the Fermi sea but occupy an energetically lower and thus favorable state. It is important to note that the binding energy term in Eq. (2.35) is nonanalytic at $V = 0$ which makes a perturbational treatment impossible and explains the mathematical difficulties earlier approaches faced. Although this model obtains a bound pair state it still leaves some questions open. Yet there is no energy gap in the model, which is observed in experiments, and the the treatment of isolated pairs is questionable. Taking the estimate for ξ_0 of Eq. (2.25) as the size of the pair, which is at the order of $\sim 10^4$ Å, the necessary distance of the pairs to be able to treat them as separated would lead to a density of superconducting pairs that is much too small to fit the experiments [43]. Furthermore there is nothing explaining the origin of the attractive interaction between two negatively charged particles.

A first important fact that helps to solve this problem is that the usually strong and long range Coulomb repulsion is screened inside a solid by the other electrons. This reduces

the repulsion dramatically at distances of the above mentioned intrapair distance ξ_0 and allows a weaker attractive interaction to dominate. Fröhlich suggested that electron-lattice interactions could lead to an effective attractive interaction between two electrons [11] via the mechanism displayed in Fig. 2.8. The idea is that an electron moving through the solid

Figure 2.8: Schematic illustration of phonon mediated attractive effective interaction between two electrons. **Left:** The first electron distorts the lattice creating inhomogeneities in the distribution of the positive charges of the ions. This charge inhomogeneity decays away with the frequency of the excited phonon. **Right:** A second electron with opposite momentum is attracted by the more positively charged space at a later time but before the inhomogeneity had time to decay away. Taken from [31].

polarizes the lattice by attracting the positive ions. In other words the electron excites a phonon since the ions relax back into their equilibrium position in an oscillatory movement. The distortion thus decays away with the frequency of the excited phonon which means that for an other electron reaching this point soon enough the polarization is still present. Hence the second electron is attracted by the first one through a lattice distortion that is a lot less mobile than the electrons themselves. This allows the necessary intrapair distance to be large enough for the screened Coulomb repulsion to be overcome by the phonon mediated attraction. Mathematically this can be shown by using a phonon Hamiltonian of the form [44]

$$\hat{H}_{ph} = \sum_{\mathbf{q},j} \omega_q a^\dagger_{\mathbf{q},j} a_{\mathbf{q},j} + const. \tag{2.36}$$

together with an electron-phonon Hamiltonian that is written as [44]

$$\hat{H}_{el-ph} = \gamma \sum_{\mathbf{k},\mathbf{q},j} \frac{iq_j}{(2m\omega_q)^{1/2}} \hat{n}_{\mathbf{q}} (a_{\mathbf{q},j} + a^\dagger_{-\mathbf{q},j}) \tag{2.37}$$

with ω_q being the phonon dispersion and the index $j = 1, 2, 3$ denoting the three spacial dimensions. $a_{\mathbf{q},j}$ and $a^\dagger_{\mathbf{q},j}$ are the bosonic annihilation and creation operators of the second quantization formalism respectively. $\hat{n}_{\mathbf{q}} \equiv \sum_{\mathbf{k}} c^\dagger_{\mathbf{k}+\mathbf{q}} c_{\mathbf{k}}$ represents the electronic density expressed in terms of fermionic creation and annihilation operators and γ is a coupling

constant. With the introduction of Grassmann fields ψ ($\tilde{\psi}$) and complex fields ϕ ($\tilde{\phi}$) as a representation of the fermionic and bosonic operators respectively the Hamiltonians in Eq. (2.36) and Eq. (2.37) can be used to formulate the coherent state actions S in the coherent state field integral.

$$
\begin{aligned}
\mathscr{Z} &= \int \mathscr{D}[\tilde{\psi}, \psi] \int \mathscr{D}[\tilde{\phi}, \phi] e^{-S_{el}[\tilde{\psi},\psi]-S_{ph}[\tilde{\phi},\phi]-S_{el-ph}[\tilde{\psi},\psi,\tilde{\phi},\phi]} \\
&= \int \mathscr{D}[\tilde{\psi}, \psi] e^{-S_{el}[\tilde{\psi},\psi]+\ln(\int \mathscr{D}[\tilde{\phi},\phi] \exp(-S_{ph}[\tilde{\phi},\phi]-S_{el-ph}[\tilde{\psi},\psi,\tilde{\phi},\phi]))} \\
&\equiv \int \mathscr{D}[\tilde{\psi}, \psi] e^{-S_{eff}[\tilde{\psi},\psi]}
\end{aligned}
\tag{2.38}
$$

The effective action S_{eff} defined in Eq. (2.38) can then be calculated by integrating out the bosonic fields which results in

$$
S_{eff}[\tilde{\psi}, \psi] = S_{el}[\tilde{\psi}, \psi] - \frac{\Gamma}{2m} \sum_q \frac{q^2}{\omega_q^2 - \omega^2} \rho_q \rho_{-q}
\tag{2.39}
$$

with $\rho_q = \sum_k \tilde{\psi}_{k+q} \psi_k$ describing the electron density written in terms of Grassmann fields. The electron action S_{el}, not written out explicitly, is reduced by the second term on the right hand side as soon as $\omega < \omega_q$ for every q. So this result shows that the Coulomb repulsion can indeed be weakened and with a large enough electron phonon coupling γ (Γ is a function of γ) even overcome, resulting in a negative effective action and therefore an attractive interaction. Short after the proposal of such a phonon mediated mechanism the isotope effect was discovered [9, 10] showing a dependence of the critical temperature on the mass of different isotopes of the same element in the form

$$
T_c \sim M^\alpha
\tag{2.40}
$$

For most regular superconductors $\alpha \approx -\frac{1}{2}$. This is a clear evidence for phonons being involved in the microscopic mechanism of superconductivity because of the same inverse square root dependence of the phonon frequency on the ions mass. This leads to the identification of the previously mentioned cutoff frequency ω_c with the Debye frequency ω_D which characterizes the cutoff in the phonon spectrum. Hence the binding energy in Eq. (2.35) can be rewritten and we obtain for the energy of paired electrons in Coopers simplified model

$$
E \approx 2E_F - 2\hbar\omega_D e^{-\frac{2}{N(0)V}}
\tag{2.41}
$$

with now $\hbar\omega_D$ being the important energy scale.

After having realized that the usual ground state, with all states being occupied to the Fermi energy and all states being unoccupied above, is unstable towards the formation of pairs as soon as there is an attractive interaction and having found an explanation for that interaction it is now the task to find an expression for that new ground state. Such an expression was formulated in the original BCS-theory [16, 17] with a mean-field approach justified by the large number of involved particles. Here the approximation is made that the occupancy of a state with wave vector $\mathbf{k}$ only depends on the average occupancies of the other states which leads to the average of the particle number $\bar{N}$ being fixed instead of N itself. This statistical treatment of occupancies certainly needs to be done in the grand canonical ensemble. Furthermore the following treatment is restricted to $T = 0$ so that there are no thermal excitations present. The BCS ground state wave function [30]

$$|\psi_G\rangle = \prod_{\mathbf{k}=\mathbf{k}_1,...,\mathbf{k}_M} \left(u_{\mathbf{k}} + v_{\mathbf{k}} c^{\dagger}_{\mathbf{k}\uparrow} c^{\dagger}_{-\mathbf{k}\downarrow} \right) |\phi_0\rangle \tag{2.42}$$

consists of the vacuum state $|\phi_0\rangle$ out of which the fermionic creation operators $c^{\dagger}_{\mathbf{k}\uparrow} c^{\dagger}_{-\mathbf{k}\downarrow}$ create cooper pairs with opposite momentum and spin. $|v_{\mathbf{k}}|^2$ represents the probability that a pair $(\mathbf{k}\uparrow, -\mathbf{k}\downarrow)$ is occupied and $|u_{\mathbf{k}}|^2$ denotes the probability that this pair is unoccupied. This implies the proper normalization condition $|v_{\mathbf{k}}|^2 + |u_{\mathbf{k}}|^2 = 1$. To extract physical information out of the ground state in Eq. (2.42) the two parameters $v_{\mathbf{k}}$ and $u_{\mathbf{k}}$ have to be calculated. This is done by a variational approach with the so called pairing Hamiltonian [30]

$$\hat{H} = \sum_{\mathbf{k}\sigma} \epsilon_{\mathbf{k}} n_{\mathbf{k}\sigma} + \sum_{\mathbf{kl}} V_{\mathbf{kl}} c^{\dagger}_{\mathbf{k}\uparrow} c^{\dagger}_{-\mathbf{k}\downarrow} c_{-\mathbf{l}\downarrow} c_{\mathbf{l}\uparrow} \tag{2.43}$$

with σ being the spin of the particle. The first term, containing the particle number operator $n_{\mathbf{k}\sigma} = c^{\dagger}_{\mathbf{k}\sigma} c_{\mathbf{k}\sigma}$, describes the kinetic energy and the second term stands for pair scattering with the scattering potential $V_{\mathbf{kl}}$. In order to regulate the mean number of particles $\bar{N}$ the term $-\mu N_{OP}$ has to be added to the Hamiltonian, as usual in the grand canonical ensemble, with $N_{OP} = \sum_{\mathbf{k}\sigma} n_{\mathbf{k}\sigma}$. This is equivalent to a shift in energy with the chemical potential μ. Thus with the definition of $\xi_{\mathbf{k}} = \epsilon_{\mathbf{k}} - \mu$ as the single particle energy relative to the

Fermi energy only $\epsilon_{\mathbf{k}}$ has to be substituted with $\xi_{\mathbf{k}}$ in Eq. (2.43) to obtain $\hat{H} - \mu N_{OP}$. The expectation value of this operator in the BCS ground state turns out to be [30]

$$\langle \psi_G | \hat{H} - \mu N_{OP} | \psi_G \rangle = 2 \sum_{\mathbf{k}} \xi_{\mathbf{k}} v_{\mathbf{k}}^2 + \sum_{\mathbf{kl}} V_{\mathbf{kl}} u_{\mathbf{k}} v_{\mathbf{k}} u_{\mathbf{l}} v_{\mathbf{l}} \tag{2.44}$$

where $u_{\mathbf{k}}$ and $v_{\mathbf{k}}$ are taken to be real for simplicity. The variation is done by applying the derivative with respect to one of the parameters to the right hand side of Eq. (2.44) while keeping the others fixed and setting the result equal to zero. Carrying out the further calculation the definitions $\Delta_{\mathbf{k}} = -\sum_{\mathbf{l}} V_{\mathbf{kl}} u_{\mathbf{l}} v_{\mathbf{l}}$ and $E_{\mathbf{k}} = \left(\xi_{\mathbf{k}}^2 + \Delta_{\mathbf{k}}^2 \right)^{1/2}$ are made because those quantities turn to be of certain interest later on. After that the same approximation as in Coopers one pair model is made meaning in this case [30]

$$V_{\mathbf{kl}} = \begin{cases} \Delta & \text{if } |\xi_{\mathbf{k}}| \text{ and } |\xi_{\mathbf{l}}| \leq \hbar \omega_c \\ 0 & \text{otherwise} \end{cases} \tag{2.45}$$

This leads to a big simplification of the above defined $\Delta_{\mathbf{k}}$

$$\Delta_{\mathbf{k}} = \begin{cases} \Delta & \text{for } |\xi_{\mathbf{k}}| < \hbar \omega_c \\ 0 & \text{for } |\xi_{\mathbf{k}}| > \hbar \omega_c \end{cases} \tag{2.46}$$

which is now independent of $\mathbf{k}$. After some mathematical manipulations that are not of great physical interest one gets for Δ [30, 31]

$$\Delta = \frac{\hbar \omega_c}{\sinh \left[N(0) V \right]} \approx 2 \hbar \omega_D e^{-\frac{1}{N(0) V}} \tag{2.47}$$

In the last step the weak coupling limit is assumed with $N(0)V \ll 1$ and the cutoff frequency is again taken to be the Debye frequency. For the parameters $v_{\mathbf{k}}$ and $u_{\mathbf{k}}$ the following result is obtained [30]

$$\begin{aligned} v_{\mathbf{k}}^2 &= \frac{1}{2} \left(1 - \frac{\xi_{\mathbf{k}}}{E_{\mathbf{k}}} \right) = \frac{1}{2} \left[1 - \frac{\xi_{\mathbf{k}}}{\left(\xi_{\mathbf{k}}^2 + \Delta_{\mathbf{k}}^2 \right)^{1/2}} \right] \\ u_{\mathbf{k}}^2 &= \frac{1}{2} \left(1 + \frac{\xi_{\mathbf{k}}}{E_{\mathbf{k}}} \right) = 1 - v_{\mathbf{k}}^2 \end{aligned} \tag{2.48}$$

This result is plotted in Fig. 2.9 neglecting the $\mathbf{k}$-dependence of all quantities. The occupation fraction of Cooper pairs $|v|^2$ is 1 far below and 0 far above the Fermi level and 0.5 at the Fermi energy. These features are the same as for the Fermi occupation at zero temperatures but in contrast to this $|v|^2$ shows an asymptotical behavior towards those values instead of

a sudden jump. Thus there is a change in occupation from the normal to the supercon-
ducting phase but this only effects an energy range of about Δ around the Fermi energy.
So only a tiny fraction of the electrons is energetically shifted to lager kinetic energies and
the majority remains unchanged in this picture. The dramatic change takes place in the
probability of k-space occupation since there is a much larger chance of **k** being occupied
if -**k** is occupied. This direct correspondence of the paired electrons together with the fact
that all pairs are described by one wave function, shown in Eq. (2.42) is the essence of
superconductivity. Under the assumption that the number of electronic states is conserved
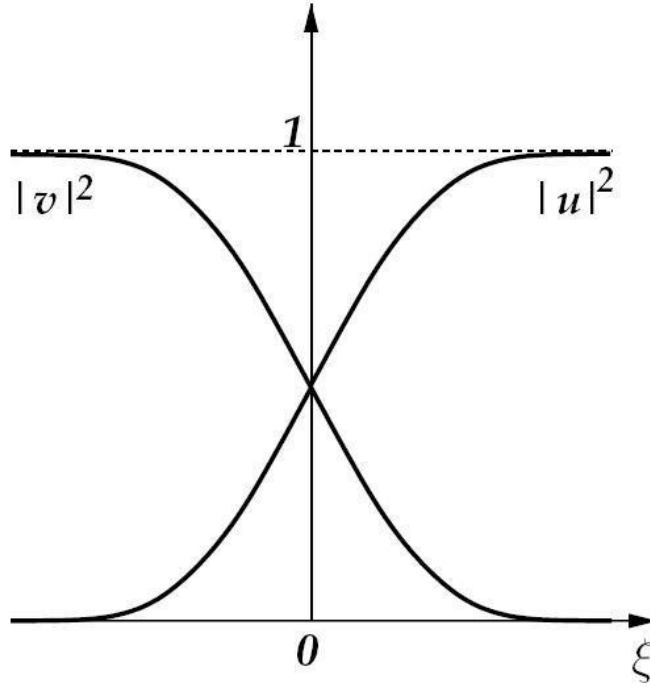
Figure 2.9: Cooper pair occupation parameters $|v|^2$ and $|u|^2$ as a function of ξ. **k**-
dependencies are neglected. The Cooper pair occupation fraction $|v|^2$ approaches 1 asymp-
totically for negative ξ and 0 for positive ξ. $|u|^2$ shows exactly inverse behavior. There
is a startling resemblance between $|v|^2$ and the Fermi distribution for finite temperatures.
Taken from [31].

during the superconducting phase transition it is possible to compute the superconducting
density of states $N_s(E)$ [30].

$$N_s(E)dE = N_n(\xi)d\xi \Rightarrow N_s(E) = N_n(\xi)\frac{d\xi}{dE} \qquad (2.49)$$

Using the definition of $E = \left(\xi^2 + \Delta^2\right)^{1/2}$ given above, without the **k**-dependencies, and the simplification of Δ given in Eq.(2.46) this results in

$$N_s(E) = \begin{cases} N(0)\frac{E}{(E^2-\Delta^2)^{1/2}} & \text{for} |E| > |\Delta| \\ 0 & \text{for} |E| < |\Delta| \end{cases} \tag{2.50}$$

Here the normal state density of states $N_n(\xi)$ was taken to be a constant $N(0)$ since it is in a very close range to the Fermi energy. The plot of Eq. (2.50) is displayed in Fig. 2.10. $N_s(E)$ shows a gap in an energy range of Δ above the Fermi energy and diverges in the
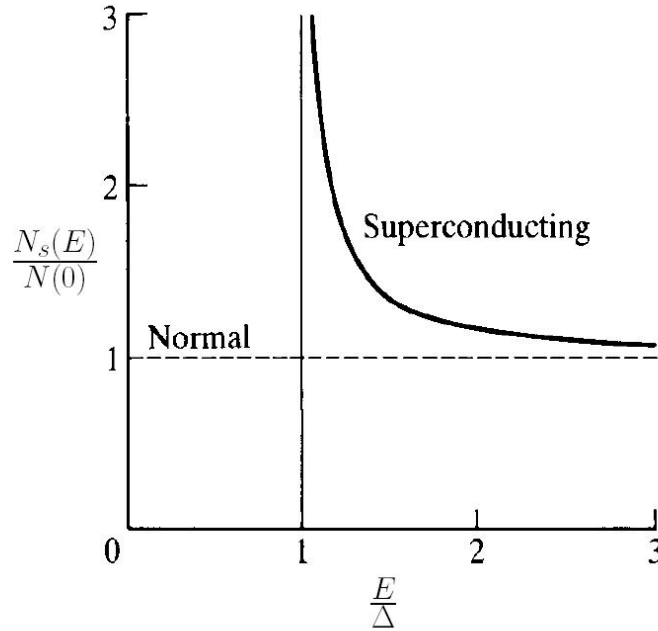
Figure 2.10: Density of states as a function of E. $N_s(E)$ shows a huge deviation from the normal state density at the Fermi level $N(0)$. There is a gap with no allowed states beginning at Δ above the Fermi level and $N_s(E)$ diverges when it approaches this gap. Taken from [30].

vicinity of the gap. This leads to a heavily increased density of states right above the gap. Since Δ is related to the pair scattering potential this effect is a direct consequence of the Cooper pairing. As a result of this gap in $N_s(E)$ there are no possible excitations of energies smaller than 2Δ since the cooper pairs have to be broken first. This means that it is not possible to drive the superconducting condensate out of its ground state unless this energy is applied which explains the previously mentioned rigidity and leads to the remarkable

effects discussed in the first part of this chapter. At this point it is easily understood why the definition of the quantities $\Delta_{\mathbf{k}}$ and $E_{\mathbf{k}}$ were made. Δ denotes the size of the energy gap in $N_s(E)$ and E has the meaning of a quasi particle energy of excited quasi particles out of the superconducting ground state. So both are important in describing superconducting properties and thus of physical interest. Another important quantity that can be computed, with the parameters u and v being determined and therefore also the ground state wave function $|\psi_G\rangle$ entirely known, is the ground state energy. The combination of Eq. (2.44), the definition of $\Delta_{\mathbf{k}}$ and Eq. (2.48) leads to the expectation value [30]

$$\langle\psi_G|\,\hat{H} - \mu N_{OP}\,|\psi_G\rangle = \sum_{\mathbf{k}}\left(\xi_{\mathbf{k}} - \frac{\xi_{\mathbf{k}}^2}{E_{\mathbf{k}}}\right) - \frac{\Delta^2}{V} \tag{2.51}$$

In order to compare this result to the normal state and find an expression for the condensation energy we need to set the energy gap in Eq. (2.51) equal to zero since that refers to the normal state at $T = 0$. This leads to

$$\langle\psi_N|\,\hat{H} - \mu N_{OP}\,|\psi_N\rangle = \sum_{|\mathbf{k}|<k_F} 2\xi_{\mathbf{k}} \tag{2.52}$$

with the summation only going to k_F since all states above are empty at $T = 0$. Subtracting Eq. (2.51) from Eq. (2.52) gives the condensation energy [30]

$$\begin{aligned}
\langle E\rangle_s - \langle E\rangle_n &= \sum_{|\mathbf{k}|>k_F}\left(\xi_{\mathbf{k}} - \frac{\xi_{\mathbf{k}}^2}{E_{\mathbf{k}}}\right) - \sum_{|\mathbf{k}|<k_F}\left(-\xi_{\mathbf{k}} - \frac{\xi_{\mathbf{k}}^2}{E_{\mathbf{k}}}\right) - \frac{\Delta^2}{V}\\
&= 2\sum_{|\mathbf{k}|>k_F}\left(\xi_{\mathbf{k}} - \frac{\xi_{\mathbf{k}}^2}{E_{\mathbf{k}}}\right) - \frac{\Delta^2}{V}
\end{aligned} \tag{2.53}$$

Here the symmetry of all quantities about the Fermi energy was used in the second equality. The first term of Eq. (2.53) describes the excess energy of the above mentioned kinetic energy shift and the second term reflects the change in potential energy due to pairing. By replacing the sum with an integral over ξ from 0 to $\hbar\omega_c$, justified by the huge particle number, and again using the weak coupling limit $N(0)V \ll 1$ Eq. (2.53) results in [30]

$$\langle E\rangle_s - \langle E\rangle_n = \left[\frac{\Delta^2}{V} - \frac{1}{2}N(0)\Delta^2\right] - \frac{\Delta^2}{V} = -\frac{1}{2}N(0)\Delta^2 \tag{2.54}$$

So the condensation energy at $T = 0$ is negative showing again that the superconducting state is energetically favorable over the normal state and thus realized. The energy in Eq. (2.54) has to be the same as in Eq. (2.6) obtained earlier.

The just used variational approach leads to the right results but as soon as finite temperatures are included it is simpler to use another treatment. With the introduction of quasi particle operators that represent excitations which have $E_{\mathbf{k}}$ as their energies the probability that a quasi particle is excited in thermal equilibrium is just [30]

$$f(E_{\mathbf{k}}) = \frac{1}{e^{\beta E_{\mathbf{k}}} + 1} \tag{2.55}$$

This is simply the Fermi function with the usual definition of $\beta = \frac{1}{k_B T}$. Noting that $E_{\mathbf{k}} \geq \Delta$ and therefore finite for a nonvanishing energy gap it is obvious that $f(E_{\mathbf{k}})$ goes to zero at $T = 0$ for all $\mathbf{k}$, including those with $|\mathbf{k}| < k_F$. So there are no quasi particles at absolute zero temperature. The average value of the usual particle occupation operator, formed by the quasi particle operators, can be substituted by $f(E_{\mathbf{k}})$ of Eq. (2.55) and so the temperature dependence of the superconducting energy gap can be computed. First of all one obtains [30]

$$\frac{\Delta(0)}{k_B T_c} = 1.764 \tag{2.56}$$

which shows that the energy gap at zero temperature is about the same value as $k_B T_c$. Furthermore the temperature dependence of the energy gap $\Delta(T)$ itself can be evaluated numerically in the weak coupling limit and the result is shown in Fig. 2.11. The energy gap
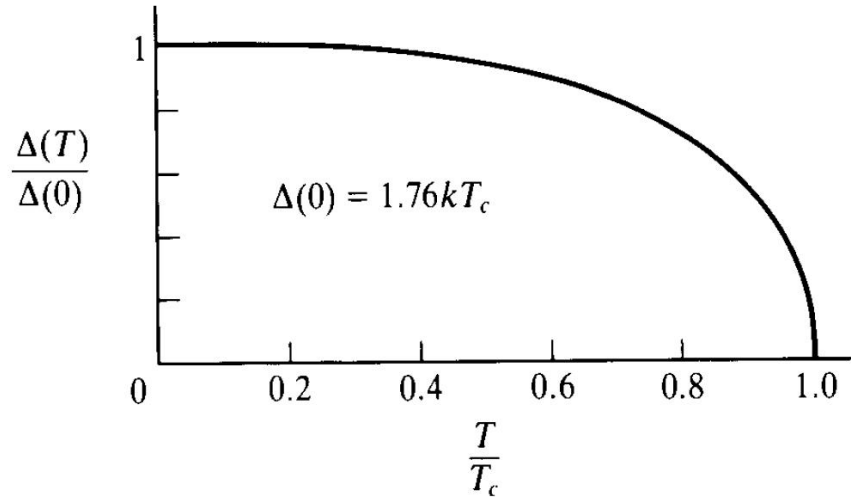
Figure 2.11: Superconducting energy gap as a function of temperature. At low temperatures Δ shows an almost constant value and near T_c a square root temperature dependence is observed. Taken from [30].

decreases monotonically from its zero temperature value to zero at T_c where the temperature dependence can be approximated by [30]

$$\frac{\Delta(T)}{\Delta(0)} \approx 1.74 \left(1 - \frac{T}{T_c}\right)^{\frac{1}{2}} \tag{2.57}$$

At very low temperatures Δ is nearly constant which can be physically interpreted as the fact that a significant number of quasi particles have to be excited before the energy gap value is effected by temperature variations.

Having talked about excitations from the BCS ground state in Eq. (2.42) it will now be discussed how those excitations actually take place within the superconducting condensate. Here another characteristic feature of superconductivity comes into play with the ground state not only being macroscopic but phase coherent. This has huge effects on the interaction Hamiltonian [30]

$$\hat{H}_I = \sum_{\mathbf{k}\sigma, \mathbf{k}'\sigma'} B_{\mathbf{k}'\sigma', \mathbf{k}\sigma} c_{\mathbf{k}'\sigma'}^{\dagger} c_{\mathbf{k}\sigma} \tag{2.58}$$

with $B_{\mathbf{k}'\sigma', \mathbf{k}\sigma}$ standing for the matrix elements of the perturbating operator between regular one-electron states. In the normal state the transition probability is simply proportional to the square of the particular $B_{\mathbf{k}'\sigma', \mathbf{k}\sigma}$ since all terms in the sum of Eq. (2.58) are independent in this case. In the superconducting state this changes dramatically because the phase coherence produces interference terms that lead to coherence factors which have to be multiplied to $\left|B_{\mathbf{k}'\sigma', \mathbf{k}\sigma}\right|^2$. For the scattering of quasi particles the proper coherence factor is $(u_{\mathbf{k}} u_{\mathbf{k}'} \mp v_{\mathbf{k}} v_{\mathbf{k}'})^2$ and for the creation or annihilation of two quasi particles the coherence factor turns out to be $(v_{\mathbf{k}} u_{\mathbf{k}'} \pm u_{\mathbf{k}} v_{\mathbf{k}'})^2$. In both expressions the upper sign corresponds to case I which is even under time reversal of the electronic states. The lower sign corresponds to case II with odd symmetry under this transformation that interchanges the partners in the Cooper-pairing scheme. An example for case I is ultrasonic attenuation and for case II it is spin relaxation. With the result obtained in Eq. (2.48) these coherence factors can be evaluated as functions of the involved energies [30].

$$(u_{\mathbf{k}} u_{\mathbf{k}'} \mp v_{\mathbf{k}} v_{\mathbf{k}'})^2 = \frac{1}{2}\left(1 \mp \frac{\Delta^2}{E_{\mathbf{k}} E_{\mathbf{k}'}}\right) \tag{2.59}$$

for the scattering of quasi particles and

$$(v_{\mathbf{k}} u_{\mathbf{k}'} \pm u_{\mathbf{k}} v_{\mathbf{k}'})^2 = \frac{1}{2}\left(1 \pm \frac{\Delta^2}{E_{\mathbf{k}} E_{\mathbf{k}'}}\right) \tag{2.60}$$
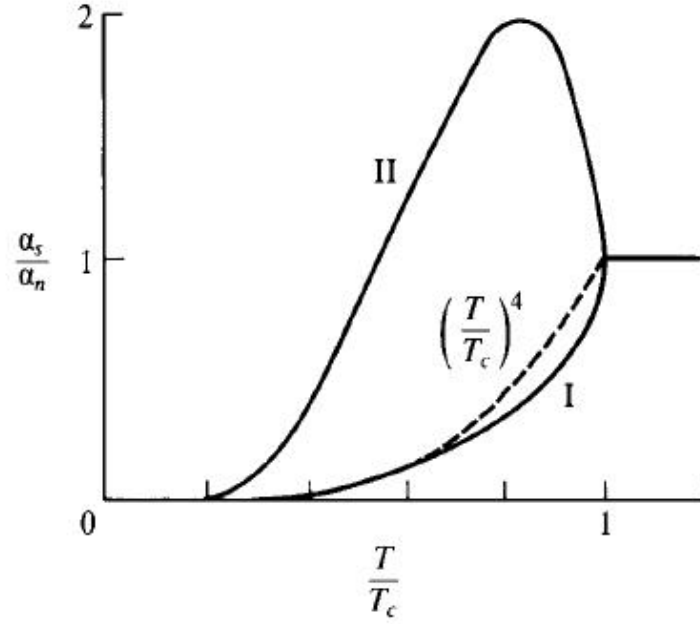
Figure 2.12: Comparison of the temperature dependence of the transition rates α in the superconducting (s) and normal (n) state. Also shown, as the dashed line, is the $(T/T)^4$ dependence predicted by a super fluid model. Case I does not deviate too much from the oversimplified super fluid model but case II shows a significantly different behavior, especially near T_c. Taken from [30].

for quasi particle creation and annihilation. Actual calculations of transition rates for both cases are shown in Fig. 2.12. Case I is not to far away from the super fluid approximation which is plotted as the dashed line and deviates only slightly in the vicinity of T_c. A whole different shape is observed for case II which increases below T_c and has a clear peak. Here the coherence factors produce completely different behavior than predicted by a two fluid model demonstrating its oversimplified character.

2.3 Examples for experimental verification of the BCS-Theory

2.3.1 Superconducting density of states

A convincing way to verify the BCS theory would be a direct measurement of the density of states which shows a large difference between the normal and the superconducting state (see Fig. 2.10). This can be done by tunneling spectroscopy at a normal-insulator-superconductor junction. The charge transfer through such an insulating barrier is nonzero

due to quantum mechanical tunneling and varies exponentially with the width of the insulator. It turns out that the transition probability of the charge carriers is independent of the BCS occupancy factors $u_{\mathbf{k}}$ and $v_{\mathbf{k}}$ and the process can be described by the semiconductor model. Here the density of states of the normal metal is seen to be constant near the chemical potential and the superconductor is taken to be a simple semiconductor with an independent particle density of states that exhibits the form of the the density of states in Fig. 2.10. It is symmetric with respect to the chemical potential and the superconducting character is most dominant directly above and below the gap where the density of states diverges. An applied potential difference eV (electronic charge e, applied voltage V) shifts the chemical potential and wherever there are occupied states at the same energy level on one side of the barrier as there are free states on the other side a horizontal transition is possible. In the semiconductor model the tunneling current between a superconductor and a normal metal can be written as [30]

$$
\begin{aligned}
I_{ns} &= A \left|T\right|^2 N_1(0) \int_{-\infty}^{\infty} N_{2s}(E) \left[f(E) - f(E + eV)\right] dE \\
&= \frac{G_{nn}}{e} \int_{-\infty}^{\infty} \frac{N_{2s}(E)}{N_2(0)} \left[f(E) - f(E + eV)\right] dE
\end{aligned}
\tag{2.61}
$$

with the normal-normal tunneling conductance G_{nn} defined as

$$
G_{nn} \equiv eA \left|T\right|^2 N_1(0) N_2(0)
\tag{2.62}
$$

A is a proportionality constant, T is the constant tunneling-matrix element and $N_1(0)$ and $N_{2s}(E)$ denote the normal density of states of metal 1 and the superconducting density of states of metal 2 respectively. f represents the regular Fermi function. To directly compare the theory to the experiment one has to study the differential conductance $\frac{dI}{dV}$ of the current in Eq. (2.61) as a function of V.

$$
G_{ns} = \frac{dI_{ns}}{dV} = G_{nn} \int_{-\infty}^{\infty} \frac{N_{2s}(E)}{N_2(0)} \left[-\frac{\partial f(E + eV)}{\partial(eV)}\right] dE
\tag{2.63}
$$

The term $\left[-\frac{\partial f(E+eV)}{\partial(eV)}\right]$ is a bell-shaped weighting function with its peak located at $E = -eV$, a width $\sim 4k_B T$ and a unit area under the curve. Thus in the limit of $T \to 0$ Eq. (2.63) becomes

$$
(G_{ns})_{T=0} = G_{nn} \frac{N_{2s}(e|V|)}{N_2(0)}
\tag{2.64}
$$

Here the absolute value of the voltage is taken since both signs are equal because excitations of electrons and holes have equal energies. Eq.(2.64) shows that for very low temperatures the differential conductance is proportional to the superconducting density of states and this quantity can directly be observed. At absolute zero one would indeed measure a vanishing current until $e|V| \gtrsim \Delta$ since the shift in the chemical potential must be large enough to create an excitation in the superconductor. A finite temperature smears out the peak at Δ
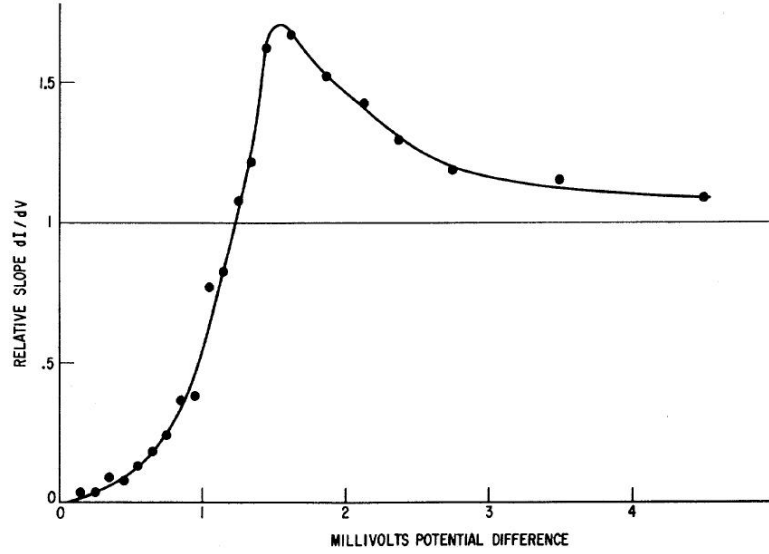
Figure 2.13: Slope $\frac{dI}{dV}$ as a function of applied voltage of a junction of superconducting Pb and normal Al with a Al_2O_3 insulating barrier normalized to the slope of the same junction in the normal state. The measurement was performed by Ivar Giaever at $T = 1.6K$ [45]. This measures directly the superconducting density of states normalized to the nonsuperconducting density of states in Pb.

by $\sim \pm 2k_B T$ and a finite density of states is obtained below the peak since some excitations are already thermally created. In Fig. 2.13 original data from Ivar Giaever [45] obtained in 1960 is presented. He measured the tunnel current as a function of applied voltage on a junction of superconducting Pb and normal Al with a Al_2O_3 insulating barrier. To obtain the curve for the normalization to the nonsuperconducting conductance a magnetic field was applied to drive the Pb layer into the normal state. The slope of the former curve divided through the slope of the latter curve is displayed in the graph. According to Eq. (2.64) this serves as a direct measurement of the superconducting density of states normalized to

the normal density of states. The curve can be seen as a thermally smeared version of Fig. 2.10 with the features discussed above and therefore validates the BCS theory.

2.3.2 Coherence factors

Another unique feature of the superconducting state are the coherence factors appearing in the transition probabilities of quasi particle scattering (Eq. (2.59)) and creation and annihilation of quasi particles (Eq. (2.60)). To experimentally verify the existence of the effects
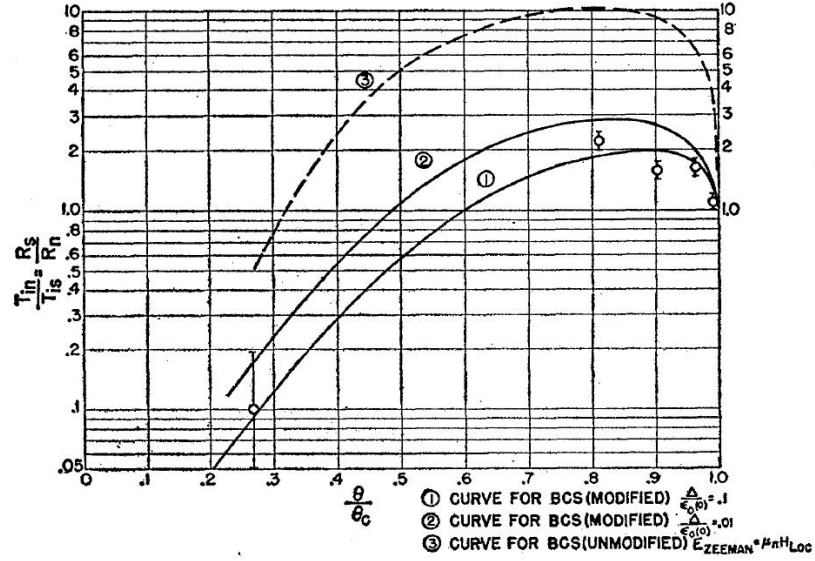
Figure 2.14: Ratio of normal to superconducting relaxation time of nuclear spin relaxation, which is equal to the ratio of the superconducting to the normal transition rate, as a function of temperature normalized to the transition temperature. The increase of the transition rate below the critical temperature is shown together with three theoretical curves calculated on the basis of the BCS theory. Original data from Hebel and Slichter [46] published in 1959.

of these coherence factors would be a direct validation of the BCS theory. Furthermore the fact that there are two different cases for both coherence factors, depending on the symmetry of the involved process under time reversal, gives an excellent opportunity for very convincing verification of the BCS theory by predicting experimental results for the two different cases. Since the scattering of quasi particles is involved in ultrasonic attenuation as well as in spin relaxation both experiments can serve as a proving ground. The former is of case I thus the ratio of the transition rates in the superconducting and the normal state should show the behavior of the lowest curve in Fig. 2.12. However the more interesting

case is certainly case II since here the normalized transition rate $\frac{\alpha_s}{\alpha_n}$ increases directly below T_c before it goes to zero for $T \to 0$, as seen in Fig. 2.12. In 1959 Hebel and Slichter [46] obtained this form in their data of nuclear spin relaxation times. The graph shown in Fig. 2.14 exhibits an increase of the transition rate ratio (here denoted by $\frac{R_s}{R_n}$) below the critical temperature (here denoted by θ_c). The dashed line is a calculation based on the BCS theory and only predicts the qualitative behavior of the data while modified models by Hebel and Slichter are able to reach also quantitative consensus. This measurement of the influence of the coherence factors is an outstanding visualization of the superconducting phase coherence and a historically decisive proof of the BCS theory.

Chapter 3

Iron-based superconductors

In this chapter an overview of the recently discovered new high temperature superconductors based on iron compounds is done. Considering the large number of publications and the fast progress in this field of research this overview is not intended to be complete but only tries to summarize the basic properties by selected examples of materials and measurements. First the lattice structure of the different families is shown and the conditions under which they actually become superconducting are presented. Second a short overlook on calculations and measurements of the electronic structure is given. Also the size and momentum distribution of the superconducting gap parameter is shown followed by a short discussion of its symmetry. In the last section an example of a phase diagram is presented and compared to several others. Furthermore possible candidates for the superconducting pairing mechanism are discussed.

3.1 Lattice structure of different families

The discovery of superconductivity with a transition temperature as high as $T_c = 26K$ in $LaOFeAs$ by Kamihara et al [28] in the beginning of 2008 opened up a hole new field of research. It was quite a surprise that the ferromagnetic atom iron could be used to produce superconducting compounds with such a high T_c that could be even raised to $T_c = 43K$ in this compound by applying pressure [47]. To achieve superconductivity in this material the parent compound had to be doped with fluorine replacing oxygen in the LaO layer adding an extra electron to the $FeAs$ plane (see lower left in Fig. 3.1) similar to the cuprate superconductors. $LaOFeAs$ condenses in the $ZrCuSiAs$ type structure (space group $P4/nmm$) and by substituting La by different rare earth metals a lot of other materials
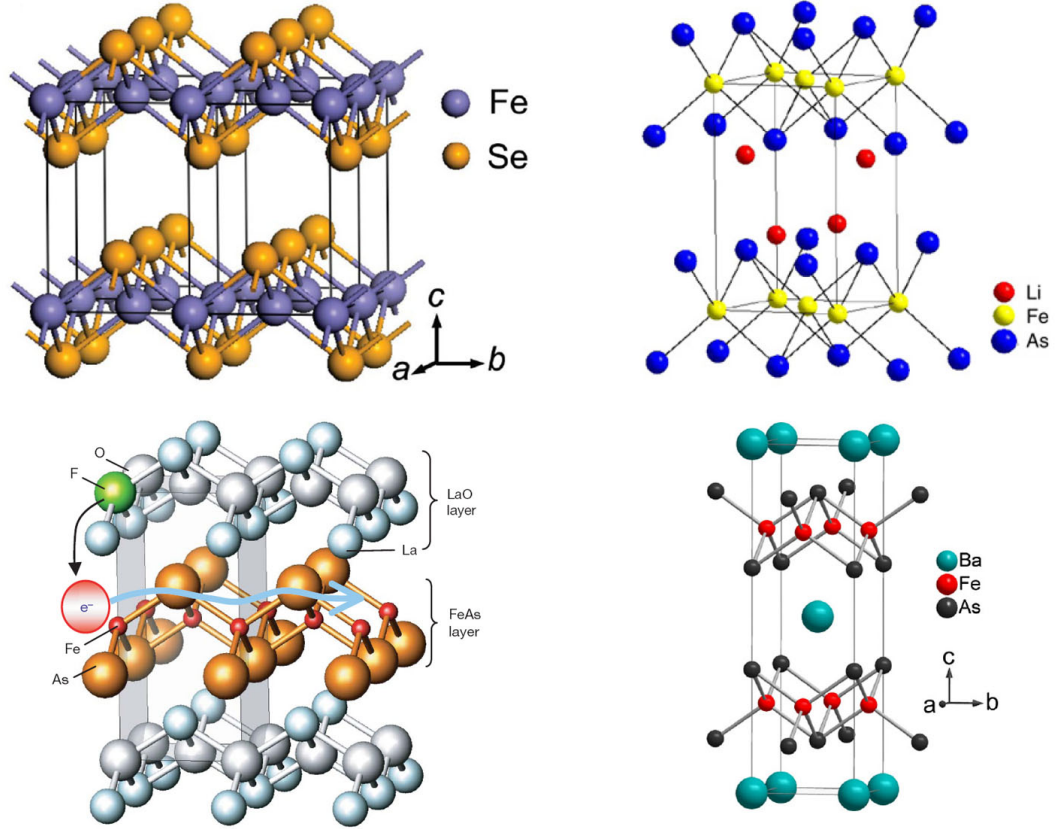
Figure 3.1: Illustration of the four different families of iron-based superconductors. **Upper left:** $FeSe$ as an example for the so called 11-family. Taken from [48]. **Upper right:** $LiFeAs$ exhibiting the 111-structure with a layer of Li in between the iron-arsenide layers. Taken from [49]. **Lower left:** $LaOFeAs$ representative for a 1111-family compound having a LaO spacer layer in between the $FeAs$ layers. One O-atom is replaced by flouride donating an extra electron to the iron-arsenide layer. Taken from [47]. **Lower right:** $BaFeAs$ from the 122-family with a Ba layer in between the $FeAs$ layers. Taken from [50].

with similar properties can be created. Many other compounds with this so called 1111-structure (name caused by the stoichiometry) exhibiting superconducting behavior were found, some of them with even higher transition temperatures, for example $T_c = 56K$ in $GdFeAsO$ [29]. Here Th doping istead of F doping lead to superconductivity. Another way to induce superconductivity in this structure of iron-arsenide is realized by oxygen-deficiency for example in the compound $NdFeAsO$ [51]. Moreover even doping directly into the iron-arsenide plane with Co in $CaFeAsF$ lead to superconductivity [52] which is quite remarkable since this introduces possible scattering centers into the plane where the important physics is happening. Besides the 1111-structure there are three other families of

iron based superconducting materials which are shown in Fig. 3.1 each of them represented by a specific example compound. They all share a layered structure containing a layer with an iron compound that is responsible for the superconductivity which makes their physical properties being considered highly two-dimensional. These compounds are usually referred to as iron-pnictide superconductors in the literature which is a proper name for the materials containing a layer that consist of iron and a member of the nitrogen group (pnictogens). However a strict interpretation of this name would exclude the compounds without a pnictogen that have to be included into this group of materials. Thus the name iron-based superconductors is chosen in this chapter as a general term for these materials. An example for a non-pnictide member of this material group is $FeSe$ which condenses in the PbO type structure (space group $P4/nmm$) displayed in the upper left of Fig. 3.1. This so called 11-structure is the simplest of the families having only layers of $FeSe$ without any spacing layers. Superconductivity is observed only with an intentional Se-deficiency with a T_c of $8K$ in $FeSe$ [48] and can be raised to $T_c = 27K$ under high pressure [53]. Furthermore it is reported that the substitution of Se with Te raises the transition temperature to a maximum of $15.2K$ at about a content of 50% Te in the compound [54] but $FeTe$ itself is not superconducting. The structure shown in the upper right of Fig. 3.1 is a Cu_2Sb type tetragonal structure (space group $P4/nmm$) called 111-structure and is represented by the compound $LiFeAs$. Li-deficiency leads to superconductivity with a maximum $T_c = 18K$ in the displayed material. In the lower right $BaFeAs$ as an example of the last structural family is illustrated. It condenses in $ThCr_2Si_2$-type structure (space group $I4/mmm$) which is called the 122-structre here. Superconductivity with a $T_c = 38K$ evolves with hole doping, explicitly meaning replacing Ba by K, in the displayed structure of $BaFeAs$ [50]. Also electron doping which is realized by inserting for example Co instead of Fe into the $FeAs$ plane of $BaFeAs$ [55] leads to superconductivity with a T_c of $22K$ in this example. Furthermore it is also possible to induce superconductivity by applying pressure to compounds of the 122-family reaching a maximum T_c of $29K$ [56, 57].

3.2   Electronic structure and superconducting gap

Short after the discovery of the iron-based superconducters the band structure was calculated for several different compounds. Density Functional Theory (DFT) studies in Local Density Approximation (LDA) were performed on $LaFeAsO$ (1111-family) [58] and showed a multi sheeted Fermi surface with two electron-like high-velocity cylinders around the zone edge $M - A$ line (corner of the 1. BZ), two hole-like lower-velocity cylinders around the $\Gamma - Z$ line (zone center) and an additional heavy 3D hole pocket that is centered at Z and intersects and anticrosses with the hole-like cylinders. Except for the latter one all other bands were found to be nearly two-dimensional and electron doping leads to a shrinking of the hole-like pockets because of their larger masses, especially the 3D hole pocket, making the Fermi surface even more 2D-like. Other DFT calculations with LDA for $BaFe_2As_2$ (122-family) and $LiFeAs$ (111-family) [59] lead to a very similar band structure with again two hole cylinders in the zone center for $BaFe_2As_2$ and an additional 3D hole pocket around Γ for $LiFeAs$ and two electron cylinders around the zone corner. This band structure was at first confirmed by Angular Resolved Photo Electron Spectroscopy (ARPES) measurements on F-doped $NdFeAsO$ (1111-family) showing a bigger hole-like nearly circular Fermi surface sheet (in higher resolution probably two distinct sheets) in the center of the 1. BZ and a smaller electron like pocket (also likely to be two) in the corner [62]. ARPES measurements on normal state $BaFe_2As_2$ (122-family) showed two hole-like Fermi surface sheets at the Γ-point and an electron-like pocket in the M-point with a four leaf-like deviation from a circle [63]. Another publication of ARPES measurements on the optimally ($x = 0.4$) K-doped superconducting $Ba_{1-x}K_xFe_2As_2$ found evidence that this structure in the corners are two distinct sheets with the inner one being almost circular and the outer one exhibiting the four leaf-structure [64] the two Γ-sheets were rather unchanged. More recent ARPES measurements on $Ba_{1-x}K_xFe_2As_2$ in the superconducting state [60] resolved that structure and showed that it consist of an electron pocket at the M point and four blades around it resulting in a propeller-like structure which was confirmed by another publication of the same group [61]. This data is displayed in Fig. 3.2 and will be used in Chapter 5 within a Free Electron Model to construct a Fermi surface that consists of two circular
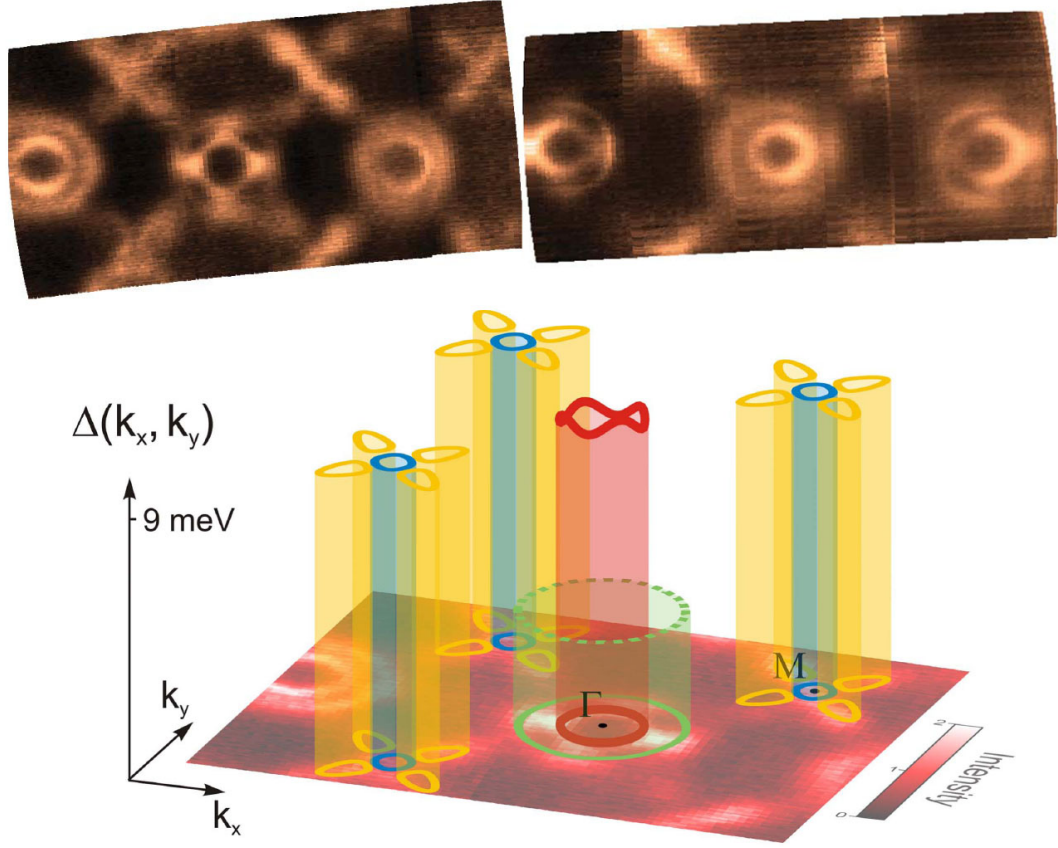
Figure 3.2: **Top:** ARPES measurements of the Fermi surface of superconducting $Ba_{1-x}K_xFe_2As_2$ with two different photon energies (left: $80eV$, right: $50eV$) at $T = 14K$. The two circles in the middle of both pictures (displayed three times) are the hole-like pockets around the Γ-point and the propeller-like structure is centered in the M-point. Taken from [60]. **Bottom:** Illustration of the above shown Fermi surface sheets with the corresponding superconducting gap value. The inner Γ-pocket and the bands in the propeller structre at the M-point have a bigger gap value than the outer Γ-pocket. Taken from [61].

hole-like bands in the Γ-point and a circular electron like band in the M-point surrounded by four elliptical blades. Moreover APRES measurements are capable of investigating the momentum dependence and value of the superconducting gap. It was shown that the gap of $Ba_{1-x}K_xFe_2As_2$ in the inner hole-like Γ-pocket as well as the one of the electron-like M-pocket exhibit a value of $\Delta_{big} \approx 12meV$ and that the outer hole-like Γ-pocket has a smaller gap with about $\Delta_{small} \approx 6meV$ [65]. Another publication obtains gap values for the bigger gap being $\Delta_{big} \approx 9meV$ [61] and the smaller gap being $\Delta_{small} \approx 1.1meV$ [66]. The latter one is not directly measured but obtained through a fit within the comparison of the penetration depth $\lambda(T)$ from ARPES and the muon-spin depolarization rate in muon

spin rotation measurements (μSR). Furthermore different μSR measurements find a bigger gap value of $\Delta_{big} \approx 6meV$ and a smaller gap value of $\Delta_{small} \approx 3meV$ [67]. An illustration of the distribution of the two different gap values throuout the 1. BZ is shown in Fig. 3.2. The smaller gap value is present at the outer hole-like sheet around Γ and all other bands show the bigger value. The ARPES measurements all show only a little variation of the gap (seen in Fig. 3.2 for the inner Γ-pocket) along the particular Fermi surface sheet and no evidence for gap nodes was obtained. The same is true for electron tunneling experiments [68] but Nuclear Magnetic Resonance (NMR) measurements point towards nodes in the gap [69]. This makes the question of the symmetry of the superconducting gap paremeter quite complicated since a nodeless gap excludes p-wave and d-wave pairing an favors an s-wave symmetry that is inconsistent with the NMR data. The symmetry favored by most publications, for example [70, 71], is and extended s-wave symmetry (or $s_{\pm}$-symmetry) that switches sign in between the Γ-point and M-point but has no nodes on the Fermi surface sheets. Inelastic neutron scattering measurements also point into this direction [72] and flux quantum transition measurements [73] claim to proof that the pairing must be spin-singlet with a sign change which also supports extended s-wave symmetry. Other theoretical studies show that the proposed extended s-wave gap parameter can explain the NMR data as well as the experiments showing a nodless gap [74]. Since most publications favor the extended s-wave symmetry this one will be chosen for the investigations including a nontrivial gap in Chapter 5. The analytical expression used there requires a maximum gap value Δ_0 which will be chosen to be $\Delta_0 = 10meV$ in sufficient agreement with the values given above. It has to be mentioned at this point that the issue of the gap symmetry is not entirely solved despite of all the experimental as well as theoretical work mentioned above supporting the extended s-wave gap with a sign change in between the Fermi surface sheets.

3.3 Phase diagram and physical properties

In contrast to the parent compounds of the high temperature superconducting cuprates, which are Mott insulators, the iron arsenide compounds, for exapmle $LaFeAsO$ [28], are found to be bad metals. Furthermore this material showed anomalies near $150K$ in both resistivity and DC magnetic susceptibility. Neutron scattering measurements revealed that

$LaFeAsO$ undergoes a structural phase transition at $155K$ where it changes its latice symmetry from tetragonal (space group P4/nmm) to monoclinic (space group P112/n) [75]. Another phase transition occurs at about $137K$ and the material develops a long-range spin density wave (SDW) type antiferromagnetic order below that temperature [75]. Fluorine doping suppresses both of these orderings and leads to superconductivity. Detailed
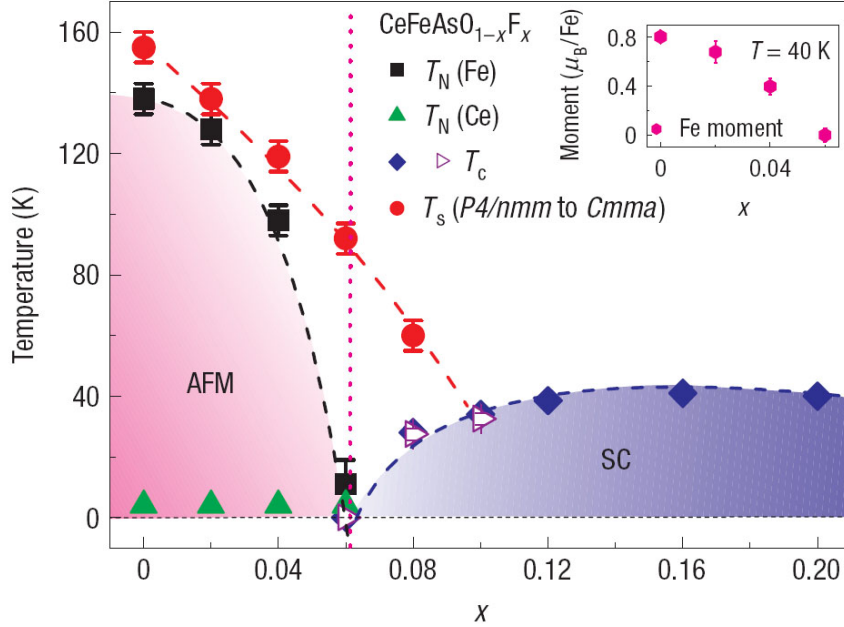
Figure 3.3: Phase diagram of $CeFeAsO_{1-x}F_x$. T_s is illustrated by the red circles and T_N for Fe and Ce are shown with black squares and green triangles respectively. All of these values are obtained by neutron scattering measurements of [76]. T_c obtained by susceptibility measurements in [76] is shown with open triangles and results from resistivity measurements of [77] are displayed with blue diamonds. The inset shows the doping dependence of the magnetic moment of the iron atoms at $40K$ where the influence of Ce on the Bragg peak of Fe is negligible. The error bars correspond to one standard deviation. Taken from [76].

measurements of the different critical temperatures (T_c for superconductivity, T_N for the antiferromagnetic ordering and T_s for the structural phase transition) were made on another member of the 1111-family, namely $CeFeAsO_{1-x}F_x$ [76, 77]. Here again a structural phase transition occurs at $T_c = 155K$ this time from the tetragonal (space group P4/nmm) to orthorhombic (space group Cmma) symmetry. The doping dependence of this structural transition is displayed in Fig. 3.3 by the red circles. The picture also shows the doping dependence of the antiferromagnetic transition T_N for Fe (black squares) as well as Ce

(green triangles), all obtained from neutron measurements. The critical temperature for superconductivity T_c obtained from resistivity measurements of a different publication [77] (blue diamonds) together with T_c results from susceptibility measurements (open triangles) are also displayed. The antiferromagnetic ordering of the parent compound is destroyed by doping and at a doping level of $x = 0.06$ superconductivity occurs with a rather smooth second order phase transition. This phase diagram is quite reminiscent of the one for the cuprates (for example Fig. 2.4). The phase diagram of $LaFeAsO_{1-x}F_x$ obtained from X-ray scattering, muon spin relaxation and Mössbauer spectroscopy [78] shows a different behavior with a much more abrupt (first order) phase transition from the SDW antiferromagnetism to superconductivity. For $BaFe_{2-x}Co_xAs_2$ a member of the 122-family the phase diagram does not show distinct phase transitions for the structure and the magnetic ordering [79]. Furthermore the antiferromagnetic order and suprconductivity seem to coexist at intermediate doping. The same was reported in $Ba_{1-x}K_xFe_2As_2$ [80]. Regarding the different results in compounds that all exhibit the same $FeAs$ layers it is obvious that at this point there is no consensus on a common behavior of the phase diagram. Also the exact character of the magnetic ordering is still under debate and the only thing that can be said at this early stage of this field of research is that more data is needed to unambiguously determine those properties. Also the pairing mechanism is far from being nailed down to one candidate. While some authors predict that superconductivity is mediated by antiferromagnetic spin fluctuations, for example [70], which is quite tempting due to the vicinity of magnetic ordering to the superconducting phase, the influence of phonons is also considered because of a strong Fe isotope effect of $\alpha = 0.35$ [81]. In other publications, for example [82], phonon mediated pairing is excluded because of the calculated phonon coupling constants being too small to explain the experimentally found T_c's. Furthermore the angle in between Fe and As and thus the perfection of the $Fe - As$ tetrahedron seems to have a big influence on T_c and with that on the superconducting mechanism [76]. Various other pairing mechanisms are also proposed but will not be mentioned here. An extensive theoretical review on the pairing symmetry and the pairing state in the iron-based superconductors is provided by [83].

Chapter 4

Raman Spectroscopy

In this chapter the theory of Raman scattering and several examples of experimental data of electronic Raman scattering will be presented. First the general theory, beginning with the perturbation Hamiltonian, will be shown and a direct proportionality of the scattering intensity to the imaginary part of the Raman susceptibility (or response function) will be developed. After that the effective mass approximation will be introduced for the computation of the Raman vertex and then the theory of electronic Raman scattering on a superconductor will be presented. In the second part an example for data of electronic Raman spectroscopy on a single band s-wave (BCS) superconductor will be illustrated first. Following that examples for Raman data on high temperature cuprate superconductors, hole and electron doped, and the multiband superconductor MgB_2 will be shown. These examples will demonstrate the possibilities of results obtained through electronic Raman scattering.

4.1   Theory of Raman scattering

4.1.1   General theory

Raman scattering is inelastic scattering of light, usually within or in the vicinity of the visible spectrum, by gaseous, liquid or solid matter. The intensity of the scattered light as a function of energy shift between the incoming and outgoing photons is measured with spectroscopic methods. Since this energy change of the photons corresponds to elementary excitations of the scattering material one gains information of the physics taking place in that material. Examples for those elementary excitations are phonons in solids and vibrations of molecules, which are historically the most important, but also electronic excitations

like magnons, excitons and, in the case of a superconducting probe, the breaking of Cooper pairs. At zero temperature the energy shift is always positive and the scattered photons loose part of their energy by creating such excitations. If excitations are already thermally created at finite temperatures the incident photon can gain energy and the energy shift is negative. The former is called Stokes and the latter anti-Stokes process. The interaction of light with electrons can be described by integrating the vector potential $\mathbf{A}(\mathbf{r}_j)$ into the Hamiltonian via the principle of least coupling to the momentum $\mathbf{p}_j$ of the jth electron, meaning $\mathbf{p}_j \rightarrow \mathbf{p}_j - \frac{e}{c}\mathbf{A}(\mathbf{r}_j)$. This leads to a perturbation Hamiltonian [84]

$$H' = \frac{1}{2m}\sum_j \left|\mathbf{p}_j - \frac{e}{c}\mathbf{A}(\mathbf{r}_j)\right|^2 - \frac{1}{2m}\sum_j \mathbf{p}_j^2 \tag{4.1}$$

where m is the electrons mass, e its charge ($e > 0$) and c the speed of light. Since Raman scattering is a two photon process one has to treat the part of H' proportional to $\mathbf{A}(\mathbf{r}_j)$, that is $H_A = -\frac{e}{mc}\sum_j \mathbf{A}(\mathbf{r}_j)\mathbf{p}_j$ (using transverse gauge: $\nabla\mathbf{A}(\mathbf{r}_j) = 0$), in second order perturbation theory. The part of H' being quadratic in $\mathbf{A}(\mathbf{r}_j)$, that is $H_{AA} = \frac{r_0}{2}\mathbf{A}^2(\mathbf{r}_j)$ (with the definition of the classic electron radius $r_0 = \frac{e^2}{mc^2}$), has to be treated in first order perturbation theory. The two Hamiltonians H_{AA} and H_A can be included in one effective Hamiltonian H_R, contributing to Raman scattering in linear response theory [85].

$$H_R = r_0 \left\langle A_S^\dagger A_L \right\rangle \tilde{\rho}_\mathbf{q} \tag{4.2}$$

Here $\mathbf{q} = \mathbf{k}_L - \mathbf{k}_S$ stands for the momentum transfered by the photon field to the sample with the momentum of the incident photon $\mathbf{k}_L$ and the scattered photon $\mathbf{k}_S$. The operators $A_S^\dagger$ and A_L contain the creation operator for the scattered photon and the annihilation operator for the incident photon respectively. Furthermore $\tilde{\rho}_\mathbf{q}$ denotes the effective density operator [85]

$$\tilde{\rho}_\mathbf{q} = \sum_{n,\mathbf{k}} \gamma_n(\mathbf{k}) c_{n,\mathbf{k}}^\dagger c_{n,\mathbf{k}} \tag{4.3}$$

where $c_{n,\mathbf{k}}^\dagger$ creates and $c_{n,\mathbf{k}}$ annihilates a Bloch electron in band n with momentum $\mathbf{k}$. The Raman vertex represented by $\gamma_n(\mathbf{k})$ will be specified later on. It is now the task to find an expression for the Raman scattering efficiency $\frac{d^2 R}{d\Omega d\omega}$ into a region in k-space $d\Omega d\omega$, with a Raman shift $\omega = \omega_L - \omega_S$ and a solid angle Ω, which has a relation to the

Raman susceptibility $\chi_{Raman}(\mathbf{q}, t)$. The latter quantity can be defined as the usual quantum mechanical thermal average of an operator in linear response theory [85]

$$\chi_{Raman}(\mathbf{q}, t) = \frac{i}{\hbar} Tr \left\{ \frac{e^{-\beta H_0}}{Z} \left[\tilde{\rho}_{\mathbf{q}}(t), \tilde{\rho}_{-\mathbf{q}}(0) \right] \right\} \tag{4.4}$$

with the partition function Z, the trace Tr and the usual thermodynamic definition of $\beta = k_B T$. A first step is made by multiplying the effective Hamiltonian in Eq. (4.2) with the time evolution factor $e^{-i\omega t}$ and inserting it into Fermi's golden rule.

$$\Gamma(\mathbf{k}_L, \mathbf{e}_L, \mathbf{k}_S, \mathbf{e}_s) = \frac{2\pi}{\hbar} \left| \langle f | H_R | i \rangle \right|^2 \delta \left(E_f - E_i - \hbar \omega \right) \tag{4.5}$$

Then a summation over the final states $|f\rangle$ of the the sample is made together with a thermal average over the initial states $|i\rangle$ giving a factor of $\sum_{i,f} \frac{e^{-i\beta E_i}}{Z}$ in the transition rate Γ^T [85]

$$\Gamma^T(\mathbf{k}_L, \mathbf{e}_L, \mathbf{k}_S, \mathbf{e}_s) = \frac{2\pi}{\hbar} r_0^2 \left| \left\langle A_S^\dagger A_L \right\rangle \right|^2 \sum_{i,f} \frac{e^{-i\beta E_i}}{Z} \left| \langle f | \tilde{\rho}_{\mathbf{q}} | i \rangle \right|^2 \delta \left(E_f - E_i - \hbar \omega \right) \tag{4.6}$$

Here $\left| \langle f | \tilde{\rho}_{\mathbf{q}} | i \rangle \right|^2$ represents a transition matrix element of the effective density operator between final and initial states. Since $\tilde{\rho}_{\mathbf{q}}$ contains the Raman vertex the transition probability also depends on this quantity leading to important consequences which will be discussed later. The delta distribution in Eq. (4.6) takes care of the necessary energy conservation, emphasizing the fact that the Raman shift equals the elementary excitation in the sample. The last part of Eq. (4.6) is usually referred to as the generalized dynamical structure factor $\tilde{S}^T$ of the sample [85].

$$\tilde{S}^T(\mathbf{q}, \omega) = \sum_{i,f} \frac{e^{-i\beta E_i}}{Z} \left| \langle f | \tilde{\rho}_{\mathbf{q}} | i \rangle \right|^2 \delta \left(E_f - E_i - \hbar \omega \right) \tag{4.7}$$

Next a summation over all final states within a region $d\Omega d\omega_S$ around $\mathbf{k}_S$ in k-space of Eq. (4.6) and a normalization to the incoming flux $\hbar c n_L$ is performed. The obtained differential Raman cross section $\frac{d^2\sigma}{d\Omega d\omega}$ is equal to the above mentioned Raman scattering efficiency $\frac{d^2R}{d\Omega d\omega}$ with the definition of the scattering volume as the unit volume [85]. Thus it follows

$$\frac{d^2R}{d\Omega d\omega} = \frac{\omega_S}{\omega_L} r_0^2 \tilde{S}^T(\mathbf{q}, \omega) \tag{4.8}$$

which shows a direct proportionality of the generalized dynamical structure factor to the Raman scattering efficiency. In the last step the fluctuation dissipation theorem [86] will

be used, which generally relates the imaginary part of the response function, representing energy dissipation, to a thermal fluctuation in the probe. In this case it leads to a direct correspondence of the dynamical structure factor $\tilde{S}^T(\mathbf{q}, \omega)$ to the imaginary part of the Fourier transformed Raman susceptibility $\chi_{Raman}(\mathbf{q}, \omega)$ [85].

$$\tilde{S}^T(\mathbf{q}, \omega) = -\frac{1}{\pi}(1 + n_\omega) Im\left[\chi_{Raman}(\mathbf{q}, \omega)\right] \tag{4.9}$$

where n_ω denotes the Bose factor $n_\omega = \frac{1}{e^{\beta \hbar \omega} - 1}$. Now inserting Eq. (4.9) into Eq. (4.8) leads to

$$\frac{d^2 R}{d\Omega d\omega} = -\frac{\omega_S}{\omega_L}\frac{r_0^2}{\pi}(1 + n_\omega) Im\left[\chi_{Raman}(\mathbf{q}, \omega)\right] \tag{4.10}$$

This shows the requested direct relation of the scattering efficiency to the imaginary part of the Raman susceptibility which allows us to predict the basic behavior of the Raman spectra with a calculation of the susceptibility of the examined material.

4.1.2 Effective mass approximation

The next important step, in order to arrive at a result that allows calculations for a real material, is to find a good approximation for the in Eq. (4.3) appearing Raman vertex. It can be written in the following way [85]

$$\gamma_n(\mathbf{k}) = \mathbf{e}_S^* \mathbf{e}_L + \sum_{n_m} \frac{\langle n\mathbf{k} + \mathbf{q}\, |\mathbf{e}_S^*\mathbf{p}|\, n_m\mathbf{k} + \mathbf{k}_L\rangle\, \langle n_m\mathbf{k} + \mathbf{k}_L\, |\mathbf{e}_L\mathbf{p}|\, n\mathbf{k}\rangle}{\epsilon_{n\mathbf{k}} - \epsilon_{n_m\mathbf{k} + \mathbf{k}_L} + \omega_L + i0}$$
$$+ \frac{\langle n\mathbf{k} + \mathbf{q}\, |\mathbf{e}_L\mathbf{p}|\, n_m\mathbf{k} - \mathbf{k}_S\rangle\, \langle n_m\mathbf{k} - \mathbf{k}_S\, |\mathbf{e}_S^*\mathbf{p}|\, n\mathbf{k}\rangle}{\epsilon_{n\mathbf{k}} - \epsilon_{n_m\mathbf{k} - \mathbf{k}_S} - \omega_S + i0} \tag{4.11}$$

where n_m denotes the band of the intermediate state, ϵ is the band energy dispersion and $\mathbf{e}_S$ and $\mathbf{e}_L$ are the polarization vectors of the scattered and incoming light respectively. Real interband transitions, meaning that the final and the initial states belong to different bands, are neglected. The first term arises from first order perturbation theory on the Hamiltonian H_{AA} and is only nonzero if the polarization vectors are not perpendicular to each other. The second and the third term are the result of second order perturbation theory of the Hamiltonian H_A. It can contribute to the Raman vertex, and therefore to the scattering efficiency, in various combinations of the polarization vectors, depending on the involved bands and their energy dispersion. It turns out that virtual intraband transitions $(n = n_m)$ are, up to first order in $\frac{v_F}{c}$, compared to virtual interband transitions of the order

of $\frac{\omega}{\omega_L} \ll 1$ and therefore negligible. Furthermore neglecting the incoming and scattered light frequencies ω_L and ω_S in the denominator of Eq. (4.11) and disregarding any resonance case the Raman vertex is brought into a form that is equivalent to the inverse effective mass in $\mathbf{k} \cdot \mathbf{p}$ theory. The effective mass tensor is defined as the inverse of the second derivative of the energy band dispersion with respect to k in the particular direction and can be seen as a way to remain a Newtonian form of mechanics within a periodic crystal potential. Performing this effective mass approximation on Eq. (4.11) the Raman vertex can be written as [85]

$$\gamma_n(\mathbf{k}) = \frac{m}{\hbar^2} \sum_{i,j} \mathbf{e}_{S,i}^* \frac{\partial^2 \epsilon_{n\mathbf{k}}}{\partial k_i \partial k_j} \mathbf{e}_{L,j} \tag{4.12}$$

Here one can see that it is the curvature of the energy band dispersion together with the light polarization vectors that determines which combinations of directions i and j contribute to Raman scattering and which ones vanish.

4.1.3 Theory of electronic Raman scattering on superconductors

After the general treatment of Raman scattering in the two previous subsections, now a specialization for the superconducting state is made. The quantity of interest is the Raman susceptibility according to the direct proportionality of its imaginary part to the scattering efficiency shown in Eq. (4.10). A first further simplification of $\chi_{Raman}(\mathbf{q}, \omega)$ can be made by restricting the treatment to the $\mathbf{q} \to 0$ limit. Since the incoming light wavelength is somewhere in or near the visible spectrum, with λ being in between 400Å and 800Å, and the usual order of a lattice constant a is of about 10Å it follows that $\frac{\pi}{a} \gg \frac{2\pi}{\lambda_L} = k_L$. So the value of the momentum difference $q = k_L - k_S$ is a lot smaller than the the Brillouin zone boundary value $\frac{\pi}{a}$ and the limitation to the Brillouin zone center, meaning $q \approx 0$, is certainly justified. An important fact that has to be taken into account is the Coulomb screening in the solid because the charge fluctuations excited by the Raman photons can be affected by it. Including screening the Raman susceptibility in the $\mathbf{q} \to 0$ limit can be written as [85]

$$\chi_{Raman}(\mathbf{q} \to 0, \omega) = \chi_{\gamma\gamma}(\omega) - \frac{\chi_{\gamma 1}^2(\omega)}{\chi_{11}(\omega)} \tag{4.13}$$

with

$$\chi_{ab}(\mathbf{q} \to 0, \omega) = \sum_{\mathbf{k}} a_{\mathbf{k}} b_{\mathbf{k}} \lambda_{\mathbf{k}}(\omega) \tag{4.14}$$

The last expression includes the Tsuneto function $\lambda_{\mathbf{k}}(\omega)$ [87]. For q being a lot smaller than the inverse of the coherence length ξ and the value of the Fermi wave vector k_F and for frequencies way below the Plasma frequency ω_p the Tsuneto function turns out to be [85]

$$\lambda_{\mathbf{k}}(\omega) = \frac{\Delta_{\mathbf{k}}^2}{E_{\mathbf{k}}^2} \tanh\left(\frac{E_{\mathbf{k}}}{2k_B T}\right) \left(\frac{1}{2E_{\mathbf{k}} + \hbar\omega + i\alpha} + \frac{1}{2E_{\mathbf{k}} - \hbar\omega - i\alpha}\right) \tag{4.15}$$

Here $\Delta_{\mathbf{k}}$ is the superconducting gap function and $E_{\mathbf{k}}^2 = \xi_{\mathbf{k}}^2 + \Delta_{\mathbf{k}}^2$ denotes the quasi particle excitation energy with the band dispersion relation $\xi_{\mathbf{k}} = \epsilon_{\mathbf{k}} - \epsilon_F$ relative to the Fermi energy as previously mentioned in the BCS theory. It is important to note that the second term in Eq. (4.13) which represents the screening vanishes if the average of $\gamma_{\mathbf{k}} \cdot \lambda_{\mathbf{k}}$ does. This is the case when the vertex does not transform according to the fully symmetric irreducible representation of the point group of the crystal since the Tsuneto function is always fully symmetric. Thus it is important what symmetry the vertex has and screening does not have to be taken into account for all symmetry channels.

4.2 Examples for electronic Raman spectroscopy experiments on superconductors

4.2.1 Single band s-wave superconductors

The first measurements which showed a new peak in the superconducting state that decreased with an external magnetic field were made by Sooryakumar and Klein [88] in 1980 on $2H - NbSe_2$. The example for electronic Raman scattering on regular s-wave superconductors with phonon mediated pairing presented here is data from experiments on Nb_3Sn. Since the gap in an s-wave superconductor is isotropic the peak referring to cooper pair breaking should be observed at the same energy in all symmetries. The data presented in Fig. 4.1 shows these peaks for the three symmetries E_g, T_{2g} and A_{1g} in Nb_3Sn with a critical temperature of $T_c = 18.0K$ [89]. In (a) the E_g symmetry is shown with the upper curve taken at $T = 1.8K$ and the lower curve at $T = 40K$. The larger peak corresponds to a

phonon and the additional peak below T_c has to arise from Cooper pair breaking. In (d) theoretical fits of those contributions are separately shown for the curve in the superconducting state together with a background contribution of electronic interband excitations. In the T_{2g} symmetry in (b) there is only a weak phoninic peak in the upper ($T = 1.8K$) as well as in the lower ($T = 40K$) curve and again a clear contribution from a superconducting gap below T_c could be measured. The lowest curve in (c) is the A_{1g} symmetry channel which
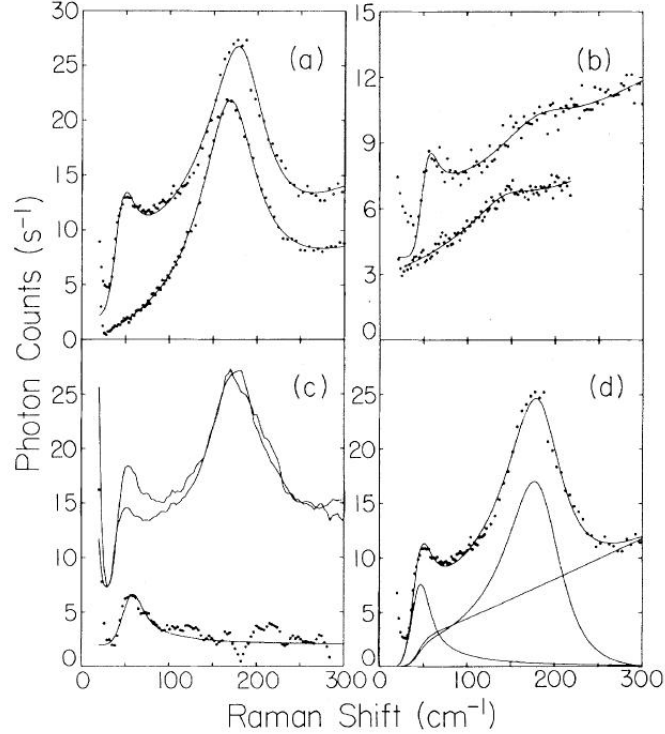
Figure 4.1: Raman spectra of Nb_3Sn. **(a)** Data and theoretical fits (solid curves) in E_g symmetry. In the upper curve ($T = 1.8K$) an additional peak to the phonon peak in the lower curve ($T = 40K$) appears. **(b)** The T_{2g} symmetry data and theoretical fits (solid curves) also show a new peak in the upper curve ($T = 1.8K$) that was not present in the lower curve ($T = 40K$). The phonon peak is very weak at both temperatures. **(c)** The top curve is data of $E_g + A_{1g}$ symmetry, the middle curve is data of E_g symmetry and the bottom curve is data of A_{1g} symmetry obtained by subtracting the middle curve from the top curve, all at $T = 1.8K$. The A_{1g} symmetry also shows a clear peak due to a superconducting gap and no phononic peak. The solid curve at the bottom is a theoretical fit. **(d)** The upper curve from (a) is shown with the three contributions that sum up to the theoretical fit. The smaller peak on the left arises from the superconducting gap, the large peak from the phonon and the linear part is the background contribution of electronic interband excitations. Original data from Dierker/Klein and Webb/Fisk [89].

was obtained by subtracting the middle curve from the top curve. Since there is no phonon

in this channel the peak can only be due to a direct measurement of the superconducting gap. In spite of the isotropy of the gap in this material, measured with other techniques, the E_g Cooper pair breaking peak is at lower energy than the ones in the other symmetry channels pointing towards a gap anisotropy. Furthermore the peaks are all smaller than those obtained by bulk methods. This lead to extensive discussions that first included the general fact that Raman spectroscopy is a surface sensitive method which usually obtains smaller gap values due to impurities on the surface. Measurements on freshly cleaved surfaces could rule out that explanation and showed that the gap values for the A_{1g} and T_{2g} symmetries are close to the ones obtained by bulk methods [90]. So the source of anisotropy had to be especially present in the E_g channel which points at the phonon that is quite dominant in the spectrum in this case. A final state interaction, meaning an interaction of the two single electrons of the broken Cooper pair with a channel orthogonal to the pairing channel, became a reasonable explanation since the strongly coupled E_g phonon is indeed orthogonal to the fully symmetric s-wave pairing channel. Together with symmetry arguments, the unique line shape of the E_g phonon and comparison to other gap measurements it were integrated spectral weight investigations that supported this explanation [90]. In the latter it was obvious that in the A_{1g} symmetry a new channel opened up below T_c which gained weight with decreasing temperature while the weight in the E_g channel was only slightly effected by temperature variation. It could be seen that the weight was transformed from the phonon to the bound state of the final state interaction with decreasing temperature which gave further evidence to that model. Thus no gap anisotropy had to be explained.

4.2.2 High temperature superconducting cuprates

Raman scattering measurements also played a role in revealing the nature of superconductivity in the high temperature cuprate superconductors. Fig. 4.2 shows one of the first Raman measurements on a hole doped cuprate superconductor, in this case $Bi_{2.2}Sr_{1.8}CaCu_2O_y$ [37]. The responses on the left hand side correspond to the $A_{1g} + B_{2g}$ symmetry channel and the ones on the right hand side to the $B_{1g} + (A_{2g})$ symmetry channel ((A_{2g}) is in brackets since its contribution is usually negligible). The peaks observed in the normal state (a) at $T = 140K$ are phonon excitations. In the superconducting state (b) the spectral weight gets
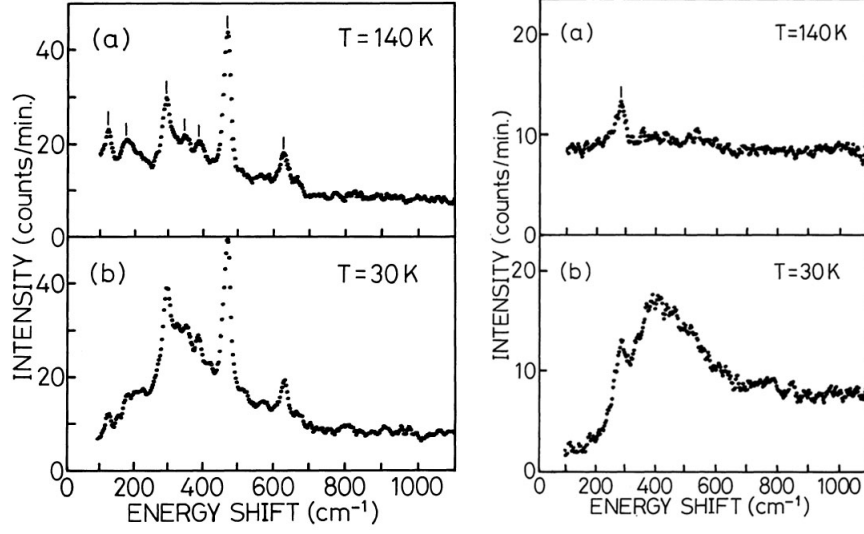
Figure 4.2: Data from Raman spectroscopy on the hole doped high temperature supercon-ductor $Bi_{2.2}Sr_{1.8}CaCu_2O_y$. The left panel shows $A_{1g} + B_{2g}$ symmetry and the right panel $B_{1g} + (A_{2g})$ symmetry in the normal (a) and superconducting state (b). In the latter one the response shows a redistribution at low energies and a broad peak at about $400cm^{-1}$ appears in the $B_{1g} + (A_{2g})$ symmetry. Taken from [37].

significantly redistributed and is much smaller at low energies. Furthermore a new peak is clearly seen in B_{1g} symmetry at about $400cm^{-1}$ and in $A_{1g} + B_{2g}$ symmetry a less obvious peak structure appears around roughly $300cm^{-1}$. While in the BCS-type superconductors a sharp onset of the new peaks at a threshold was observed in the superconducting state (see Fig. 4.1), corresponding to a fully gaped Fermi surface, the scattering intensity is increasing continuously at low energies in this material. A possible interpretation of this behavior was given by a superconducting gap with nodes along certain lines of the Fermi surface (later confirmed as d-wave pairing, see discussion in the extensive review [35]) and the difference in the position of the pair breaking peaks in the superconducting state can be seen as the first spectroscopic evidence for an anisotropic gap.

Raman response measurements also obtained results for electron doped cuprate su-perconductors which were discovered later than their hole doped relatives. The example presented in Fig. 4.3 shows Raman scattering on $Nd_{2-x}Ce_xCuO_4$ in A_{1g}, B_{1g} and B_{2g} symmetry [38]. In all symmetry channels the normal state response is almost constant and featureless in the shown energy range and in the superconducting state clear broad peaks appear at slightly different energies. An explanation for this difference requires a
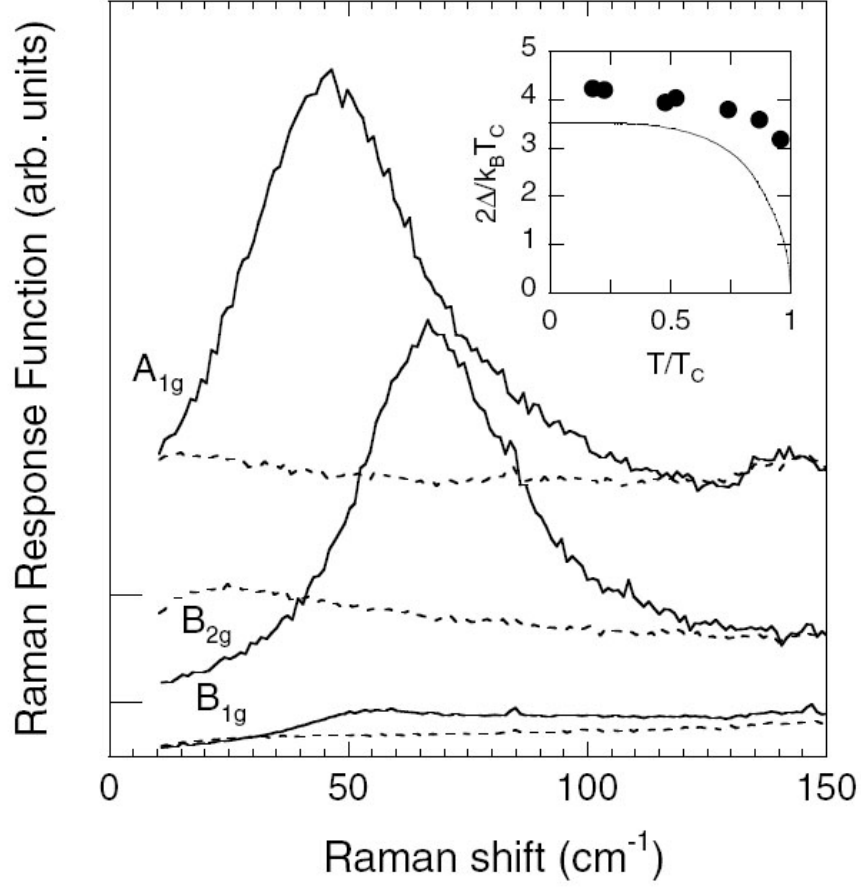
Figure 4.3: Raman scattering intensity of the electron doped superconductor $Nd_{2-x}Ce_xCuO_4$ in A_{1g}, B_{1g} and B_{2g} symmetry. The solid lines denote the response in the superconducting state at $T = 11K$ and the dashed lines denote the normal state response at $35K$. The ticks represent the shifts on the baselines. In the inset the temperature dependence of the 2Δ peak energy in the B_{1g} is shown together with the BCS mean field temperature dependence (solid line). Taken from [38].

knowledge about the measurement geometry and the form factor of each channel. The $B_{2g}(+A_{2g})$ (A_{2g} is again negligible) channel is measured in the $(\mathbf{e}_i, \mathbf{e}_s) = (xy)$ ($x = [100]$, $y = [010]$) geometry with $\mathbf{e}_i$ being the polarization direction of the incident and $\mathbf{e}_s$ the one of the scattered photon. Its form factor has $d_{x^2+y^2}$ symmetry which vanishes along the BZ diagonal $((0,0) \rightarrow (\pi, \pi)$ and equivalent lines) meaning the major contribution in this channel comes from the vicinity of the $(0, \pi)$ and equivalent points. The $B_{1g}(+A_{2g})$ channel is obtained in $(x'y')$ geometry ($x' = [110]$, $y' = [\bar{1}10]$) and has a form factor of d_{xy} symmetry that vanishes along $(0,0) \rightarrow (0, \pi)$ and equivalent lines exhibiting the major contribution

from the diagonal lines in the BZ and thus the $(\pi/2, \pi/2)$ and equivalent points with the here investigated Fermi surface. The (xx) geometry measures $A_{1g} + B_{1g}$ and the A_{1g} data is obtained by subtracting the $(x'y')$ response. The A_{1g} form factor is nonvanishing everywhere resulting in a contribution from the entire BZ. These form factors have a crucial influence on the interpretation of the data illustrated in Fig. 4.3 since the Cooper-pair breaking 2Δ peak in B_{1g} symmetry is at lower energies than the one in B_{2g} symmetry. This difference is evidence for the gap maximum being located near the $(\pi/2, \pi/2)$ point because this region is suppressed in the B_{1g} channel. The intensity differences of the peaks are explained through resonance effects and their general shape with a continuous onset instead of a threshold is evidence for nodes. In the inset of Fig. 4.3 the temperature dependence of the 2Δ peak location and thus its magnitude is compared to the mean field BCS behavior and a clear deviation is observed. In summary one can say that this data is an example for the possibilities of electronic Raman spectroscopy which is able to detect the presence of gap notes in a superconductor and to measure the magnitude as well as the anisotropy of the gap.

4.2.3 Multiband superconductor MgB_2

Electronic Raman scattering experiments were also performed on the multiband superconductor MgB_2 with a Fermi surface of four bands with two different gaps. Fig. 4.4 shows Raman data of this material in E_{2g} (top row) and A_{1g} (bottom row) symmetry for different excitation energies increasing from the left to the right [91]. The lager response in panel c is due to coherence effects of the band structure and is not seen in that magnitude in A_{1g} symmetry which can be explained by the screening in this channel. The normal state response (red) only shows a moderately featureless continuum that most likely has its origin in finite wave-vector effects. In the superconducting state (blue) the Raman response shows a redistribution with a broadened threshold structure at twice the smaller gap value Δ_0 without a peak. This is expected for a fully gaped superconductor with a coherence length larger than the optical penetration depth [84]. At twice the larger gap value Δ_l the coherence peak is obviously seen and its contribution to the solid line fit is shown in shaded violet. This peak exhibits a broadened square root singularity like structure expected for
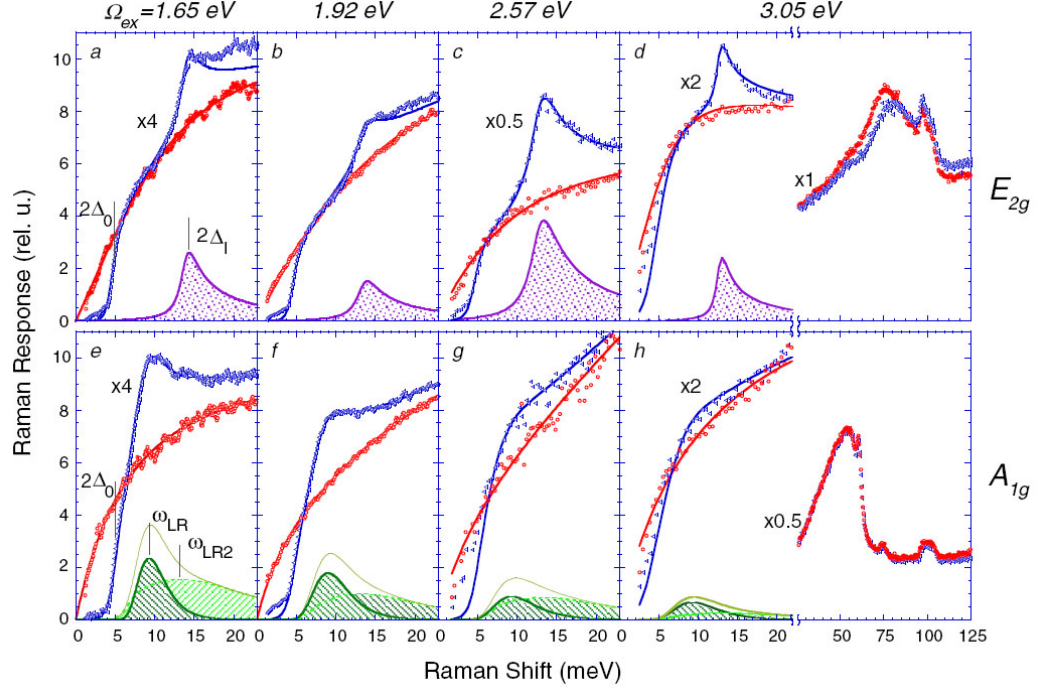
Figure 4.4: Raman response in E_{2g} and A_{1g} symmetry of the multiband superconductor MgB_2 for different excitation energies. The red responses are in the normal state at $T = 40K$ or in an external magnetic field of $5T$ and the blue responses are in the superconducting state at $T = 5 - 8K$. The solid lines are fits to the data which are solely determined by an electronic background continuum produced by finite wave-vector effects in the normal state. In E_{2g} symmetry (top row) the fits in the superconducting state consist of the electronic background continuum, a threshold at twice the smaller gap Δ_0 and a broadened peak at twice the larger gap Δ_l (shaded in violet). The superconducting A_{1g} (bottom row) response is fitted with the same electronic background continuum and threshold but with two peaks (sum denoted by thin green line) arising from collective modes at ω_{LR} (shaded in dark green) and ω_{LR2} (shaded in light green) caused by multiband effects. Taken from [91].

a constant gap superconductor. With the E_{2g} channel not transforming according to the fully symmetric irreducible representation of the crystals point group there are no screening effects in this channel. In contrast to that one would expect strong screening effects in the A_{1g} channel but there are clear peak structures seen in the response. The origin of those peaks are multiband effects in between the two distinct superconducting condensates explicitly meaning simultaneous cross tunneling of Cooper pairs from one condensate to the other and vice versa. This interband quasi particle scattering is only resulting in relative phase fluctuation of the two condensates and there is no net charge density fluctuation. So this mode is neutral and no screening occurs. Furthermore the strength of this peak can be

explained by the opposite signs of the two different bands involved. It can be shown that this mode is fully symmetric and hence only contributes to the A_{1g} symmetry response. The theoretical fits are shown in light and dark green and their sum is represented by the thin green line. While the sharper peak at ω_{LR} is shown to be due to the so called Leggett's mode [92] explained above the second one at ω_{LR2} might be of the same origin or an interference between superconducting contributions from two different bands. In the two panels on the very right the high energy contribution of phonons is also shown. In conclusion this data is another example for results obtained by Raman spectroscopy this time detecting a collective mode previously predicted by theory.

Chapter 5

Model calculations of Raman responses of multiband iron-based superconductors

In the beginning of this chapter the unscreened superconducting Raman response within a free electron model and at zero temperature will be calculated for an only angular dependent superconducting gap. The result will later be used to calculate the imaginary and with the Kramers-Krönig relation the real part of the Raman response function with a constant gap. This will make an analytical treatment of the Raman response including the screening term possible. Vertex corrections that take into account final state interactions of the excited quasi particles will not be considered and the Raman vertex will be obtained trough calculations using the effective mass approximation. Next investigations of multiband responses with a constant gap will be done analytically for all possible cases which will then be used to explain the Raman response of a multiband iron-based superconductor within a free electron band structure model based on ARPES measurements. After that a momentum dependent gap of extended s-wave symmetry will be introduced and the response will be calculated numerically with this gap. The obtained single band responses will be explained within a slightly simpler model of an only angular dependent gap and the investigated constant gap cases will be used to interpret the multiband features including screening. Finally the shortcomings of the applied model will be discussed and a comparison to earlier work will be presented before the results of the original work in this chapter will be summarized.

5.1 Raman response of a parabolic band structure without screening

As a first approach towards a realistic prediction of the Raman scattering efficiency given by Eq. (4.10) the simplifications of a free electron model will be applied leading to a parabolic band structure which symbolizes circular Fermi surface sheets. Furthermore the screening

term, second term on the right hand side of Eq. (4.13), will be neglected as well. This results in the direct proportionality of the Raman scattering efficiency to the imaginary part of the first term on the right side of Eq. (4.13). For n bands crossing the Fermi level the Raman response $\chi_{\gamma\gamma}(\omega)$ can be written, according to Eq. (4.14), in the following way

$$\chi_{\gamma\gamma}(\omega) = \frac{1}{N} \sum_{\mathbf{k}} \sum_{n} \gamma_n^2(\mathbf{k}) \lambda_n(\mathbf{k}, \omega) \tag{5.1}$$

with $\gamma_n(\mathbf{k})$ denoting the Raman vertex and $\lambda_n(\mathbf{k}, \omega)$ representing the Tsuneto function for the nth band. The expression of $\lambda_n(\mathbf{k}, \omega)$ in Eq. (4.15) is brought to the form

$$\lambda_n(\mathbf{k}, \omega) = \tanh\left(\frac{E_n(\mathbf{k})}{2k_B T}\right) \frac{4|\Delta_n(\mathbf{k})|^2}{E_n(\mathbf{k})[4E_n^2(\mathbf{k}) - (\omega + i\alpha)^2]} \tag{5.2}$$

$E_n(\mathbf{k})$ denotes the quasi particle energy of excited quasi particles from the superconducting condensate with $E_n^2(\mathbf{k}) = \epsilon_n^2(\mathbf{k}) + |\Delta_n(\mathbf{k})|^2$. Here again $\epsilon_n(\mathbf{k})$ is the band dispersion and $\Delta_n(\mathbf{k})$ stands for the superconducting energy gap parameter. Furthermore $\hbar$ has been absorbed in ω which has now energy units. For a further simplification of the treatment only the case of absolute zero temperature will be considered at this point. At $T = 0$ we can set $\tanh\left(\frac{E_n(\mathbf{k})}{2k_B T}\right) = 1$ and after taking the imaginary part of Eq. (5.1) we arrive at

$$Im\left(\chi_{\gamma\gamma}(\omega)\right) = \frac{1}{N} \sum_{\mathbf{k}} \sum_{n} \gamma_n^2(\mathbf{k}) \frac{4|\Delta_n(\mathbf{k})|^2}{E_n(\mathbf{k})} \frac{2\omega\alpha}{(4E_n^2(\mathbf{k}) - \omega^2 + \alpha^2)^2 + (2\omega\alpha)^2} \tag{5.3}$$

Now taking $\lim_{\alpha \to 0}$ of Eq. (5.3) and using the representation of the delta distribution as a limit of a Lorentzian function

$$\lim_{a \to 0} \frac{1}{\pi} \frac{a}{x^2 + a^2} = \delta(x) \tag{5.4}$$

we obtain

$$Im\left(\chi_{\gamma\gamma}(\omega)\right) = \frac{1}{N} \sum_{\mathbf{k}} \sum_{n} \gamma_n^2(\mathbf{k}) \frac{4|\Delta_n(\mathbf{k})|^2}{E_n(\mathbf{k})} \pi \delta(4E_n^2(\mathbf{k}) - \omega^2) \tag{5.5}$$

Here it is important to note that Eq. (5.4) is restricted to $a > 0$ this means that ω has to be a finite positive quantity. For the case of $T = 0$ this is certainly true since there are no thermal excitations of which the photon can gain energy from but for finite temperatures also negative ω have to be considered. However, at this point ω is taken to be positive. After exchanging the sum over $\mathbf{k}$, meaning a double sum over k_x and k_y, by a two dimensional integral in k-space and going to polar coordinates in the following way

$$\sum_{\mathbf{k}} \to \frac{NA}{(2\pi)^2} \int dk_x \int dk_y = \frac{NA}{(2\pi)^2} \int_0^{2\pi} d\theta \int_0^\infty k\,dk = \frac{NA}{(2\pi)^2} \int_0^{2\pi} d\theta \int_0^\infty \frac{1}{2} d(k^2) \tag{5.6}$$

with N being the number of unit cells and A denoting the unit cell area, further specification of $E_n(\mathbf{k})$ has to be made. Assuming the paraboloid band dispersion of a free electron model with the Fermi energy ϵ_F, that is equal to the chemical potential μ at $T = 0$, as the zero energy value and the energy gap only depending on the angel the quasi particle energy becomes

$$E_n^2(\mathbf{k}) = \left(\frac{k^2}{2m^*} - \mu\right)^2 + |\Delta_n(\theta)|^2 = x^2 + |\Delta_n(\theta)|^2 \tag{5.7}$$

Here the transformation $x = \frac{k^2}{2m^*} - \mu$ was made leading to $d(k^2) = 2m^*dx$ in the integration. The quantity m^*, in which $\hbar^2$ and several other constants for a convenient transformation into the later used units (defined in the next section) have been absorbed, is the effective mass of the free electron band that corresponds to the curvature of the parabolic band. Also taking the vertex to be only angle dependent Eq. (5.5) results in

$$Im\left(\chi_{\gamma\gamma}(\omega)\right) = \sum_n \frac{m^*A}{\pi} \int_0^{2\pi} d\theta \int_0^\infty dx \gamma_n^2(\theta) \frac{|\Delta_n(\theta)|^2}{\sqrt{x^2 + |\Delta_n(\theta)|^2}}$$
$$\times \delta\left(4x^2 + 4|\Delta_n(\theta)|^2 - \omega^2\right) \tag{5.8}$$

To execute the delta distribution, containing a function of more than one root, one has to use the formula

$$\delta(g(x)) = \sum_n \frac{1}{|g'(x_n)|} \delta(x - x_n) \tag{5.9}$$

with $g'(x_n)$ denoting the first derivative of $g(x)$ at the nth root x_n of $g(x)$. In this case

$$g(x) \equiv 4x^2 + 4|\Delta_n(\theta)|^2 - \omega^2$$
$$x_{1/2} = \pm\frac{1}{2}\sqrt{\omega^2 - 4|\Delta_n(\theta)|^2} \tag{5.10}$$
$$g'(x_{1/2}) = \pm 4\sqrt{\omega^2 - 4|\Delta_n(\theta)|^2}$$

Now inserting Eq. (5.9) and Eq. (5.10) into Eq. (5.8) I get

$$Im\left(\chi_{\gamma\gamma}(\omega)\right) = \sum_n \frac{m^*A}{\pi} Re\left[\int_0^{2\pi} d\theta \int_0^\infty dx \gamma_n^2(\theta) \frac{|\Delta_n(\theta)|^2}{\sqrt{x^2 + |\Delta_n(\theta)|^2}}\right.$$
$$\times \left[\frac{1}{4\sqrt{\omega^2 - 4|\Delta_n(\theta)|^2}} \delta\left(x - \frac{1}{2}\sqrt{\omega^2 - 4|\Delta_n(\theta)|^2}\right)\right.$$
$$\left.\left. + \frac{1}{4\sqrt{\omega^2 - 4|\Delta_n(\theta)|^2}} \delta\left(x + \frac{1}{2}\sqrt{\omega^2 - 4|\Delta_n(\theta)|^2}\right)\right]\right] \tag{5.11}$$

The $Re[\ ]$ is inserted to keep the whole function real if the argument of the square root gets negative for $\omega^2 < 4\,|\Delta_n(\theta)|^2$ and produces an i. After executing the delta distributions together with the integral over x I obtain

$$
\begin{aligned}
Im\,(\chi_{\gamma\gamma}(\omega)) &= \sum_n \frac{m^*A}{4\pi}\,Re\left[\int_0^{2\pi} d\theta\gamma_n^2(\theta)\frac{|\Delta_n(\theta)|^2}{\sqrt{\omega^2 - 4\,|\Delta_n(\theta)|^2}}\left[\frac{2}{\omega} + \frac{2}{\omega}\right]\right] \\
&= \sum_n \frac{m^*A}{\pi}\frac{1}{\omega}\,Re\left[\int_0^{2\pi} d\theta\gamma_n^2(\theta)\frac{|\Delta_n(\theta)|^2}{\sqrt{\omega^2 - 4\,|\Delta_n(\theta)|^2}}\right]
\end{aligned}
\tag{5.12}
$$

Using $N_{F,n}$ for the density of states in 2D with $N_{F,n} = \left|\frac{m^*A}{\pi}\right|$ this can be written as

$$
Im\,(\chi_{\gamma\gamma}(\omega)) = \sum_n \frac{N_{F,n}}{\omega}\,Re\left[\int_0^{2\pi} d\theta\gamma_n^2(\theta)\frac{|\Delta_n(\theta)|^2}{\sqrt{\omega^2 - 4\,|\Delta_n(\theta)|^2}}\right]
\tag{5.13}
$$

Taking the density of states to be a constant is certainly reasonable in the vicinity of the Fermi level but if one looks further apart of the Fermi energy and reaches the bottom or top of the parabola this is no longer true. Above the top of the band or below its bottom the density of states should be vanishing which could be realized by a cutoff at the particular energy (chemical potential) of the band. Since the focus of the Raman responses calculated in this chapter lies on the energy region near the Fermi level the cutoff will be neglected at this point. However for the k-dependent gap used later on this feature will reappear since the simplification done at this point is tied to the analytical calculations which are replaced by numerics in that case. If one only considers one band in Eq. (5.13) complications from interplay of different bands don't exist and the sum over n can be dropped in this expression. In the simplest case the energy gap Δ is a constant and has no angular dependence. Then the whole fraction containing Δ can be put out of the integral which turns out to be just a constant for a nonvanishing vertex of a form transforming according to the crystal's symmetry point group. It can easily be seen now that there is square root singularity at $\omega = 2\Delta$ and that the function is equal to zero below that singularity since the square root gets imaginary in this region.

5.2 Raman response of a free electron band structure based on data from ARPES experiments

5.2.1 Band structure

In the next step the preceding calculations for one parabolic band will be extended by integrating experimental results from Angular Resolved Photo Electron Spectroscopy (ARPES). Recent publications [60, 61, 66] showed that several bands are crossing the Fermi level (see Fig. 3.2). There are two hole-like bands around the Γ-point and an electron-like band around the M-point which is surrounded by four additional hole-like bands forming a propeller-like structure. This experimentally observed structure will be approximated with a free electron model which is actually a reasonable starting point since the deviation from parabolicity is only small at the Fermi level. The hole-like pockets around the Γ-point and the electron-like pocket around the M-point will be represented as parabolas including the experimentally observed effective masses, crossing points with the Fermi level and the corresponding top or bottom of the band. The blades of the propeller show a more elliptical shape which will be taken into account by different effective masses along the $k_x + k_y$ and $k_x - k_y$ directions so that the top of the band and the crossing point with the Fermi level fit the data. These assumptions lead to the following representations for the parabolas

$$\epsilon_i(\mathbf{k}) = \frac{1}{2m_i^*} \left((k_x - n)^2 + (k_y - h)^2 \right) - \mu_i \tag{5.14}$$

Here i means the inner Γ-parabola (Γi), the outer Γ-parabola (Γo) or the M-pocket (Mp) and m_i^* and μ_i are the corresponding effective mass and chemical potential respectively. The effective mass is in this case defined as $m_i^* = \frac{xmea^2}{\hbar^2\pi^2} \times 10^{-3}$ where x is a the number of electron masses m describing the curvature of the particular band, e is the absolute value of the electrons charge and a is the lattice constant of the back folded BZ (doubled unit cell in real space) and will be taken $\sqrt{2} \cdot 3.90\text{Å}$ according to [93]. This definition is chosen in this way to carry the units of inverse energy and to transform the effective mass for the inserted number of electron masses to the same units as μ which is used in meV. This also
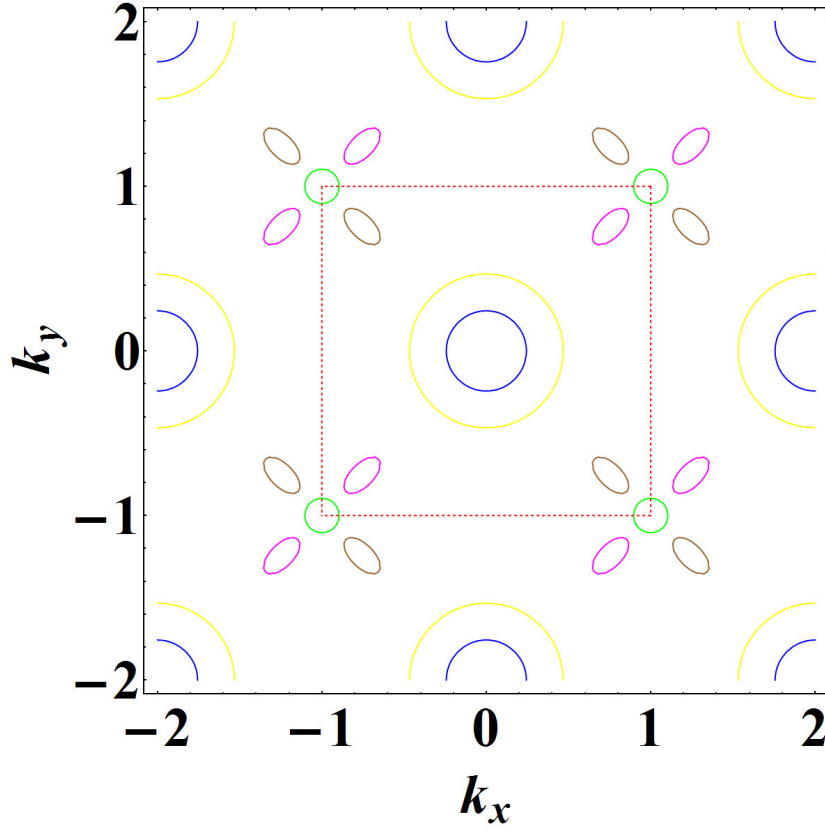
Figure 5.1: Illustration of the bands crossing the Fermi level in the free electron model. The inner Γ-parabola is blue, the outer Γ-parabola is yellow, the M-pocket is green and the propeller blades are magenta and brown. The M-pocket is electron-like and the rest of the band is hole-like. The red dashed square encloses the 1. BZ.

means that k_x and k_y run from -1 to 1 for the first BZ and are bare numbers. The ellipses will be represented by

$$
\epsilon_{bl}(\mathbf{k}) = \frac{1}{2m^*_{x+y}} \left\{ \frac{\left[\left(k_x - \left(n + \frac{0.346}{\sqrt{2}}\xi_1\right)\right) + \left(k_y - \left(h + \frac{0.346}{\sqrt{2}}\xi_2\right)\right)\right]}{\sqrt{2}} \right\}^2
$$
$$
+ \frac{1}{2m^*_{x-y}} \left\{ \frac{\left[\left(k_x - \left(l + \frac{0.346}{\sqrt{2}}\xi_3\right)\right) - \left(k_y - \left(o + \frac{0.346}{\sqrt{2}}\xi_4\right)\right)\right]}{\sqrt{2}} \right\}^2 - \mu_{bl}
$$

(5.15)

with m^*_{x+y} being the effective mass in the $k_x + k_y$ direction, m^*_{x-y} the effective mass in the $k_x - k_y$ direction, defined analog to m^*_i, and μ_{bl} denoting the chemical potential of the blades. In both equations $n, h, l, o \in \mathbb{Z}$ and $\xi_{1,2,3,4} = -1, 0, 1$. The value $\frac{0.346}{\sqrt{2}}$ is extracted from [60]. The crossing of the Fermi level in free electron approximation of the ARPES

Table 5.1: Effective masses and chemical potentials used for Fig. 5.1.

band	inner Γ-par.	outer Γ-par.	M-pocket	blade
effective mass $[m_e]$	-2.1	-6	0.8	-0.61, -2.46
chemical potential $[meV]$	35	45	-17	10

data is shown in Fig. 5.1. The first BZ contains one inner Γ-parabola (blue), one outer Γ-parabola (yellow), one M-pocket (green) and four blades (two bown and two magenta ones) and is illustrated by the red dashed square. For presentation purposes a larger area is shown where the propeller structure is more obvious. The chemical potentials and effective masses used for this illustration are shown in Table 5.1.

5.2.2 Raman verteces

The calculations for the Raman response with the bands in Eq. (5.14) and Eq. (5.15) are almost entirely analog to those done in the previous section. The main difference now will be that an explicit form of the Raman vertex is obtained by the effective mass approximation in Eq. (4.12). Furthermore group theoretical arguments determine the composition of the different entries of the effective mass tensor to the particular Raman vertex. A matrix element $M_{F,I} = M_{I,F}^{\alpha,\beta} e_i^\alpha e_s^\beta$ can be decomposed into the basis functions of the irreducible representations of the point group describing the crystal. Here the assumption of tetragonal, two dimensional lattice structure will be made which results in the decomposition [35]

$$
\begin{aligned}
M_{F,I} &= \frac{1}{2} O_{A_{1g}} (e_i^x e_s^x + e_i^y e_s^y) + \frac{1}{2} O_{B_{1g}} (e_i^x e_s^x - e_i^y e_s^y) \\
&+ \frac{1}{2} O_{B_{2g}} (e_i^x e_s^y + e_i^y e_s^x) + \frac{1}{2} O_{A_{2g}} (e_i^x e_s^y - e_i^y e_s^x)
\end{aligned}
\tag{5.16}
$$

Here O_μ is the projected operator into the particular irreducible representation and $e_{i,s}^\alpha$ is the incident (i) and scattered (s) light polarization. For $q = 0$ there is no mixing between the representations which means that the correlation functions of the Operators O_μ are

independent of each other. This leads to the following Raman verteces for the parabolic band in Eq. (5.14)

$$
\begin{aligned}
\gamma^i_{A_{1g}} &= \frac{m}{2\hbar^2}\left(\frac{\partial^2\epsilon_i(\mathbf{k})}{\partial_{k_x}\partial_{k_x}} + \frac{\partial^2\epsilon_i(\mathbf{k})}{\partial_{k_y}\partial_{k_y}}\right) = \frac{1}{\hbar^2}\frac{m}{m_i^*} \\
\gamma^i_{B_{1g}} &= \frac{m}{2\hbar^2}\left(\frac{\partial^2\epsilon_i(\mathbf{k})}{\partial_{k_x}\partial_{k_x}} - \frac{\partial^2\epsilon_i(\mathbf{k})}{\partial_{k_y}\partial_{k_y}}\right) = 0 \\
\gamma^i_{B_{2g}} &= \frac{m}{2\hbar^2}\left(\frac{\partial^2\epsilon_i(\mathbf{k})}{\partial_{k_x}\partial_{k_y}} + \frac{\partial^2\epsilon_i(\mathbf{k})}{\partial_{k_y}\partial_{k_x}}\right) = 0 \\
\gamma^i_{A_{2g}} &= \frac{m}{2\hbar^2}\left(\frac{\partial^2\epsilon_i(\mathbf{k})}{\partial_{k_x}\partial_{k_y}} - \frac{\partial^2\epsilon_i(\mathbf{k})}{\partial_{k_y}\partial_{k_x}}\right) = 0
\end{aligned}
\tag{5.17}
$$

So the only channel contributing to the Raman response for a parabolic band is the fully symmetric A_{1g} channel all others vanish. For the elliptical band in Eq. (5.15) one obtains the verteces

$$
\begin{aligned}
\gamma^{bl}_{A_{1g}} &= \frac{m}{2\hbar^2}\left(\frac{\partial^2\epsilon_{bl}(\mathbf{k})}{\partial_{k_x}\partial_{k_x}} + \frac{\partial^2\epsilon_{bl}(\mathbf{k})}{\partial_{k_y}\partial_{k_y}}\right) = \frac{m}{2\hbar^2}\left(\frac{1}{m^*_{x+y}} + \frac{1}{m^*_{x-y}}\right) \\
\gamma^{bl}_{B_{1g}} &= \frac{m}{2\hbar^2}\left(\frac{\partial^2\epsilon_{bl}(\mathbf{k})}{\partial_{k_x}\partial_{k_x}} - \frac{\partial^2\epsilon_{bl}(\mathbf{k})}{\partial_{k_y}\partial_{k_y}}\right) = 0 \\
\gamma^{bl}_{B_{2g}} &= \frac{m}{2\hbar^2}\left(\frac{\partial^2\epsilon_{bl}(\mathbf{k})}{\partial_{k_x}\partial_{k_y}} + \frac{\partial^2\epsilon_{bl}(\mathbf{k})}{\partial_{k_y}\partial_{k_x}}\right) = \frac{m}{2\hbar^2}\left(\frac{1}{m^*_{x+y}} - \frac{1}{m^*_{x-y}}\right) \\
\gamma^{bl}_{A_{2g}} &= \frac{m}{2\hbar^2}\left(\frac{\partial^2\epsilon_{bl}(\mathbf{k})}{\partial_{k_x}\partial_{k_y}} - \frac{\partial^2\epsilon_{bl}(\mathbf{k})}{\partial_{k_y}\partial_{k_x}}\right) = 0
\end{aligned}
\tag{5.18}
$$

Here A_{1g} as well as B_{2g} are nonzero so two channels contribute to the Raman response. It is important to note that the magenta blades in Fig. 5.1 have the larger effective mass along the $k_x + k_y$ direction while the larger effective mass of the brown blades is the one along the $k_x - k_y$ direction.

5.2.3 Constant superconducting gap parameter

Unscreened Raman responses

The assumption of $T = 0$ and thus $\omega > 0$ is still applied. Furthermore the energy gap parameter Δ will now taken to be just a constant. Hence the calculation of the imaginary part of the Raman response for the parabolic bands for the A_{1g} channel results in

$$Im\left(\chi_{\gamma\gamma}^{i,A_{1g}}(\omega)\right) = \frac{2\pi}{\hbar^4} N_{F,i} \left(\frac{m}{m_i^*}\right)^2 Re\left[\frac{\Delta_i^2}{\omega\sqrt{\omega^2 - 4\Delta_i^2}}\right] \tag{5.19}$$

Since the inner and outer Γ-parabola are centered around the point of origin in k-space no coordinate shift had to be done while performing the calculation. For the M-pocket the point of origin is taken to be the M-point by shifting $k_{x,y} \to k'_{x,y} + 1$. The transformation to polar coordinates is analog to the one in the previous section and the variable x over which the delta distribution is executed is again $x = \frac{k^2}{2m_i^*} - \mu_i$ leading to $d(k^2) = 2m_i^* dx$ and the density of states is $N_{F,i} = \left|\frac{m_i^* A}{\pi}\right|$. Realizing that there is no angular dependence the integral over θ gives the extra factor of 2π while the remaining difference to Eq. (5.13) evolves from the now explicitly evaluated Raman vertex $\gamma_{A_{1g}}^i$ in Eq. (5.17). For the now following evaluation of the imaginary part of the Raman response of the elliptical bands $\epsilon_{bl}(\mathbf{k})$ one has to be a little more careful. First of all the point of origin is is taken to be in the middle of the ellipse which is realized by setting all parameters $(n, h, l, o, \xi_{1,2,3,4})$ to zero. Then transformation $K_x = \frac{k_x + k_y}{\sqrt{2}}$ and $K_y = \frac{k_x - k_y}{\sqrt{2}}$ is done. The absolute value of the Jacobi determinant for this transformation is unity showing that it is area conserving and thus $dk_x dk_y = dK_x dK_y$. To be able to evaluate the integral in the same way as before another transformation $K_y = \sqrt{\frac{m_{x-y}^*}{m_{x+y}^*}} K'_y$ is applied in order to rescale the coordinate axes. This effects the integration since $dK_y = \sqrt{\frac{m_{x-y}^*}{m_{x+y}^*}} dK'_y$. The resulting band equation is

$$\tilde{\epsilon}_{bl}(\mathbf{k}) = \frac{1}{2m_{x+y}^*}\left(K_x^2 + K_y'^2\right) + \mu_{bl} \tag{5.20}$$

This looks entirely equal to Eq. (5.14) with $n = h = 0$ so the computation is again analog to the one for a parabolic band. Transforming again into polar coordinates, using this time

$x = \frac{K^2}{2m^*_{x+y}} - \mu_{bl}$ with $K^2 = K_x^2 + K_y'^2$ and inserting the Raman vertex for A_{1g} symmetry one obtains

$$Im\left(\chi_{\gamma\gamma}^{bl,A_{1g}}(\omega)\right) = \frac{2\pi}{\hbar^4}N_{F,bl}\frac{m^2}{4}\left(\frac{1}{m^*_{x+y}} + \frac{1}{m^*_{x-y}}\right)^2 Re\left[\frac{\Delta_{bl}^2}{\omega\sqrt{\omega^2 - 4\Delta_{bl}^2}}\right] \tag{5.21}$$

With the Raman vertex in B_{2g} symmetry the result is

$$Im\left(\chi_{\gamma\gamma}^{bl,B_{2g}}(\omega)\right) = \frac{2\pi}{\hbar^4}N_{F,bl}\frac{m^2}{4}\left(\frac{1}{m^*_{x+y}} - \frac{1}{m^*_{x-y}}\right)^2 Re\left[\frac{\Delta_{bl}^2}{\omega\sqrt{\omega^2 - 4\Delta_{bl}^2}}\right] \tag{5.22}$$

Here the density of states is taken to be $N_{F,bl} = \frac{\sqrt{m^*_{x+y}m^*_{x-y}}A}{\pi}$. Both the A_{1g} and the B_{2g} result show an invariance towards exchange of the effective masses m^*_{x+y} and m^*_{x-y} which means that all four blades contribute in the same way despite of their different orientation. Furthermore both results properly reduce to the parabolic case if one sets the two effective masses equal meaning the result displayed in Eq. (5.21) is equal to the one in Eq. (5.19) and the one in Eq. (5.22) is equal to zero. The entire Raman response without screening is just the sum of the responses of the different bands resulting for A_{1g} symmetry in

$$\begin{aligned} Im\left(\chi_{\gamma\gamma}^{A_{1g}}(\omega)\right) = &\ Im\left(\chi_{\gamma\gamma}^{\Gamma i,A_{1g}}(\omega)\right) + Im\left(\chi_{\gamma\gamma}^{\Gamma o,A_{1g}}(\omega)\right) \\ &+ Im\left(\chi_{\gamma\gamma}^{Mp,A_{1g}}(\omega)\right) + 4 \times Im\left(\chi_{\gamma\gamma}^{bl,A_{1g}}(\omega)\right) \end{aligned} \tag{5.23}$$

In B_{2g} symmetry only the blades contribute and the response is

$$Im\left(\chi_{\gamma\gamma}^{B_{2g}}(\omega)\right) = 4 \times Im\left(\chi_{\gamma\gamma}^{bl,B_{2g}}(\omega)\right) \tag{5.24}$$

Real part of the response function

The last thing that has to be added to the free electron band structure model in order to calculate a realistic Raman response is the screening represented by the second term on the right hand side of Eq. (4.13). This term is only nonvanishing in the totally symmetric A_{1g} symmetry. In contrast to the unscreened term there is now a possibility of cross terms between the response functions of different bands in the numerator leading to a dependence of the Raman response on the real part of the response function. Thus this term has to be calculated as well. This calculation can be done with the Kramers-Krönig relation

which relates the real part of a response function $\chi'(\omega)$ to the imaginary part $\chi''(\omega)$ via the equation [86]

$$\chi'(\omega) = \frac{1}{\pi} P \int_{-\infty}^{\infty} \frac{\chi''(\omega')}{\omega' - \omega} d\omega' \tag{5.25}$$

P denotes the Cauchy principle value of the integral which usually contains singularities that require special care during the calculation. Using that $\chi'(\omega)$ is always an even and $\chi''(\omega)$ is always an odd function of ω one obtains the Kramers-Krönig relation in the following form

$$\chi'(\omega) = \frac{2}{\pi} P \int_{0}^{\infty} \frac{\omega' \cdot \chi''(\omega')}{\omega'^2 - \omega^2} d\omega' \tag{5.26}$$

Now inserting the previously obtained imaginary part of the response function $Im\left(\chi_{\gamma\gamma}^{n,A_{1g}}\right)$ for the nth band leads to

$$Re\left(\chi_{\gamma\gamma}^{n,A_{1g}}(\omega)\right) = 2\pi N_{F,n}\left(\gamma_{A_{1g}}^n\right)^2 \times \frac{2}{\pi} P \int_{2\Delta_n}^{\infty} \frac{\Delta_n^2}{(\omega'^2 - \omega^2)\sqrt{\omega'^2 - 4\Delta_n^2}} d\omega' \tag{5.27}$$

The lower integration boundary here is $2\Delta_n$ since for smaller values of ω' the square root would get imaginary but the result is meant to be the real part of $\chi_{\gamma\gamma}^{n,A_{1g}}(\omega)$ so the imaginary case has to be excluded. The evaluation of the integral for $\Delta_n > 0$ leads to

$$Re\left(\chi_{\gamma\gamma}^{n,A_{1g}}(\omega)\right) = 2\pi N_{F,n}\left(\gamma_{A_{1g}}^n\right)^2 \times Re\left[\frac{2}{\pi}\frac{\Delta_n^2}{\omega\sqrt{4\Delta_n^2 - \omega^2}}\arcsin\left(\frac{\omega}{2\Delta_n}\right)\right] \tag{5.28}$$

The function in the argument of the Re is entirely real below $\omega = 2\Delta_n$ since the square
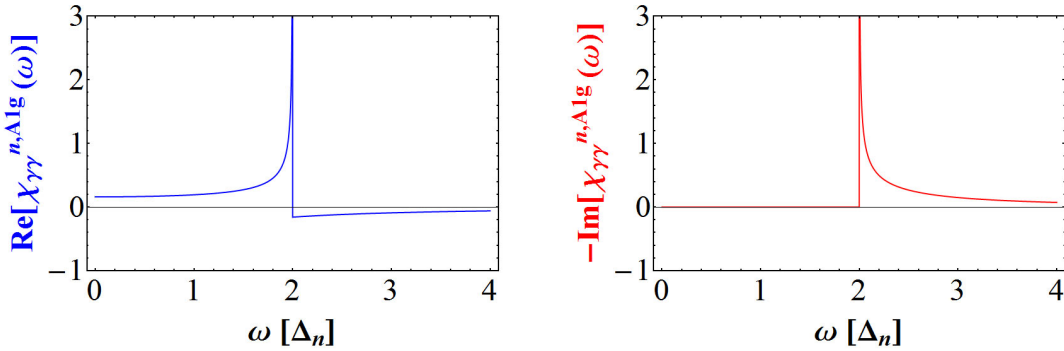
Figure 5.2: Real part (blue) and imaginary part multiplied with minus unity (red) of the response function in A_{1g} symmetry as a function of ω in units of Δ_n. The effective masses used correspond to one electron mass. The singularity occurs at $\omega = 2\Delta_n$ in both plots and the real part has a sign change at this point.

root is real and the imaginary part of the arcsin is zero. At $\omega = 2\Delta_n$ it has a singularity in the real as well as in the imaginary part and a sign change in the real part. Above $\omega = 2\Delta_n$

the function has both an imaginary and a real part. The latter one consists of the square root with the signs switched in the argument multiplied with the imaginary part of the arcsin. The imaginary part shows an interesting feature. With the real part of the arcsin being a constant of $\frac{\pi}{2}$ that cancels with the factor of $\frac{2}{\pi}$ and the switched signs under the square root the previously obtained result for $Im\left(\chi_{\gamma\gamma}^{n,A_{1g}}\right)$ is reproduced with a minus sign in front that appears by moving the i coming from the square root from the denominator into the numerator. Thus the function

$$\chi_{\gamma\gamma}^{n,A_{1g}}(\omega) = 2\pi N_{F,n}\left(\gamma_{A_{1g}}^n\right)^2 \times \frac{2}{\pi}\frac{\Delta_n^2}{\omega\sqrt{4\Delta_n^2 - \omega^2}}\arcsin\left(\frac{\omega}{2\Delta_n}\right) \tag{5.29}$$

is the total response function with the proper real part and the imaginary part with a switched sign. This minus will be absorbed in the definition of the Raman response. The real and the imaginary part multiplied with minus unity of $\chi_{\gamma\gamma}^{n,A_{1g}}$ are shown in Fig. 5.2 for effective masses corresponding to one electron mass and and ω in the units of Δ_n. For the following discussion $\chi_{\gamma\gamma}^{n,A_{1g}}(\omega)$ will be transformed into a slightly simpler form with the definition of $x_n = \frac{\omega}{2\Delta_n}$. This results in

$$\chi_{\gamma\gamma}^{n,A_{1g}}(\omega) = N_{F,n}\left(\gamma_{A_{1g}}^n\right)^2 \frac{\arcsin(x_n)}{x_n\sqrt{1 - x_n^2}} \tag{5.30}$$

Interplay of two screened bands in A_{1g} symmetry

With the entire response function for the used model known it is now possible to investigate the effect of screening, which is only present in A_{1g} symmetry, for one and two bands. The latter one is the much more interesting case since for only one band the screening is perfect in the applied approximations. This can be easily seen in the general expression for the screened Raman response for the nth band which is

$$Im\left[N_{Fn}\gamma_n^2 F_n\right] - Im\left[\frac{(N_{Fn}\gamma_n F_n)^2}{N_{Fn}F_n}\right] \tag{5.31}$$

with the definition

$$F_n = \frac{\arcsin(x_n)}{x_n\sqrt{1 - x_n^2}} \tag{5.32}$$

and dropping the index of the symmetry channel of the vertex for a more condensed notation. It clearly shows that the screening term exactly cancels the unscreened term. This is the

case for parabolic as well as elliptical shaped Fermi surface sheets and has its origin in the fact that for both the Raman verteces are constants. Furthermore the density of states in two dimensions is also a constant, meaning it is independent of energy and solely determined by the effective masses of the band and the area of the unit cell. The general form of the screened Raman response for two bands which is

$$Im \left[N_{F1}\gamma_1^2 F_1 + N_{F2}\gamma_2^2 F_2 \right] - Im \left[\frac{(N_{F1}\gamma_1 F_1 + N_{F2}\gamma_2 F_2)^2}{N_{F1}F_1 + N_{F2}F_2} \right] \tag{5.33}$$

leaves a lot more room for variation of the different parameters and shows a wide range of different possible cases. The alterable parameters are the effective masses m_{n1}^* and m_{n2}^* (n is the band index and 1 and 2 correspond to the $k_x + k_y$ and the $k_x - k_y$ direction) that can be adjusted to a parabolic band and an elliptical band with variable ellipticity. Furthermore the absolute value as well as the sign of the effective mass represent a huge play ground themselves. Also the gap parameter can be altered and hence F_n in Eq. (5.32).

At this point all parts of the two bands will be taken to be different which makes the further discussion remain general. Expanding out the bracket in the numerator of the screening term and multiplying a nontrivial form of unity to the terms containing $N_{Fn}^2 \gamma_n^2 F_n^2$ results in

$$\begin{aligned} Im \Big[\ N_{F1}\gamma_1^2 F_1 + N_{F2}\gamma_2^2 F_2 \Big] &- Im \left[\frac{N_{F1}^2 \gamma_1^2 F_1^2}{N_{F1}F_1 + N_{F2}F_2} \left(\frac{N_{F1}F_1 + N_{F2}F_2}{N_{F1}F_1} - \frac{N_{F2}F_2}{N_{F1}F_1} \right) \right. \\ &+ \left. \frac{N_{F2}^2 \gamma_2^2 F_2^2}{N_{F1}F_1 + N_{F2}F_2} \left(\frac{N_{F1}F_1 + N_{F2}F_2}{N_{F2}F_2} - \frac{N_{F1}F_1}{N_{F2}F_2} \right) + \frac{2N_{F1}N_{F2}\gamma_1\gamma_2 F_1 F_2}{N_{F1}F_1 + N_{F2}F_2} \right] \end{aligned} \tag{5.34}$$

The first fraction of the nontrivial unity bracket gives together with the term in front of the bracket for both brackets a term that cancels exactly with one in the unscreened response. The remaining fractions of the screening term can be brought to the simpler form

$$Im \left[(\gamma_1 - \gamma_2)^2 \, \frac{N_{F1}F_1 N_{F2}F_2}{N_{F1}F_1 + N_{F2}F_2} \right] \tag{5.35}$$

This represents the entire Raman response and can be seen as a cross term of the two bands since the response of the two single bands and their screening were separated and canceled by each other. It is now very easy to see that the entire response is vanishing and therefore the screening is perfect if the γ's are equal. This is the case when $m_1^* = m_2^*$ for the parabolic band and $m_{11}^* = m_{21}^*$ and $m_{12}^* = m_{22}^*$ or $m_{11}^* = m_{22}^*$ and $m_{12}^* = m_{21}^*$ for the elliptic band
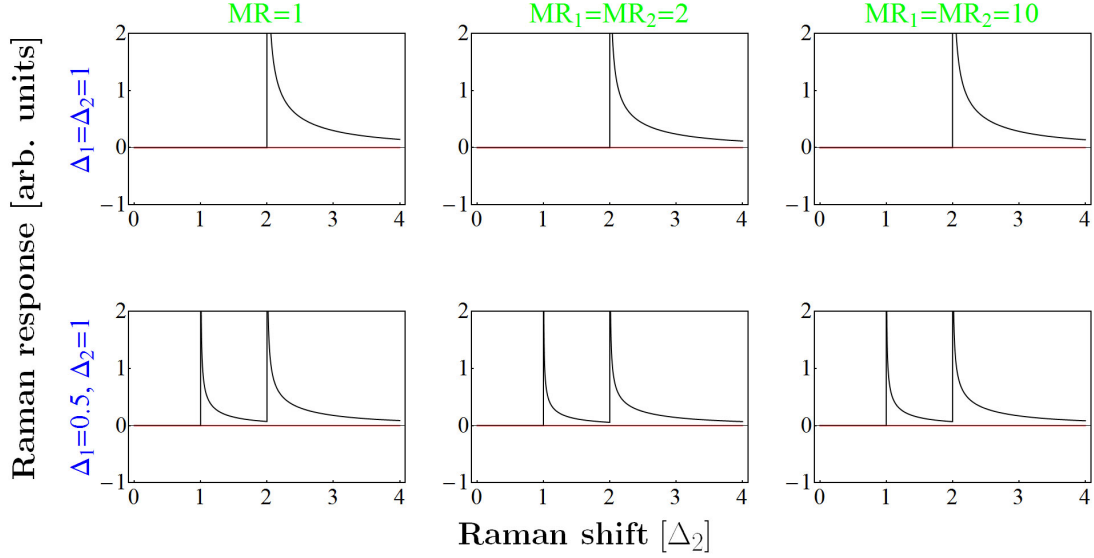
Figure 5.3: Comparison of unscreened (black) and screened Raman response (red) of two electron-like bands with identical Raman verteces in A_{1g} symmetry. For parabolic bands with a mass ratio (MR) of 1 and elliptical bands of MR's 2 and 10 the screening is perfect and the screened response vanishes. This is true for equal and different gap parameters Δ_n.

and is shown in Fig. 5.3. The displayed plots further demonstrate that the gap values have no influence at all on this behavior and that for different Δ_n's the screened response also vanishes as expected from Eq. 5.35.

Another easily recognizable fact of Eq. (5.35) is that for γ's with opposite signs, refering to one electron and one hole band, the response will reach a maximum. The question arises at this point if that corresponds to a vanishing screening or some intermediate case of partial screening. A closer look at the general screening term, the second term in Eq. (5.33), shows that the screening certainly vanishes for the same gap value and the same absolute value of the effective masses but different signs for the different bands (different signs within one band make no physical sense). As soon as one of those parameters differs in between the two bands the situation becomes nontrivial and requires more detailed investigation. First the gap parameter will be set equal in both F's which are then equal to each other and can be put out of the bracket in the numerator of the screening term. Hence this term will be

$$Im \left[\frac{(N_{F1}\gamma_1 + N_{F2}\gamma_2)^2}{N_{F1} + N_{F2}} F \right] \tag{5.36}$$
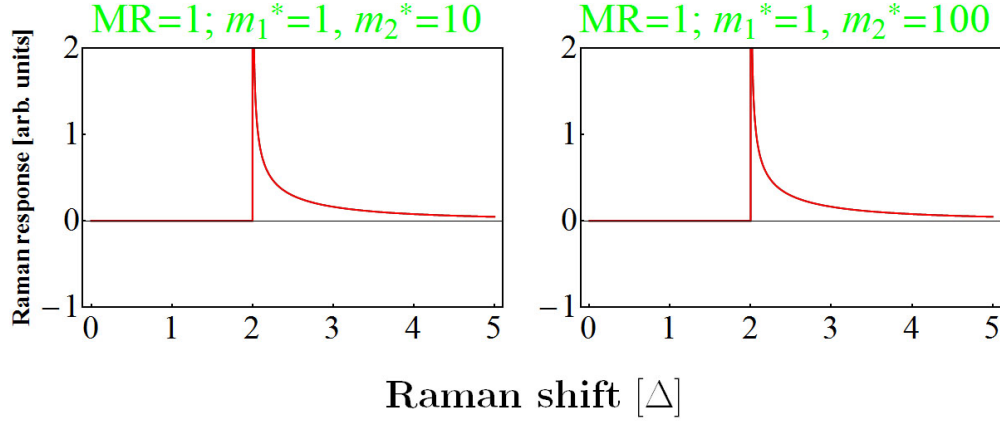
Figure 5.4: Comparison of unscreened (black) and screened (red) Raman responses for two parabolic bands of opposite signs with equal gap values and different absolute values of the effective masses in A_{1g} symmetry. The given numbers correspond to the number of electron masses. The screening vanishes for all mass differences.

The fraction in front of F is a function of the effective masses which is written out explicitly as

$$\frac{1}{M^*} = B \frac{\left(\sqrt{m_{11}^* m_{12}^*} \left(\frac{1}{m_{11}^*} + \frac{1}{m_{12}^*} \right) + \sqrt{m_{21}^* m_{22}^*} \left(\frac{1}{m_{21}^*} + \frac{1}{m_{22}^*} \right) \right)^2}{\sqrt{m_{11}^* m_{12}^*} + \sqrt{m_{21}^* m_{22}^*}} \tag{5.37}$$

with all common constants absorbed in B. This can be brought to a more transparent form by taking one of the inverse effective masses out of the bracket. It is important to note that in this case, where the interplay of an electron-like and a hole-like band is investigated, the masses of one band are negative quantities. Without loss of generality the masses of band 2 will be taken to be hole-like and thus negative meaning $m_{21}^* = -|m_{21}^*|$ and $m_{22}^* = -|m_{22}^*|$. This turns the sign in between the terms in the numerator to a minus and Eq. (5.37) transforms into

$$\frac{1}{M^*} = B \frac{\left(\sqrt{\frac{m_{12}^*}{m_{11}^*}} \left(1 + \frac{m_{11}^*}{m_{12}^*} \right) - \sqrt{\frac{m_{22}^*}{m_{21}^*}} \left(1 + \frac{m_{21}^*}{m_{22}^*} \right) \right)^2}{\sqrt{m_{11}^* m_{12}^*} + \sqrt{m_{21}^* m_{22}^*}} \tag{5.38}$$

The absolute value brackets are thrown away here since $\frac{1}{M^*}$ is a function of the mass ratios $MR_n = \frac{m_{n2}^*}{m_{n1}^*}$ of the bands which are always positive. In the parabolic case all these mass ratios (MR's) are unity and there are two constants left in the numerator that cancel each other. Hence the whole term and thus the screening vanishes. It is a remarkable result that the absolute value of the masses has no influence if both bands are parabolic. This means

that different parabolic bands with dramatically different effective masses with opposite signs are entirely unscreened as long as they have the same gap value. Fig. 5.4 displays the corresponding Raman responses for a mass difference of a factor of 10 and 100. In both cases the unscreened (black) and screened (red) responses are exactly the same and thus there is no screening. Furthermore the screening term also vanishes if the MR's of the two bands are equal. That means that for elliptical bands of the same ellipticity it also does not matter what absolute value the masses have. As long as the band masses have opposite signs and the gap value is the same for both they are totally unscreened. This corresponds to the plots on the diagonal of Fig. 5.5. Here the screened Raman response looks entirely

Figure 5.5: Comparison of the unscreened (black) and screened (red) Raman responses in A_{1g} symmetry of two elliptical bands with opposite signs and equal gap values for different combinations of mass ratios (MR_n) for the nth band. The diagonal shows no difference between unscreened and screened response since the MR's are equal. A real difference between the screened and the unscreened response is first seen with a difference of a factor of 10 between the MR's. The response below $\omega = 1\Delta$ is not shown since it is zero.

equal to the unscreened one. The independence of the masses absolute value is restricted

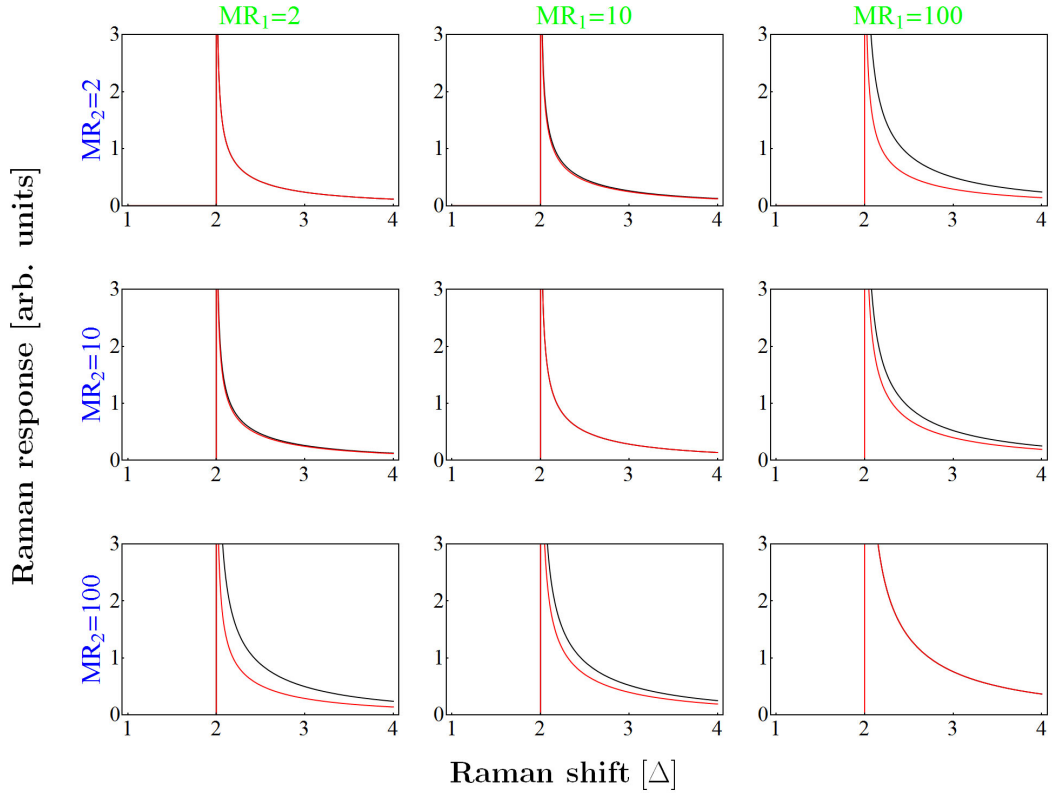to the two dimensional case. In 1D as well as in 3D the density of states is not a constant
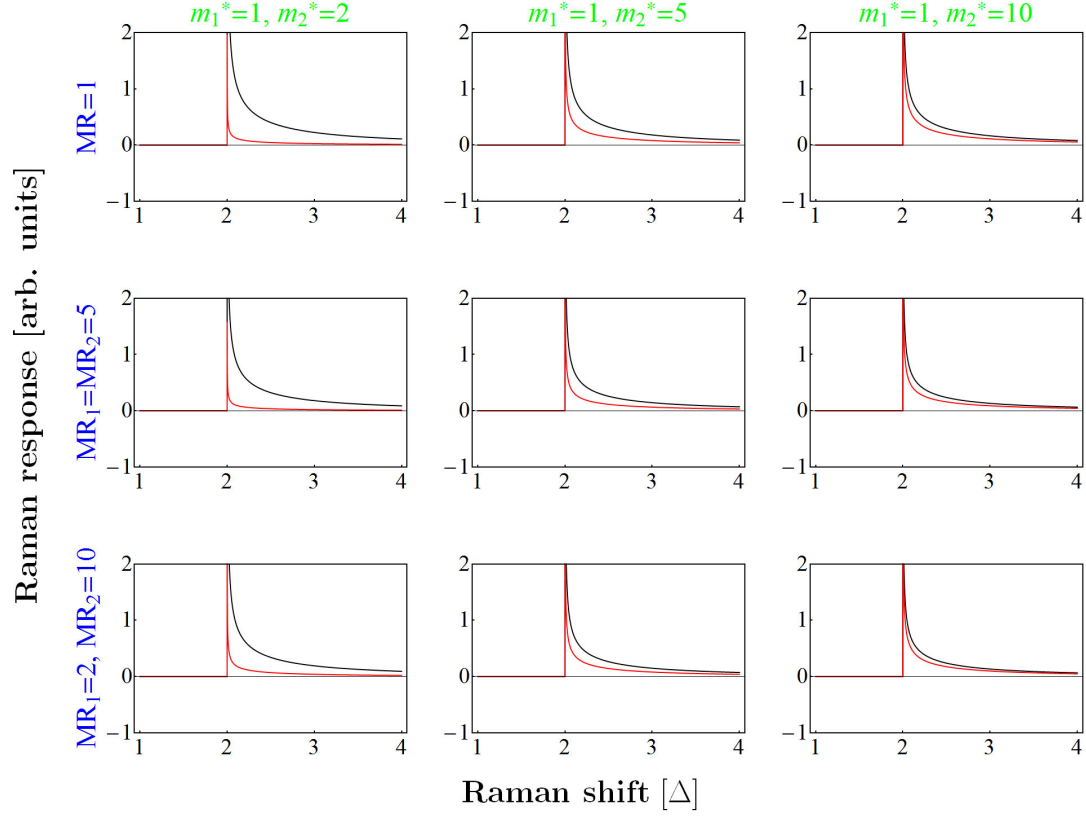

Figure 5.6: Comparison of unscreened (black) and screened (red) Raman responses in A_{1g} symmetry for two bands with the same sign, same gap value and different combinations of effecitve masses m_1^* and m_2^* for band 1 and 2 respectively. The given numbers correspond to the number of electron masses and the second effective mass of the band in the elliptical case is given by the mass ratio (MR). The first row shows two parabolic bands, the second row two elliptical bands with equal ellipticity and the third row displays two elliptical bands with different ellipticities. The screening is never perfect and gets less effective for bigger differences between the effective masses.

any more and shows an energy dependence. Furthermore the term in the density of states that includes the effective mass of the band has not the dimension of mass to the power of one in both cases. Thus it is simply by dimensional analysis impossible that the effective mass dependence of the density of states cancels with the effective mass dependence in the Raman vertex.

The next interesting scenario that can be studied in more detail is the change of ellipticity in between the two bands of opposite signs. The gap is still assumed to be the same for both bands thus Eq. (5.38) will still apply. With a different mass ratio (MR) the terms

in the numerator do not cancel anymore and the screening will affect the Raman response. The effects of different MR's are displayed in Fig. 5.5. The diagonal still has the same MR for the two bands and thus shows no difference in between the unscreened (black) and screened response (red). The invariance towards band switching of Eq. (5.38) results in the plot array being a symmetric matrix. The deviation from the unscreened term in the offdiagonal plots is first obviously seen for a difference of the MR's by a factor of 10. For a difference by a factor of 5 there is almost no recognizable deviation and for a factor of 100 between the MR's the deviation becomes more noticeable.

Another case of intermediate screening will be observed if two bands of the same sign but with different absolute values of the effective masses are considered. This makes the Raman verteces of the two bands having the same sign but a different absolute value and the bracket in Eq. (5.35) not vanishing nor maximal. To study the simplest case of this scenario first the gap value will be taken to be equal for the two bands which transforms Eq. (5.35) to the following form.

$$Im\left[(\gamma_1 - \gamma_2)^2 \frac{N_{F1}N_{F2}}{N_{F1} + N_{F2}} F\right] \tag{5.39}$$

This time the total response is determined by the difference of the verteces and the fraction of the densities of state. Unscreened (black) and screened (red) Raman responses for different combinations of effective masses for parabolic and elliptical bands of the same as well as different ellipticities are shown in Fig. 5.6. For small differences between the effective masses the verteces in Eq. (5.39) almost cancel each other and the screened response is small. The bigger the difference of m_1^* and m_2^* gets the bigger is the total response.

So far all investigations were tied to the simplification of equal gap values in both bands, except for the trivial case of equal verteces and therefore vanishing response. Now this assumption will be dropped and the case of different gap values will be discussed which makes the F_n's different for the two bands. Without loss of generality $\Delta_1 < \Delta_2$ is assumed in the following. In order to gain more insight in the exact nature of Eq. (5.35) the simplifying definitions in Eq. (5.32) will be partially reinserted. This leads to

$$Im\left[(\gamma_1 - \gamma_2)^2 \frac{N_{F1}N_{F2}\frac{AS(1)}{x_1\sqrt{1-x_1^2}}\frac{AS(2)}{x_2\sqrt{1-x_2^2}}}{N_{F1}\frac{AS(1)}{x_1\sqrt{1-x_1^2}} + N_{F2}\frac{AS(2)}{x_2\sqrt{1-x_2^2}}}\right] \tag{5.40}$$
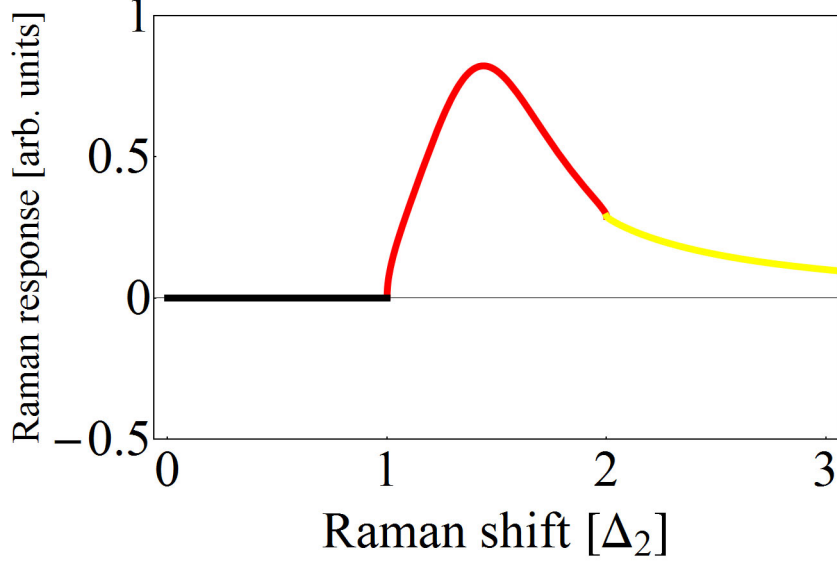
Figure 5.7: Illustration of the Raman response of two parabolic bands with different gap values of $2\Delta_1 = \Delta_2$, different signs and equal absolute values of the effective masses m_1^* and m_2^*. The region of $\omega < 2\Delta_1 < 2\Delta_2$ is displayed in black, the region of $2\Delta_1 < \omega < 2\Delta_2$ in red and the region of $2\Delta_1 < 2\Delta_2 < \omega$ in yellow. There are no singularities at twice the gap values.

with the new short representation of the arcsin

$$AS(n) = \arcsin(x_n) \tag{5.41}$$

Eq. (5.40) immediately simplifies to

$$Im\left[(\gamma_1 - \gamma_2)^2 \frac{N_{F1}N_{F2}AS(1)AS(2)}{N_{F1}AS(1)x_2\sqrt{1-x_2^2} + N_{F2}AS(2)x_1\sqrt{1-x_1^2}}\right] \tag{5.42}$$

This equation shows another remarkable fact that was not obvious in the general form. At $\omega = 2\Delta_1$, where $x_1 = 1$ and $x_2 = \frac{\Delta_1}{\Delta_2}$, the square root in the second term in the denominator vanishes and so does the whole term while the square root in the first term in the denomiator stays real and finite. $AS(1)$ cancels because it is present in the numerator as well and $AS(2)$ is an entirely real function since its imaginary part is zero for the argument being smaller than 1. Thus Eq. (5.42) takes the following value at $\omega = 2\Delta_1$ and hence $x_1 = 1$ and $x_2 = \frac{\Delta_1}{\Delta_2}$

$$Im\left[(\gamma_1 - \gamma_2)^2 N_{F2} \frac{\arcsin\left(\frac{\Delta_1}{\Delta_2}\right)}{\frac{\Delta_1}{\Delta_2}\sqrt{1 - \frac{\Delta_1^2}{\Delta_2^2}}}\right] = 0 \tag{5.43}$$
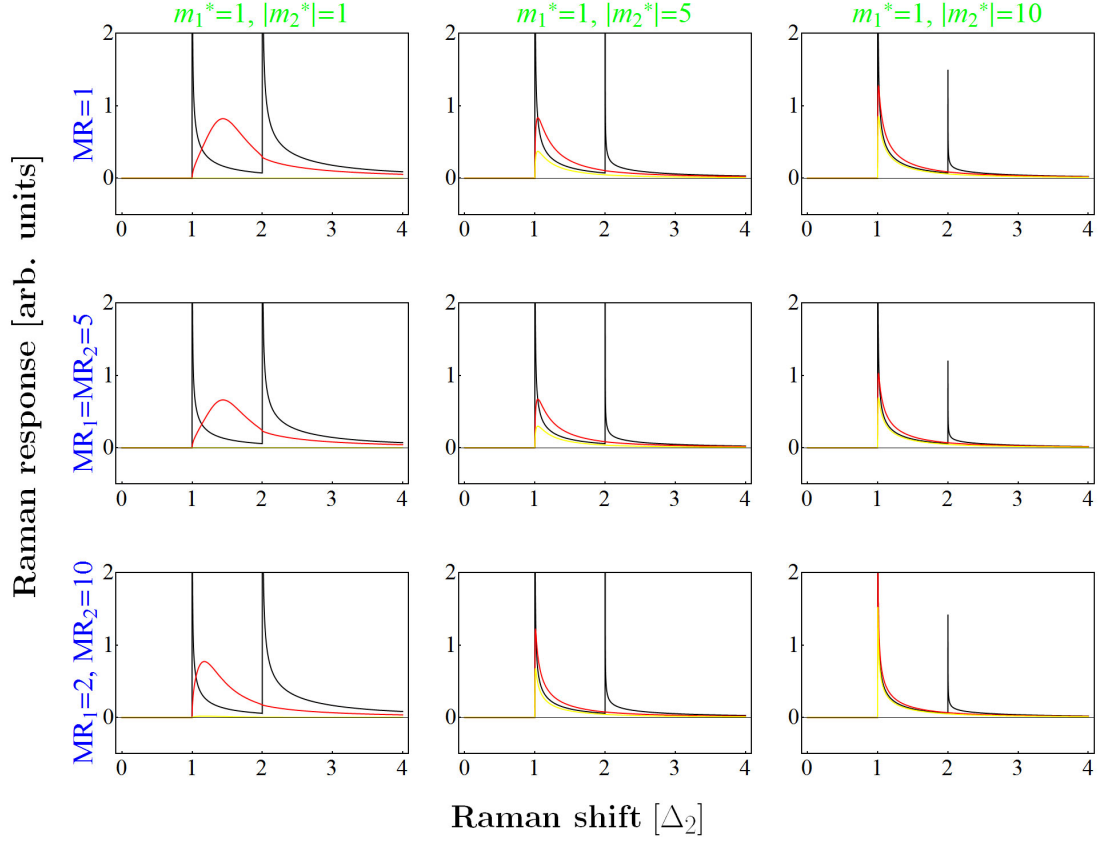
Figure 5.8: Comparison of unscreened (black) and screened Raman responses in A_{1g} symmetry for two bands with different gap values $2\Delta_1 = \Delta_2$ and different combinations of effective masses. The yellow plots correspond to two screened electron-electron bands and the red plots to two screened electron-hole bands. The given numbers for the effective masses correspond to the number of electron masses. It is the sign of m_2^* that is altered and the values of the second band mass in the elliptical case are given through the mass ratio (MR_n). For the verteces being of the same sign and value (two upper yellow plots in the first column) the response is again vanishing. This is not the case for the lowest yellow plot in the first column which is only vanishingly small but not exactly zero. The larger the masses get the sharper gets the peak and the closer it is located to the the position of the singularity of the band with the smaller masses. The peaks moved from the middle exhibit a more similar shape to the square root singularity the sharper they get. The electron-electron band response (yellow) is always smaller than the electron-hole response (red).

This means that the first singularity, meaning the one at twice the smaller gap value, is removed and the whole response vanishes at this point. At $\omega = 2\Delta_2$ and thus $x_1 = \frac{\Delta_2}{\Delta_1}$ and $x_2 = 1$ the first term in the denominator vanishes and the square root in the second term gets imaginary. This time $AS(2)$ cancels out and the argument of $AS(1)$ is bigger than unity making it imaginary with a real part being a constant of $\frac{\pi}{2}$. Hence at $\omega = 2\Delta_2$ Eq. (5.42) is

$$Im\left[(\gamma_1 - \gamma_2)^2 \, N_{F1} \frac{\frac{\pi}{2} + iIm\left[\arcsin\left(\frac{\Delta_2}{\Delta_1}\right)\right]}{i\frac{\Delta_2}{\Delta_1}\sqrt{\frac{\Delta_2^2}{\Delta_1^2} - 1}}\right] = -\frac{\pi \, (\gamma_1 - \gamma_2)^2 \, N_{F1}\Delta_1^2}{2\Delta_2\sqrt{\Delta_2^2 - \Delta_1^2}} \tag{5.44}$$

So the singularity at twice the bigger gap value is also removed but remains finite. The removal of the singularities will no longer be present if the gap values Δ_1 and Δ_2 are taken to be equal again since then the two terms in the denominator of Eq. (5.42) vanish at the same point and the whole term approaches infinity. Hence this case properly reduces to the simpler case of similar gap values discussed earlier. After realizing the removal of the singularities the behavior of the response in the three regions $\omega < 2\Delta_1 < 2\Delta_2$, $2\Delta_1 < \omega < 2\Delta_2$ and $2\Delta_1 < 2\Delta_2 < \omega$ will be studied. In the first region the arguments of both arcsin's are smaller than one and both square roots are real which makes the whole argument of $Im[...]$ in Eq. (5.42) real and thus the function equal to zero. So the entire response below twice the smaller gap value vanishes. In the region where $2\Delta_1 < \omega < 2\Delta_2$, corresponding to $x_1 > 1$ and $x_2 < 1$, $AS(1)$ becomes a function with a real as well as an imaginary part and the square root including x_1 is entirely imaginary while $AS(2)$ and the square root containing x_2 stay real. After separating the real from the imaginary parts one obtains

$$-\frac{(\gamma_1 - \gamma_2)^2 \, N_{F1}N_{F2}^2 \, (Re\,[AS(2)])^2 \, SQ_1}{\frac{2}{\pi}\left[\left(\frac{\pi}{2}N_{F1}\widetilde{SQ_2}\right)^2 + \left(N_{F1}Im\,[AS(1)]\,\widetilde{SQ_2} + N_{F2}Re\,[AS(2)]\,SQ_1\right)^2\right]} \tag{5.45}$$

with the following definitions for a shorter notation

$$\widetilde{SQ}_n = x_n\sqrt{1 - x_n^2}$$
$$SQ_n = x_n\sqrt{x_n^2 - 1} \tag{5.46}$$

In the region where $2\Delta_1 < 2\Delta_2 < \omega$, meaning $x_1 > 1$ and $x_2 > 1$, both arcsin's have a real and an imaginary part and both square roots are imaginary. The separation of the real and the imaginary part leads to

$$-\frac{(\gamma_1 - \gamma_2)^2 N_{F1}N_{F2}\left[N_{F2}\left((2Im\left[AS(2)\right])^2 + \pi^2\right)SQ_1 + N_{F1}\left((2Im\left[AS(1)\right])^2 + \pi^2\right)SQ_2\right]}{\frac{8}{\pi}\left[(N_{F1}Im\left[AS(1)\right]SQ_2 + N_{F2}Im\left[AS(2)\right]SQ_1)^2 + \left(\frac{\pi}{2}N_{F1}SQ_2 + \frac{\pi}{2}N_{F2}SQ_1\right)^2\right]}$$
(5.47)

A plot of the three different regions with $\omega < 2\Delta_1 < 2\Delta_2$ ($x_1 < 1$ and $x_2 < 1$) in black, $2\Delta_1 < \omega < 2\Delta_2$ ($x_1 > 1$ and $x_2 < 1$) in red and $2\Delta_1 < 2\Delta_2 < \omega$ ($x_1 > 1$ and $x_2 > 1$) in yellow is shown in Fig. 5.7. As expected from the preceding argumentation there are
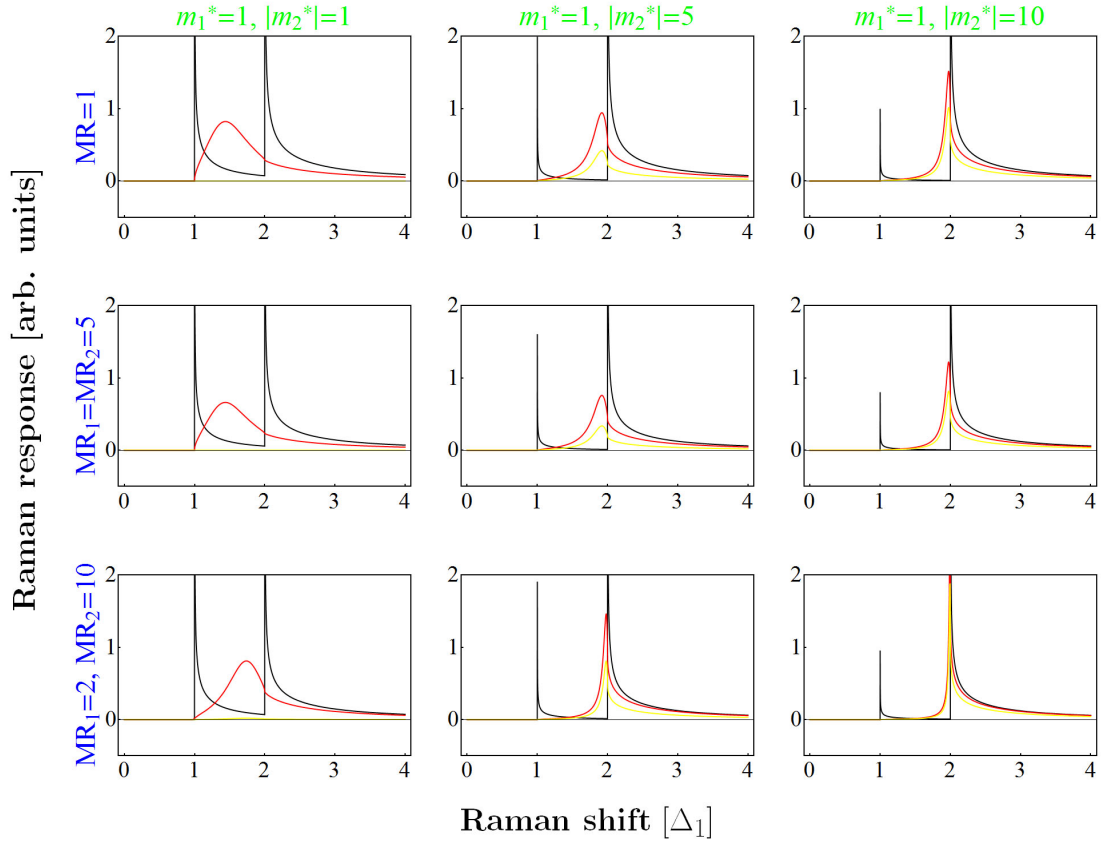
Figure 5.9: Same plots as in Fig. 5.8 but with $\Delta_1 = 2\Delta_2$. For the peaks of the screened responses located in the middle of the singularities there is no change but all the other peaks now move towards the singularity of the bigger gap value since this is now the one of the band with the smaller masses. The overall shape of the peaks that are moved from the middle is now less square root singularity like but looks more like a sharper getting bell.

no singularities at twice the gap values and the function is zero at twice the smaller and finite at twice the bigger gap value. In between those two removed singularities is a bell

shaped peak located in the middle and above twice the larger gap value the function falls off. Fig. 5.8 shows the unscreened (black) and screened Raman responses for two bands with the same sign (yellow) and with different signs (red). The different combinations of effective masses influence the peak position as well as its shape. The larger the masses get the sharper gets the peak and it approaches more and more the form of a square root singularity. Furthermore the peak moves towards twice the smaller gap value which corresponds to the band with the smaller effective masses. If both verteces are equal the peak is located in the middle of the two singularities for the electron-hole case (red) and the entire response vanishes for the electron-electron case (yellow) since the verteces are exactly equal. It is important to note that the lowest plot in the first column does not have a vanishing electron-electron band response but a very small one which is rooted in the small difference of the verteces. In Fig. 5.9 the same case as in Fig. 5.8 except for now $\Delta_1 = 2\Delta_2$ is displayed. The obvious difference here is that the peak moves towards the larger gap value now which is again the one corresponding to the band with the smaller effective masses. The shape also changes in the cases of the peak being moved from the middle. Now the response exhibits a more bell like shape that gets sharper and sharper for increasing effective masses. In both cases the response with the two bands having opposite signs (red) is always larger than the one with equal signs of the effective masses since the verteces add up in the former case instead of subtracting from each other in the latter one.

Interplay of multiple screened bands

After having studied the interplay of two bands in all kinds of different cases it is certainly interesting to generalize the investigations to more than two and finally n bands. First the Raman response for three bands is considered which has the form

$$
\begin{aligned}
&Im\left[N_{F1}\gamma_1^2 F_1 + N_{F2}\gamma_2^2 F_2 + N_{F3}\gamma_3^2 F_3\right] \\
&-Im\left[\frac{(N_{F1}\gamma_1 F_1 + N_{F2}\gamma_2 F_2 + N_{F3}\gamma_3 F_3)^2}{N_{F1}F_1 + N_{F2}F_2 + N_{F3}F_3}\right]
\end{aligned}
\tag{5.48}
$$

With an entirely similar calculation as in the two band case this can be transformed to

$$Im\left[\frac{N_{F1}F_1 N_{F2}F_2}{N_{F1}F_1 + N_{F2}F_2 + N_{F3}F_3}(\gamma_1 - \gamma_2)^2\right.$$
$$+\frac{N_{F1}F_1 N_{F3}F_3}{N_{F1}F_1 + N_{F2}F_2 + N_{F3}F_3}(\gamma_1 - \gamma_3)^2$$
$$\left.+\frac{N_{F2}F_2 N_{F3}F_3}{N_{F1}F_1 + N_{F2}F_2 + N_{F3}F_3}(\gamma_2 - \gamma_3)^2\right] \tag{5.49}$$

For four bands the calculations are again analog and the Raman response

$$Im\left[N_{F1}\gamma_1^2 F_1 + N_{F2}\gamma_2^2 F_2 + N_{F3}\gamma_3^2 F_3 + N_{F4}\gamma_4^2 F_4\right]$$
$$-Im\left[\frac{(N_{F1}\gamma_1 F_1 + N_{F2}\gamma_2 F_2 + N_{F3}\gamma_3 F_3 + N_{F4}\gamma_4 F_4)^2}{N_{F1}F_1 + N_{F2}F_2 + N_{F3}F_3 + N_{F4}F_4}\right] \tag{5.50}$$

is brought to the more transparent form

$$Im\left[\frac{N_{F1}F_1 N_{F2}F_2}{N_{F1}F_1 + N_{F2}F_2 + N_{F3}F_3 + N_{F4}F_4}(\gamma_1 - \gamma_2)^2\right.$$
$$+\frac{N_{F1}F_1 N_{F3}F_3}{N_{F1}F_1 + N_{F2}F_2 + N_{F3}F_3 + N_{F4}F_4}(\gamma_1 - \gamma_3)^2$$
$$+\frac{N_{F1}F_1 N_{F4}F_4}{N_{F1}F_1 + N_{F2}F_2 + N_{F3}F_3 + N_{F4}F_4}(\gamma_1 - \gamma_4)^2$$
$$+\frac{N_{F2}F_2 N_{F3}F_3}{N_{F1}F_1 + N_{F2}F_2 + N_{F3}F_3 + N_{F4}F_4}(\gamma_2 - \gamma_3)^2$$
$$+\frac{N_{F2}F_2 N_{F4}F_4}{N_{F1}F_1 + N_{F2}F_2 + N_{F3}F_3 + N_{F4}F_4}(\gamma_2 - \gamma_4)^2$$
$$\left.+\frac{N_{F3}F_3 N_{F4}F_4}{N_{F1}F_1 + N_{F2}F_2 + N_{F3}F_3 + N_{F4}F_4}(\gamma_3 - \gamma_4)^2\right] \tag{5.51}$$

Taking a closer look at Eq. (5.49) and Eq. (5.51) makes it easy to find the general form for the interplay of n bands which can be written as

$$Im\left[\sum_{i,j}(\gamma_i - \gamma_j)^2 \frac{N_{Fi}F_i N_{Fj}F_j}{(\sum_l N_{Fl}F_l)}\right] \tag{5.52}$$

with all i, j, l running from 1 to n. The case of $i = j$ does not have to be excluded since the bracket containing the verteces is equal to zero for that case and automatically cancels the whole term. This form shows that for any verteces γ_i and γ_j being equal to each other the corresponding term containing the functions F_i and F_j vanishes. Furthermore with the numerator of each term only containing two functions F_i and F_j and the corresponding densities of state N_{Fi} and N_{Fj} most of the results obtained in the two band case are still true for each single term in the sum of Eq. (5.52). The single term of two bands having opposite

signs will still be unscreened if the bands are parabolic or have the same ellipticity and the two gap values are equal. For two bands with opposite signs and different ellipticities and for two bands with equal signs and different verteces the screening will still be partial if the gap parameters are equal. The removal of the singularities in the case of different gap values for each single term will now be more complicated since there are now n gap parameters and n terms in the denominator that have to vanish at the same time in order to produce a singularity. For reasons of simplification and since this is assumed in the applied model for the pnictide band structure the case of $n = 4$ bands will now be studied in detail to clarify the conditions for the removal and the presence of a singularity. Expanding Eq. (5.40) to the four band case results in the single term for the bands i and j

$$Im\left[(\gamma_i - \gamma_j)^2 \frac{\frac{K_i}{\widetilde{SQ}_i}\frac{K_j}{\widetilde{SQ}_j}}{\frac{K_1}{\widetilde{SQ}_1} + \frac{K_2}{\widetilde{SQ}_2} + \frac{K_3}{\widetilde{SQ}_3} + \frac{K_4}{\widetilde{SQ}_4}}\right] \tag{5.53}$$

with further simplifying definitions

$$K_n = N_{Fn}AS(n)$$
$$\widetilde{SQ}_n = x_n\sqrt{1 - x_n^2} \tag{5.54}$$

(The second one is previously defined in Eq. (5.46) but repeated for the readers convenience.) This can be transformed into the following form

$$Im\left[(\gamma_i - \gamma_j)^2 \frac{K_iK_j}{K_1\frac{\widetilde{SQ}_i\widetilde{SQ}_j}{\widetilde{SQ}_1} + K_2\frac{\widetilde{SQ}_i\widetilde{SQ}_j}{\widetilde{SQ}_2} + K_3\frac{\widetilde{SQ}_i\widetilde{SQ}_j}{\widetilde{SQ}_3} + K_4\frac{\widetilde{SQ}_i\widetilde{SQ}_j}{\widetilde{SQ}_4}}\right] \tag{5.55}$$

Here it is very important which $\widetilde{SQ}$'s have the same or different gap values and can be canceled with each other in the terms in the denominator. The symmetry of this expression allows to set i and j equal to any number of the four bands thus they will be set to $i = 1$ and $j = 2$ for a more transparent discussion of the possible cases. First all four gap parameters will be taken to differ from each other resulting in $\widetilde{SQ}_1 \neq \widetilde{SQ}_2 \neq \widetilde{SQ}_3 \neq \widetilde{SQ}_4$. Eq. (5.55) then will be

$$Im\left[(\gamma_1 - \gamma_2)^2 \frac{K_1K_2}{K_1\widetilde{SQ}_2 + K_2\widetilde{SQ}_1 + K_3\frac{\widetilde{SQ}_1\widetilde{SQ}_2}{\widetilde{SQ}_3} + K_4\frac{\widetilde{SQ}_1\widetilde{SQ}_2}{\widetilde{SQ}_4}}\right] \tag{5.56}$$
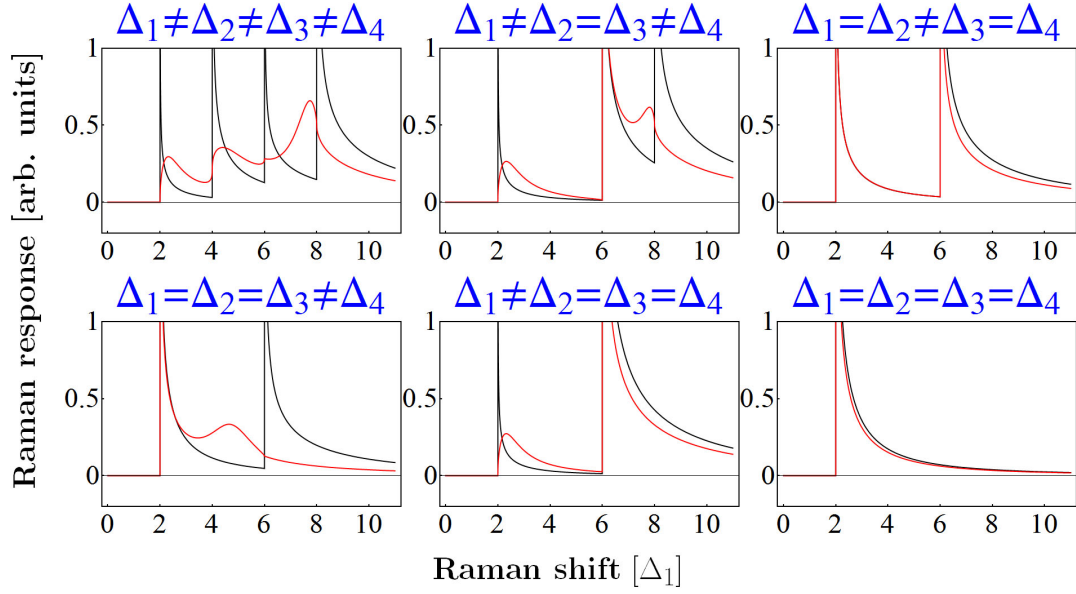
Figure 5.10: Comparison of unscreened (black) and screened (red) Raman response for four bands of unequal Raman verteces and different combinations of gap values in A_{1g} symmetry. For all gaps being different all singularities are removed and in between twice the gap values there are the bell shaped peaks discussed in the two band case. Whenever a gap value appears in more than one band the singularity at twice this gap value is not removed.

When $\widetilde{SQ}_1$ hits zero the second term in the denominator vanishes as well as the third and the fourth term but the first term still remains finite and there is no singularity. When $\widetilde{SQ}_2$ vanishes it is the second term in the denominator that is still finite also resulting in a removal of this singularity. If $\widetilde{SQ}_3$ is zero the third term in the denominator approaches infinity and the same thing happens with the fourth term when $\widetilde{SQ}_4$ vanishes. Hence the whole fraction vanishes for those two cases and all possible singularities are removed. This is true for all terms of the sum over i, j since they are symmetric in exchanging the four band numbers. Now the assumption of only three gap parameters being different will be made and first I choose $\widetilde{SQ}_1 \neq \widetilde{SQ}_2 \neq \widetilde{SQ}_3 = \widetilde{SQ}_4$. This leads to the following form of the single term in the sum of the total response

$$Im\left[(\gamma_1 - \gamma_2)^2 \frac{K_1 K_2}{K_1 \widetilde{SQ}_2 + K_2 \widetilde{SQ}_1 + K_3 \frac{\widetilde{SQ}_1 \widetilde{SQ}_2}{\widetilde{SQ}_3} + K_4 \frac{\widetilde{SQ}_1 \widetilde{SQ}_2}{\widetilde{SQ}_3}}\right] \tag{5.57}$$

This is entirely equal to the situation in Eq. (5.56) and all singularities are removed in this particular term but for the term with $i = 3$ and $j = 1$ or 2 (or the other way around) something else might happen. Looking at one of those terms

$$Im \left[(\gamma_2 - \gamma_3)^2 \frac{K_2 K_3}{K_1 \frac{\widetilde{SQ_2}\widetilde{SQ_3}}{\widetilde{SQ_1}} + K_2 \widetilde{SQ_3} + K_3 \widetilde{SQ_2} + K_4 \widetilde{SQ_2}} \right] \tag{5.58}$$

Here the whole term vanishes for $\widetilde{SQ_1} = 0$ and for $\widetilde{SQ_2} = 0$ and $\widetilde{SQ_3} = 0$ there is always one finite term left in the the denominator. So in this particular term of the sum also all singularities are removed. The last term that could show a different behavior is the one with $i = 3$ and $j = 4$

$$Im \left[(\gamma_3 - \gamma_4)^2 \frac{K_3 K_4}{K_1 \frac{\widetilde{SQ_3}^2}{\widetilde{SQ_1}} + K_2 \frac{\widetilde{SQ_3}^2}{\widetilde{SQ_2}} + K_3 \widetilde{SQ_3} + K_4 \widetilde{SQ_3}} \right] \tag{5.59}$$

Here the whole term vanishes for $\widetilde{SQ_1} = 0$ and $\widetilde{SQ_2} = 0$ and when $\widetilde{SQ_3}$ hits zero it approaches infinity. So if the two gap parameters Δ_i and Δ_j are equal the corresponding term in the sum of Eq. (5.52) exhibits a singularity at $\omega = 2\Delta_i$. This means that for the other cases of $\widetilde{SQ_1} = \widetilde{SQ_2} \neq \widetilde{SQ_3} = \widetilde{SQ_4}$ and $\widetilde{SQ_1} \neq \widetilde{SQ_2} = \widetilde{SQ_3} = \widetilde{SQ_4}$ there will also be a singularity at any gap value that is present in more than one band. Explicitly meaning that the former case shows two and the latter one only one singularity. In general one can say that the singularities at uniquely present gap values get removed and the other ones don't. This behavior is displayed in Fig. 5.10 for four bands with different verteces.

Raman response of the 4 band Fermi surface with the ARPES data

Now the effective masses of Table 5.1 will be used for plotting the Raman response of the band structure displayed in Fig. 5.1. Recent Muon Spin Rotation measurements of the magnetic field penetration depth of a member of the ironpnictide family point towards a multi-gapped Fermi surface with two gaps that differ roughly by a factor of two [67]. Furthermore ARPES measurements show that the smaller gap value corresponds to the outer Γ barrel (yellow circle in Fig. 5.1) and that all other bands exhibit the larger gap value [61] (for a more detailed discussion of gap distribution and values see Chapter 3, Section 2). These results will now be used to plot the unscreened and screened Raman response in A_{1g}
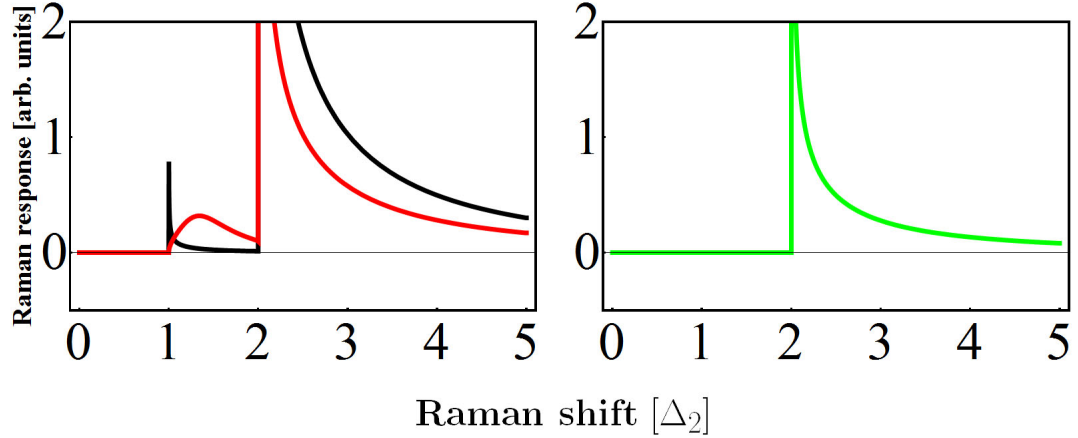
Figure 5.11: **Left:** Comparison of the unscreened (black) and screened (red) Raman response for the bands displayed in Fig. 5.1 with the effective masses in Table 5.1 in A_{1g} symmetry. There are two hole-like parabolic, one electron-like parabolic and four equal hole-like elliptical bands in the first Brioullin zone that contribute to this plot. One parabolic band is taken to have a different gap value Δ_1 with $2\Delta_1 = \Delta_2$. The singularity at twice the smaller gap value is removed since it is unique and the singularity at twice the bigger gap value remains since three bands share this gap value. In between the two locations of twice the gap values there is a bell shaped peak. **Right:** Raman response of the same bands as in the left panel in B_{2g} symmetry. Only the four elliptical bands with the same gap contribute in this channel resulting in the trivial square root singularity response.

symmetry and the unscreened response in B_{2g} symmetry which is the only non-symmetric contributing channel in the applied model. The response in A_{1g} symmetry is shown in the left hand side of Fig. 5.11. The unscreened (black) response shows the two square root singularities at twice the gap values and the screened (red) response exhibits exactly the behavior expected from the discussion in the preceding subsection. The singularity at twice the uniquely present gap value is removed while the one at twice the gap value of the three other bands remains. In between the two singularities a bell shaped peak is observed which is explained by the extensive investigations in the two band case. There is a term with different gaps and different verteces in the sum of the four band response which produced this shape in the the corresponding two band case (see Fig. 5.8 and Fig. 5.9). The response in B_{2g} symmetry, displayed in the right hand side of Fig. 5.11, does not show any nontrivial features. Since only the elliptical bands contribute to the response because the verteces of all not fully symmetric channels are vanishing for parabolic bands and since those four

elliptical bands (two brown and two magenta ones from Fig. 5.1) all have the same vertex and gap value only a simple square root singularity is produced. Possible nontrivial features through screening are also not present for the entirely unscreened B_{2g} channel.

5.2.4 Superconducting gap parameter of extended s-wave character

Momentum dependence of the gap

The so far done investigations all included a constant gap parameter over the whole BZ which means that it did not have any k-dependence and thus it did not matter where the particular band crossed the Fermi surface. Only the effective mass of the band was important for the Raman response since it solely determined the Raman vertex and set the value of the density of states together with the area of the unit cell. With a k-dependent
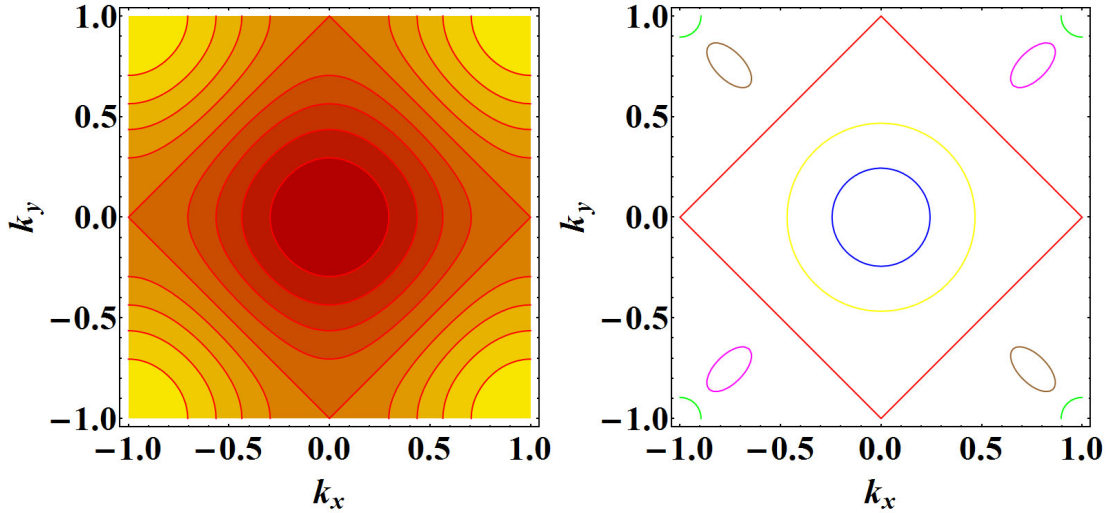
Figure 5.12: **Left:** Contourplot of the extended s-wave gap. The darkest area in the middle is the maximum and the lightest areas in the corners are the minimums. **Right:** Fermi surface sheets of the free electron bands of the used model (coloring equal to Fig. 5.1). The red square represents the nodes of the extended s-wave gap.

gap parameter it is crucial where the band hits the Fermi surface since the value of the gap parameter at this point in k-space determines the minimum energy to excite a quasi particle out of the condensate. Unless the k-dependence of the gap is equal to the one of the band there are now different values of the gap along the Fermi surface sheet with a minimum as well as a maximum gap value and depending on the chosen gap symmetry even nodes

are possible. Such nodes result in a vanishing gap and thus every finite energy is able to excite quasi particles at the points of the nodes in k-space. Recent measurement of flux quantum jumps in rings of ironpnictide superconductors [73] show that the pairing in these material is spin-singlet with even parity and that the gap parameter changes its sign. This points towards an extended s-wave symmetry of the gap parameter that can be analytically expressed by $\Delta(\mathbf{k}) = \Delta_0 \left(\cos(\pi k_x) + \cos(\pi k_y) \right)$ [94] with k_x and k_y again running from -1 to 1 like in the previous sections (a more detailed discussion of gap symmetry can be found in Chapter 3, Section 2). The contour of this gap is shown on the left hand side of Fig. 5.12 and one can see that it exhibits a squarish k-dependence resulting in a variation of the gap value along the circular or elliptical Fermi surface sheets of the used bands. Furthermore this gap has a sign change between the Γ and the M point with the nodes located on the red line shown on the right hand side of Fig. 5.12 together with the free electron bands of the applied model. These nodes do not cross the Fermi surface sheets of any band and thus the gap value remains finite on all of them but through the different Fermi momenta of the bands the gap value will now differ from one to another.

Numerical calculation of the Raman response

Introducing the above mentioned k dependent gap makes it no longer possible to calculate the Raman response entirely analytical like it was done in the previous section. Here the evaluation of the Raman response for the nth band

$$\chi_{\gamma\gamma,n}(\omega) = \frac{1}{N} \sum_{\mathbf{k}} \gamma_n^2 \frac{4\Delta_n^2(\mathbf{k})}{E_n(\mathbf{k}) \left[4E_n^2(\mathbf{k}) - (\omega + i\alpha)^2 \right]} \tag{5.60}$$

will be done entirely numerically with the program `Mathematica`. Replacing the sum over $\mathbf{k}$ by two integrals over k_x and k_y and then transforming into polar coordinates results in

$$\chi_{\gamma\gamma,n}(\omega) = \frac{A}{(2\pi)^2} \gamma_n^2 \int_0^{2\pi} d\theta \int_0^{k_{1stBZ}} kdk \frac{4\Delta_n^2(k,\theta)}{E_n(k,\theta) \left[4E_n^2(k,\theta) - (\omega + i\alpha)^2 \right]} \tag{5.61}$$

where k_{1stBZ} stands for the k-value corresponding to the rim of the 1st BZ. First of all the two Γ-parabolas will be considered since those are the easiest cases. They are written out explicitly in polar coordinates

$$\epsilon_\Gamma(k,\theta) = \frac{k^2}{2m_\Gamma^*} - \mu_\Gamma \tag{5.62}$$

With both bands being centered in the middle of the BZ shown in Fig. 5.12 no shift has to be done and with the already circular Fermi surface sheet no transformation has to be done either to simplify the numerical integration in polar coordinates. For the M-pocket band a coordinate shift of $k_{sx} = k_{sy} = 1$ has to be done to place the circular Fermi surface sheet of the band in the middle of the BZ. This shift has to be done for the gap as well resulting in a shift by π in the argument of both cosines which is equal to a sign switch of the entire gap function. Since the gap only enters squared in Eq. (5.61) (in the numerator as well as in the quasi particle energy $E_n(k, \theta)$) this sign switch will have no influence on the response and thus the M-pocket can be evaluated in the same way as the Γ-parabolas. Taking a closer look at the integrand of Eq. (5.61) reveals its 8-fold symmetry and thus only $\frac{1}{8}$th of the BZ has to be integrated. This leads to the following integral for all circular bands in the used model

$$\chi_{\gamma\gamma,i}(\omega) = 8 \times \frac{A}{(2\pi)^2} \, \gamma_i^2 \int_0^{\frac{\pi}{4}} d\theta \int_0^{\frac{1}{\cos(\theta)}} k dk \frac{4\Delta_i^2(k, \theta)}{E_i(k, \theta) \left[4E_i^2(k, \theta) - (\omega + i\alpha)^2\right]} \tag{5.63}$$

Here the index i stands for all the parabolic bands as in the previous section. The evaluation of the blades needs a little more care since they are not centered at a high symmetry point. The explicit representation of the magenta blade in the upper right of the picture on the
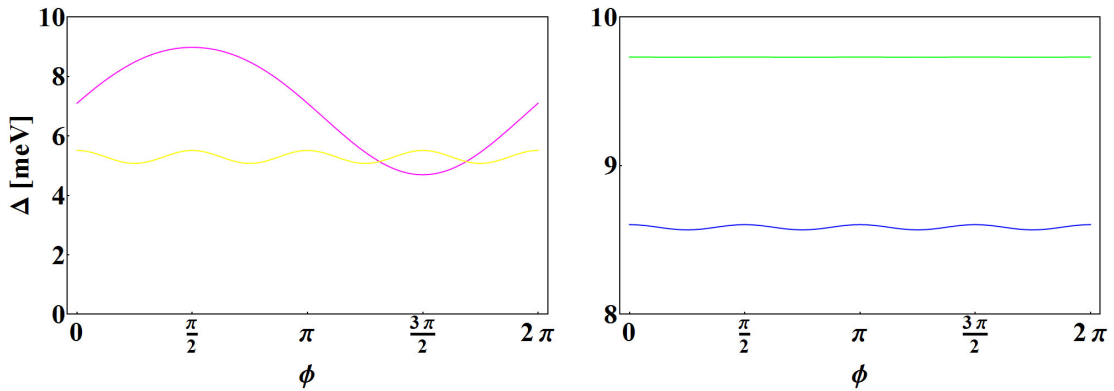
Figure 5.13: Comparison of the absolute value of the extended s-wave gap at the Fermi momentum for the different bands after the transformation into polar coordinates. The colors correspond to the bands in Fig. 5.12. All bands are $\frac{\pi}{2}$-periodic except the one for the blade (magenta). The variation of the gap corresponding to the M-pocket (green) is not resolved in this energy scale but is the same as for the ones corresponding to the Γ-parabolas (yellow, blue).

left hand side in Fig. 5.12 is

$$\epsilon_{bl}(k,\theta) = \frac{1}{m^*_{x+y}}\left(\frac{(k_x - k_0) + (k_y - k_0)}{\sqrt{2}}\right)^2 + \frac{1}{m^*_{x-y}}\left(\frac{(k_x - k_0) - (k_y - k_0)}{\sqrt{2}}\right)^2 - \mu_{bl} \quad (5.64)$$

with $k_0 = 1 - \frac{0.346}{\sqrt{2}}$. After a shift by $k_{sx} = k_{sy} = k_0$ and the transformation of

$$K_x = \frac{k_x + k_y}{\sqrt{2}}$$
$$K_y = \frac{m^*_{x-y}}{m^*_{x+y}}\frac{k_x - k_y}{\sqrt{2}} \quad (5.65)$$

polar coordinates can be introduced in the same way as before and the energy band of the blade is

$$\epsilon_{bl}(K,\theta) = \frac{K^2}{2m^*_{x+y}} - \mu_{bl} \quad (5.66)$$

This exhibits the same form as the parabolic bands with a constant Fermi momentum which makes the numerical integration in polar coordinates easier. The disadvantage of this transformation is that the energy gap will look more complicated in this case. The momenta k_x and k_y have to be expressed in the new coordinates which leads to

$$k_x = k_0 + \frac{K_x + \frac{m^*_{x+y}}{m^*_{x-y}}K_y}{\sqrt{2}}$$
$$k_y = k_0 + \frac{K_x - \frac{m^*_{x+y}}{m^*_{x-y}}K_y}{\sqrt{2}} \quad (5.67)$$

Inserting these into the gap and transforming into polar coordinates with the new K's gives the gap in the following form.

$$\Delta_{bl}(K,\theta) = \Delta_0 \left[\cos\left(\pi\left(k_0 + \frac{K\cos(\theta) + \frac{m^*_{x+y}}{m^*_{x-y}}K\sin(\theta)}{\sqrt{2}}\right)\right)\right.$$
$$\left. + \cos\left(\pi\left(k_0 + \frac{K\cos(\theta) - \frac{m^*_{x+y}}{m^*_{x-y}}K\sin(\theta)}{\sqrt{2}}\right)\right)\right] \quad (5.68)$$

This gap shows no more symmetry in θ and the integration has to run from 0 to 2π which can be explicitly seen in the angular variation of the absolute value of the gaps for all bands at the Fermi momentum in Fig. 5.13. In the new polar coordinates the Raman response for the blade can be written as

$$\chi_{\gamma\gamma,bl}(\omega) = \frac{A}{(2\pi)^2}\gamma_n^2\frac{m^*_{x+y}}{m^*_{x-y}}\int_0^{2\pi}d\theta\int_0^{K_{1stBZ}}KdK\frac{4\Delta_{bl}^2(K,\theta)}{E_{bl}(K,\theta)\left[4E_{bl}^2(K,\theta) - (\omega + i\alpha)^2\right]} \quad (5.69)$$

K_{1stBZ} is taken to be simply 1 which misses the corners of the 1st BZ but those only have a vanishingly small contribution and can be neglected. To run the numerical integration the value of $\Delta_0 = 10meV$ is chosen which is ruffly the same as the one obtained by ARPES measurements in [61] and still in the same order of magnitude as the measured value by muon spin rotation in [67] (more gap mesurements are cited in Chapter 3, Section 2). The broadening parameter α will be chosen to be $\alpha = 0.01meV$ and is caused by impurity scattering in the material. In order to simplify the numerical integration the momentum integration is split into several parts wherever the integrand shows roots in the denominator. The upper integration boundary of the integral over the smaller momenta and the lower integration boundary of the integral over the bigger momenta will be at exactly those k-values of the roots. This helps the program to deal with the singularities and speeds up the evaluation tremendously.

Single band responses

The Raman responses of the single bands are shown in Fig. 5.14. The real parts of the single band response with the extended s-wave gap are displayed in brown for all bands and the imaginary parts are again colored like in Fig. 5.12. The inner Γ-parabola (blue) has the minimum gap value at k_F of about $\Delta_{min,\Gamma i} = 8.57meV$ and the maximum gap value at k_F of about $\Delta_{max,\Gamma i} = 8.60meV$ which is roughly seen in the right panel of Fig. 5.13. At twice the minimum gap value at k_F the response shows a threshold which slowly develops into a peak at twice the maximum gap value. This behavior can only be seen in the zoomed in response shown in the inset of this plot since the values are too close together to be resolved in the entire plot. The M-pocket (green) shows the exact behavior with the only difference that because of the even closer minimum $\Delta_{min,Mp} = 9.730meV$ and maximum $\Delta_{max,Mp} = 9.731meV$ gap values at k_F an even closer zoom was necessary to resolve the structure. The tiny separation between the extreme values of the gap at k_F for those two bands was already shown in Fig. 5.13 and has its origin in the flatness of the gap near the extremal points in the middle and the corners of the BZ. Since the crossing with the Fermi surface of the outer Γ-parabola (yellow) is located further away from the Γ-point the minimum $\Delta_{min,\Gamma 0} = 5.08meV$ and maximum $\Delta_{max,\Gamma o} = 5.51meV$
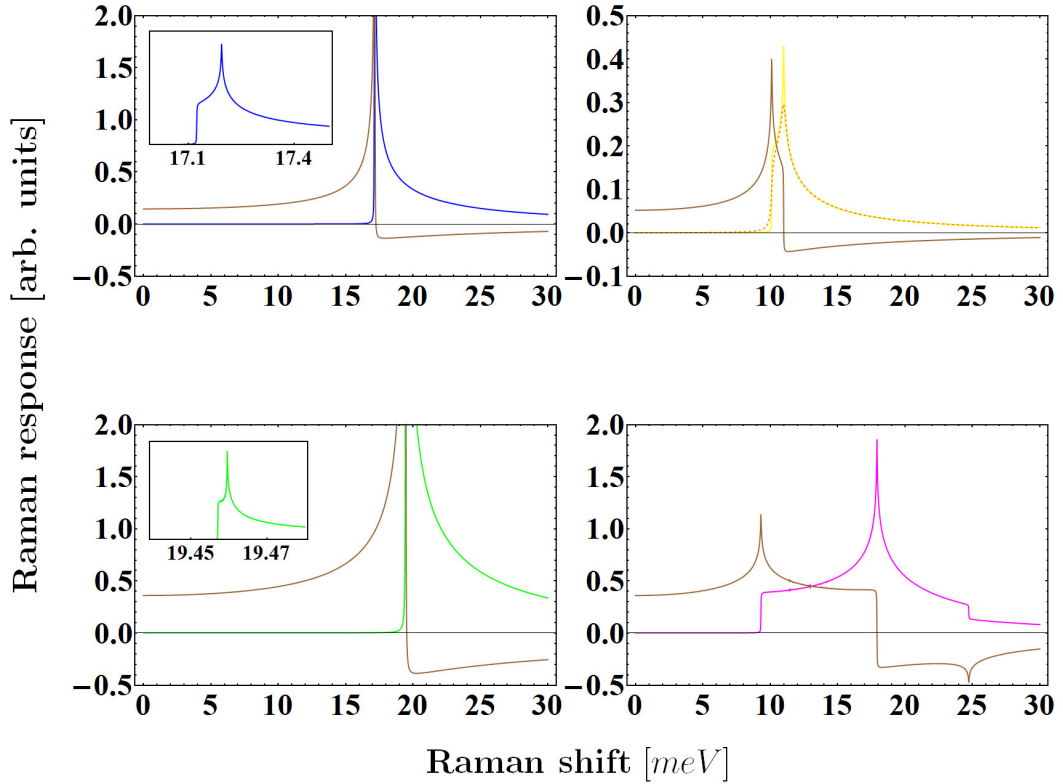
Figure 5.14: Real (brown) and imaginary (coloring as in Fig. 5.12) parts of the Raman response of all single bands with extended s-wave gap. All bands show a threshold at twice the minimum gap value and a peak at twice the maximum gap value which is shown in the insets for the bands where the extreme values of the gaps are to close to each other to be resolved in the larger image. The orange dotted line in the upper right plot is the outer Γ-parabola with a ten times larger broadening parameter α. The comparison of both peaks with different broadening shows how a lager broadening effects the shape of the peaks.

Fermi level gap values are further apart (see left hand side of Fig. 5.13) and the threshold-peak structure is resolved in the total plot of the response. The orange dotted line in the upper right panel is also the response of the outer Γ-parabola but with a broadening factor of $\alpha = 0.1meV$ which is ten times larger than the one used for the other responses. The larger broadening rounds up the threshold and the peak size decreases. The response which shows the clearest threshold-peak structure is the one of the blade (magenta) since its Fermi surface sheet is located in a region where the gap changes quite drastically and its minimum and maximum gap values at k_F are $\Delta_{min,bl} = 4.70meV$ and $\Delta_{max,bl} = 8.98meV$ respectively (see also left hand side of Fig. 5.13). Another interesting feature of the blade

is a step discontinuity above the singularity at about $25 meV$. Closer investigations of the integrand show that the denominator looses one of its two roots at exactly this point which results in a sudden fall of the response. The energy value of this feature corresponds exactly to $\omega = 2\sqrt{\mu_{bl}^2 + \Delta_{bl,center}^2}$ where $\Delta_{bl,center}$ is the gap value at the center of the blade. This ω denotes the top of the blade bands in the superconducting state above which no more quasi particles can be excited. At all discontinuities of the imaginary parts of the responses the real parts exhibit a peak and at peaks of the imaginary parts the real parts show a discontinuity.

At this point it is very interesting to investigate whether the peak at twice the larger gap value is a singularity that appears to be finite because of the included broadening or has a finite value by itself making it a cusp rather than a singularity. Furthermore it is interesting why the response starts with a threshold and not with a power law onset or a singularity. To clarify those issues a simpler analytical representation of the gap is chosen that only has an angular dependence but exhibits an equal behavior to the extended s-wave gap. The model gap will be taken to be

$$\Delta(\theta) = \Delta_{off} + \Delta_0 \cos(4\theta) \tag{5.70}$$

This gap shows a very similar angular dependence as the ones for all parabolic bands (see Fig. 5.13) and the two parameters Δ_{off} and Δ_0 define the size of the offset and the angular variation, respectively. It is important that $\Delta_{off} > \Delta_0$ so that there are no nodes in the gap contrary to the one used above. The integral that has to be evaluated is the same as in Eq. (5.13). With the new gap and after dropping the sum and the band index n it is

$$Im\left(\chi_{\gamma\gamma}(\omega)\right) = \gamma^2 \frac{8N_F}{\omega} \int_a^{\frac{\pi}{4}} d\theta \frac{(\Delta_{off} + \Delta_0 \cos(4\theta))^2}{\sqrt{\omega^2 - 4\left(\Delta_{off} + \Delta_0 \cos(4\theta)\right)^2}} \tag{5.71}$$

The lower integration boundary a is chosen to make sure that the square root stays real and will be $a = \frac{1}{4}\arccos\left(\frac{\omega - 2\Delta_{off}}{2\Delta_0}\right)$ from $\omega = 2\Delta_{off} - 2\Delta_0$ until $\omega = 2\Delta_{off} + 2\Delta_0$ which corresponds to twice the minimal and maximal gap values respectively. Above the latter value the integration will start at $a = 0$ and below the former value it will start at $a = \frac{\pi}{4}$ which makes the integral vanishing. The extra 8 comes from the initial integral running

from 0 to 2π which was reduced to $\frac{1}{8}$ because of the 8-fold symmetry of the integrand. Applying the transformation

$$x = \Delta_0 \cos(4\theta) \tag{5.72}$$

leads to

$$Im\left(\chi_{\gamma\gamma}(\omega)\right) = \gamma^2 \frac{N_F}{\omega} \int_{-\Delta_0}^{b} dx \, \frac{2}{\sqrt{(\Delta_0 + x)(\Delta_0 - x)}}$$
$$\times \frac{(\Delta_{off} + x)^2}{\sqrt{(\omega + 2\Delta_{off} + 2x)(\omega - 2\Delta_{off} - 2x)}} \tag{5.73}$$

The integrand has square root singularities one at $x = \pm\Delta_0$ and at $x = \pm\frac{\omega}{2} - \Delta_{off}$. Since the integration over θ ran from a to $\frac{\pi}{4}$ the new boundaries are b and $-\Delta_0$. The integration has to cancel below $\omega = 2(\Delta_{off} - \Delta_0)$ and only runs from $-\Delta_0$ to $\frac{\omega}{2} - \Delta_{off}$ until this value reaches Δ_0 so $b = -\Delta_0$ if $\frac{\omega}{2} - \Delta_{off} < -\Delta_0$, $b = \frac{\omega}{2} - \Delta_{off}$ if $-\Delta_0 \leq \frac{\omega}{2} - \Delta_{off} < \Delta_0$ and $b = \Delta_0$ if $\frac{\omega}{2} - \Delta_{off} > \Delta_0$. Hence the integral is zero below $\omega = 2(\Delta_{off} - \Delta_0)$ which is twice the minimal gap value. Above $\omega = 2(\Delta_{off} + \Delta_0)$ there are no singularities since x only runs from $-\Delta_0$ to Δ_0 but in between those values where $b = \frac{\omega}{2} - \Delta_{off}$ special care has to be taken to find out what exactly happens at the values of interest which are twice the extremal gap values. A twice the minimal gap value the integral can be written as

$$Im\left(\chi_{\gamma\gamma}(2(\Delta_{off} - \Delta_0))\right) = \lim_{\epsilon \to 0} \gamma^2 \frac{N_F}{\omega} \int_{-\Delta_0}^{-\Delta_0 + \epsilon} dx \, \frac{1}{\sqrt{(\Delta_0 + x)(\Delta_0 - x)}}$$
$$\times \frac{(\Delta_{off} + x)^2}{\sqrt{(2\Delta_{off} - \Delta_0 + \epsilon + x)(-\Delta_0 + \epsilon - x)}} \tag{5.74}$$

At this particular ω two of the square root singularities coincide and become a singularity at $x = -\Delta_0$ with the power 1 but since the integration runs only over an infinitesimally small value ϵ the integral remains finite. This explains why the threshold observed at twice the minimal gap value in Fig. 5.14 is not singular nor a power law onset but a step discontinuity. At twice the maximal gap value the integral is equal to

$$Im\left(\chi_{\gamma\gamma}(2(\Delta_{off} + \Delta_0))\right) = \lim_{\epsilon \to 0} \gamma^2 \frac{N_F}{\omega} \int_{-\Delta_0}^{\Delta_0 - \epsilon} dx \, \frac{1}{\sqrt{(\Delta_0 + x)(\Delta_0 - x)}}$$
$$\times \frac{(\Delta_{off} + x)^2}{\sqrt{(2\Delta_{off} + \Delta_0 - \epsilon + x)(\Delta_0 - \epsilon - x)}} \tag{5.75}$$

The square root singularity at $x = -\Delta_0$ is now present only once so it remains integrable and is removed after the integration. Whereas there are again two square root singularities coinciding to form a singularity of power 1 at $x = \Delta_0 - \epsilon$ but this time the integration

is running over a finite value thus the integral has a log-singularity at this point. This clarifies the issue of the finite value at twice the maximum gap value in Fig. 5.14. It is a log-singularity that just appears to be finite because of the broadening factor α. As soon as one takes the gap value to be constant again by setting the size of the angular variation to $\Delta_0 = 0$ it is possible to take the whole fraction containing the gap out of the integral. This will be just a constant and the square root singularity at twice the gap value is reproduced. Hence the model above properly reduces to the constant gap case discussed in the previous part of this chapter. In conclusion one can say that an angular dependence in the gap does not entirely remove the singularity in the constant gap case but it significantly weakens it and instead of a square root singularity a log-singularity an a threshold are obtained.

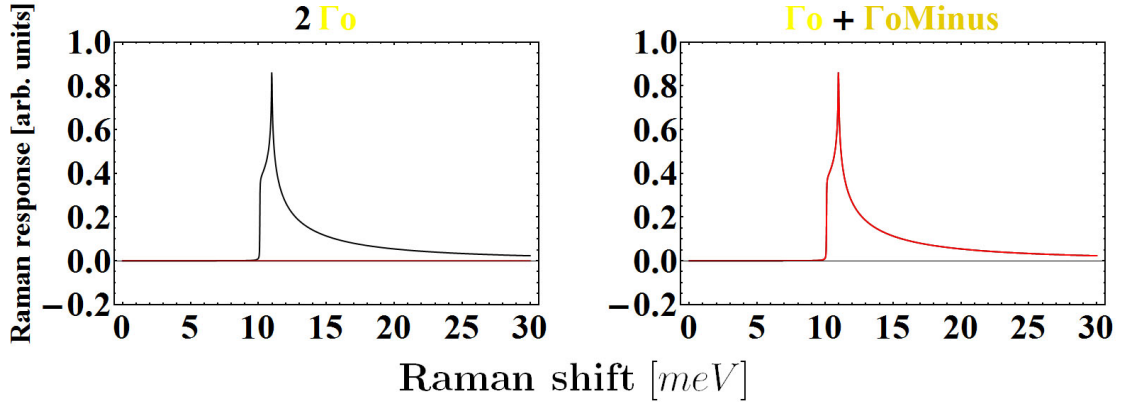**Screened multiband responses in A_{1g} symmetry**

Figure 5.15: Comparison of the unscreened (black) and screened (red) Raman responses in A_{1g} symmetry for two outer Γ-parabolas. The regular hole-like Γ-parabola is denoted with Γo and the electron-like Γ-parabola with ΓoMinus. **Left:** Both bands are hole like and the screened response is vanishing due to the exactly equal verteces of both bands that cancel each other. **Right:** One band is electron and the other is hole like which makes the equal verteces add up and the unscreened and screened responses equal since the screening term is vanishing.

Now the interplay of two bands will be considered with all the single bands of the applied free electron model. First the extreme cases of perfect and vanishing screening that occurred in the constant gap case are reproduced. In order to have the case of equal verteces for two bands, which led to vanishing response and thus perfect screening, the unscreened and screened response of two outer Γ-parabolas (Γo) is plotted. This is displayed in the left

hand side of Fig. 5.15 and indeed the screened response (red) is vanishing for all energies. The other extreme case of vanishing screening, that occurred for equal absolute values of the verteces but opposite signs, is realized by transforming the outer Γ-parabola into an electron-like band by flipping the sign of the effective mass and the sign of the chemical potential. The interplay of the hole-like outer Γ-parabola and the electron-like outer Γ-parabola (ΓoMinus) is plotted in the right hand side of Fig. 5.15. Here the unscreened (black) and screened (red) responses are equal for all energies which shows that the screening term indeed vanishes. So both of the extreme constant gap cases are succesfully reproduced with the k-dependent extended s-wave gap. The interplay of all the other bands with each other, not with themselves of course, should show a behavior similar to the different vertex and different gap cases shown in Fig. 5.8 and Fig. 5.9 since the different bands have different masses and different Fermi momenta which produce different verteces and different minimum and maximum gap values respectively. The latter ones are responsible for the thresholds and the log-singularities which certainly are different for all the bands as seen in Fig. 5.14. In Fig. 5.16 the A_{1g} channel Raman responses for all possible combinations of two different bands are shown. The black curve is the unscreened, the red curve the screened response and the cyan curve represents the screening term without the minus. In the left column the interplay of two hole-like bands is displayed. The log-singularities in the unscreened response are removed in the screened one since the screening term exhibits the same log-singularities. What is left in the screened response is the same dome-like shape as in Fig. 5.8 and Fig. 5.9 in between the positions of the two log-singularities. This shape is slightly altered in the two lower cases by the additional features of the threshold-log-singularities structure caused by the angular variation of the gap along the Fermi surface sheet. The vertex difference is rather small in all three cases since in the hole-hole case the verteces are subtracted from each other (see Eq. (5.52)) which makes the the whole response smaller than for verteces with opposite signs. This vertex-difference is increasing from the top to the bottom plot resulting in the increasing response especially for the bottom plot. The low response for the middle plot is a consequence of the log-singularity positions being located close to each other.
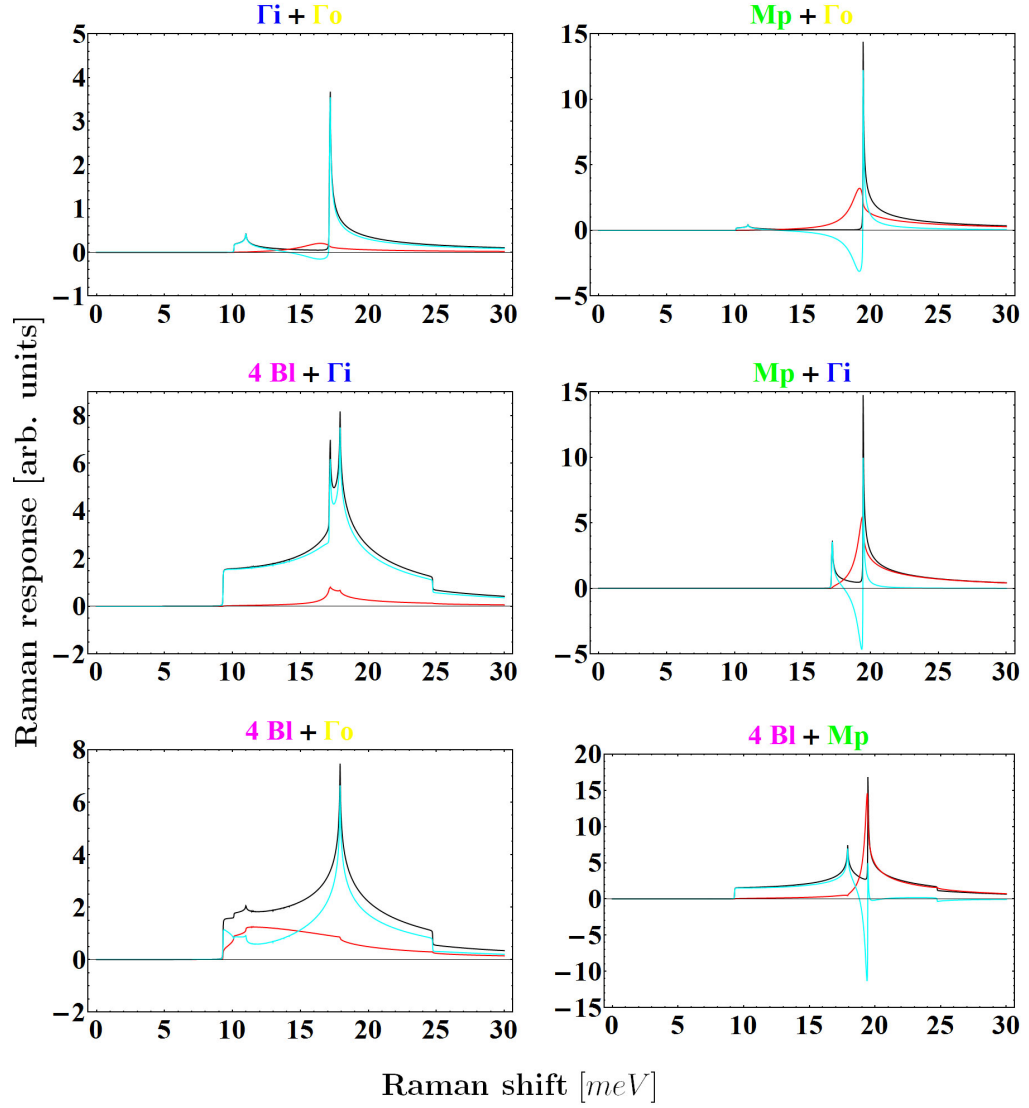
Figure 5.16: Comparison of the unscreened (black) and screened (red) Raman responses with the extended s-wave gap parameter for all possible combinations of two bands in A_{1g} symmetry. The screening term without the minus is shown in cyan. In the left column the response of two hole-like bands and in the right column the one for an electron-like and a hole-like band is displayed. In all plots the log-singularities of the unscreened response are removed by similar ones occurring in the screening term and a dome-like shape in between the positions of the singularities is produced.

Short after the increase above the energetically lower log-singularity the screened response is dominated by the fall off above the energetically higher log-singularity making the width of the dome very small. The log-singularity positions are way further apart in the bottom plot which leads to a much broader response in the screened case. The right column shows the possible electron-hole responses with the four used bands of the model. As expected the screened responses are now bigger than for the bands with equal signs since the verteces now add up in Eq. (5.52). The peaks are getting bigger and sharper for
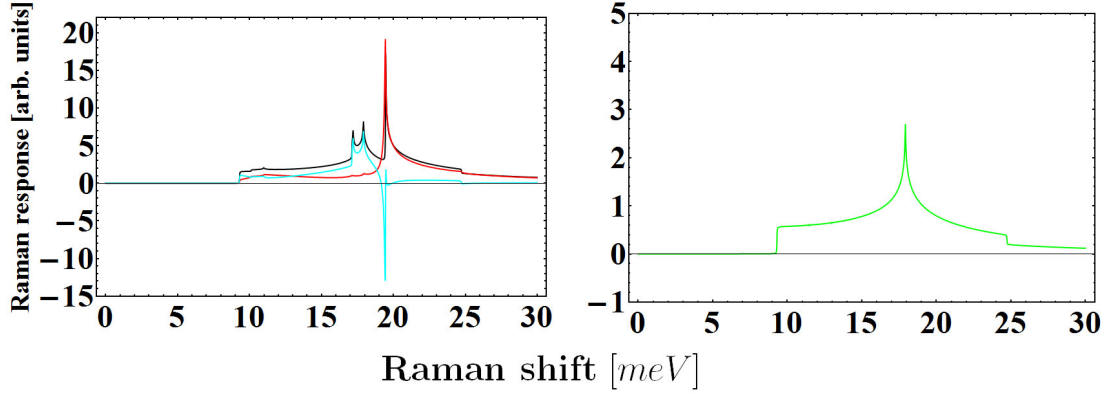

Figure 5.17: Raman response for all four bands in the 1st BZ with extended s-wave gap parameter in A_{1g} and B_{2g} symmetry. **Left:** Comparison of the unscreened (black) and screened (red) response in A_{1g} symmetry. The screening term without the minus is shown in cyan. The screened response is dominated by the sharp, almost singularity-like dome slightly below the position of the log-singularity of the M-pocket and has a flat structure below it starting at the location of the threshold of the blade. **Right:** Raman response in B_{2g} symmetry. Since the verteces of all other bands are equal to zero it is only the four blades that contribute to this channel.

the increasing vertex difference from the top to the bottom and they are located close to the position of the log-singularity of the M-pocket which means the band with the smaller mass, again similar to the plots in Fig. 5.8 and Fig. 5.9. Furthermore Eq. (5.52) shows that the screened multi-band response is a sum of all possible screened two-band responses normalized by a sum including all bands. This explains the Raman response including all four bands for A_{1g} symmetry displayed in the left hand side of Fig. 5.17. The unscreened response is again black, the screened one is red and the screening term without the minus is shown in cyan. It is obvious that the dominating terms in the sum of the two band responses are the ones including the M-pocket since those are the ones with the biggest responses

in Fig. 5.16 because of the much larger vertex difference. Thus the main feature of the screened four-band response is a sharp peak close to the position of the log-singularitiy of the M-pocket produced by the peaks of response terms including the M-pocket summing up at this point. The features of all other two band responses are small compared to this and result in a broad flat region in between the threshold of the blade, which is energetically the smallest point of twice an extremal value of a gap, and the M-pocket log-singularity. The right hand side of Fig. 5.16 shows the four-band response in B_{2g} symmetry. It only consists of the four blades since for all other bands the vertex in this symmetry channel is vanishing. Without any screening in this channel the response shows exactly the same behavior as the single band response of the blade.

5.2.5   Shortcomings of the applied model

The free electron model used in this chapter together with ARPES data for the effective masses and chemical potentials had the advantage that as long as the gap was taken to be constant everything could be investigated entirely analytical but through this simplification several things were not taken into account. By assuming a parabolic or elliptical band structure the effective masses of the bands are constants and do not have any k-dependence except for differing in between the two directions along the axes of the ellipse. Together with the effective mass approximation for the Raman verteces this resulted in those quantities being constants as well. Thus the verteces could be taken out of any integral and there was no other influence by them than being a different weighting factor for the different bands. Furthermore the verteces were vanishing in all other channels than the A_{1g} channel for the parabolic bands and for the B_{1g} as well as the A_{2g} channel for the elliptical bands. Hence the response in the B_{2g} symmetry had only a contribution from the elliptical bands and the B_{1g} and A_{2g} channels showed no response at all. Especially for the B_{1g} channel one would expect some features in the Raman response while the A_{2g} is usually not important and thus neglected. A next step in order to include these nontrivial features in the calculation of the Raman response could be done by using a tight binding model for the band structure fitted to the known Fermi momenta and velocities from ARPES measurements. This would lead to a k-dependence in the effective mass and with that also in the Raman vertex. In addition

it is very likely that the B_{1g} channel would not be vanishing any more in such a model. Moreover the performed investigations treated the excited quasi particles as completely noninteracting with each other as well as with the superconducting condensate out of which they are excited. In Raman scattering the incoming photon excites an electron from an occupied state below the Fermi level into an unoccupied state above which means it is a particle-hole excitation. Then the electron falls back on a lower state and a photon is excited. In this so called virtual interband transition the ingoing and outgoing photons have the same difference in energy and momentum as the initial and final states in the clean limit while the electron spin remains unchanged. This process leads to a perturbation H' in the form of an electron density wave that is proportional to the inverse effective mass of the band for photon energies below optically allowed interband transitions [95]. The effect of the perturbation H' in a superconducting material is the breaking of a pair which excites two quasi particles out of the superconducting condensate that continue to interact with each other as well as with the holes left behind in the superconducting condensate. Including those interactions leads to so called vertex-corrections which are for example taken into account in [94] where three types of corrections are considered. Those are particle-particle interactions of the two excited quasi-particles with each other, particle-hole interactions of an excited quasi particle with the hole left behind in the condensate and long-range Coulomb interactions. The latter one is taken into account by including the screening term in A_{1g} symmetry but no detailed diagrammatic treatment comparable to [84] was done in this work.

5.2.6 Comparison to earlier work

An earlier publication by Boyd et al. [96] on theoretical calculations of Raman responses of a Fermi surface with the multi band structure of iron-pnictide superconductors is dealing with similar issues as the work presented in this thesis. The Fermi surface sheets in this paper are taken to be circles and two of them are centered around the Γ-point while two other ones are centered around the X $(\pi, 0)$ and the Y $(0, \pi)$ points. This seems to differ from the observed structure presented in Chapter 3 but is equal since in this publication the electronic BZ and not the BZ of the lattice is used. Thus the BZ is rotated by 45

degrees as well as the symmetry channels B_{1g} and B_{2g} are exchanged in this notation. The Fermi surface of [96] is not taking into account the propeller structure that was recently resolved by ARPES measurements [60, 61] and instead of the propeller a single circle is used. However the main difference between the work done in this thesis and [96] is that Boyd et al. do not use the effective mass approximation which leads to constant verteces for the Free Electron Model with parabolic bands and thus circular sheets. Instead angular dependent verteces are obtained by an expansion in Fermi surface harmonics for cylindrical Fermi surfaces with angle independent prefactors. This leads to nonvanishing verteces in all symmetry channels, except A_{2g} which is not taken into account, in contrast to this thesis where only A_{1g} for all and B_{2g} for the blades contribute. Furthermore the gap is taken to be angular dependent from the beginning on by defining an analytical form that has only an angular dependence, making it vary along the Fermi surface circle, and a parameter to adjust the analytical form to a gap with and without nodes. Screening is included for the A_{1g} channel and later also for not fully symmetric channels which has to be interpreted as at least controversial. Later in that work also other vertex representations allowed by the D^{4h} symmetry, including constants of different signs, and constant gaps of different values are considered. The publication only runs numerical integrations and no analytical explanations for the observed responses are given. The obtained single band responses for the case of a gap without nodes in [96] show the similar main features as in the extended s-wave gap case of this thesis with the threshold onset and the log-singularity. The difference in between their responses and the ones in this thesis comes from the angular dependent verteces that slightly alter the shape of the plots and create different onset behavior where the verteces have nodes. Moreover [96] has responses for all symmetry channels because of the nonvanishing verteces and for the single screened band in A_{1g} symmetry the log-singularity is removed but the entire response it is not vanishing. The case with nodes in the gap shows power law onsets for small energies but since this case is not investigated in this thesis no comparison can be made. In the two band response in A_{1g} symmetry for two bands with the same angular dependent gap with different maximum gap values the peaks of the two bands do not get completely removed as in the constant gap as well as the angular dependent gap case in this thesis. The dome-like shape that is obtained

in the different maximum gap value case (different gap case for the constant gap) is only seen in [96] in the very end where constant gaps of different values are inserted. Boyd et al. show a huge number of cases for the gaps and verteces in their publication but non of the obtained features is closely investigated and the reasons for the threshold, the log-singularities or the removal of those singularities in the screened case remain unexplained. In contrast to that this thesis shows simpler cases of constant verteces a constant gap with varying magnitude on different bands and later on one angular dependent gap with a single analytical form that determines the gap value along the Fermi surface sheets of all bands depending on their location. This makes it possible to explain every observed feature with analytical calculations for the constant gap case and within a slightly simplifying model for the extended s-wave gap case. Thus the presented work certainly adds some deeper understanding to the cases in [96] that are similar to the ones investigated here and draws a complete picture of the Free Electron Raman response in the superconducting state within the effective mass approximation and a constant gap. Furthermore the differences that appear by adding an angular variation to the gap are clearly pointed out and explained completely by analytical calculations. Finally the shown multi band responses could be explained by the features seen in the two band cases through the obtained relation in between the two band and the n band case.

5.3   Summary

The original work presented in this chapter started with the calculation of the unscreened Raman response in a free electron model and further simplifications of zero temperature and a superconducting gap which only had an angular dependence. After that a band structure within a free electron model based on ARPES data consisting of four different bands crossing the Fermi surface was introduced. For these parabolic and elliptical bands the Raman verteces were computed in the effective mass approximation and for a constant gap the real and imaginary part of the single band Raman response were calculated entirely analytically based on the calculations in the first section. With both parts of the Raman response function known analytically a complete picture of the screened multiband Raman response in A_{1g} symmetry could be presented including explanations for all observed features
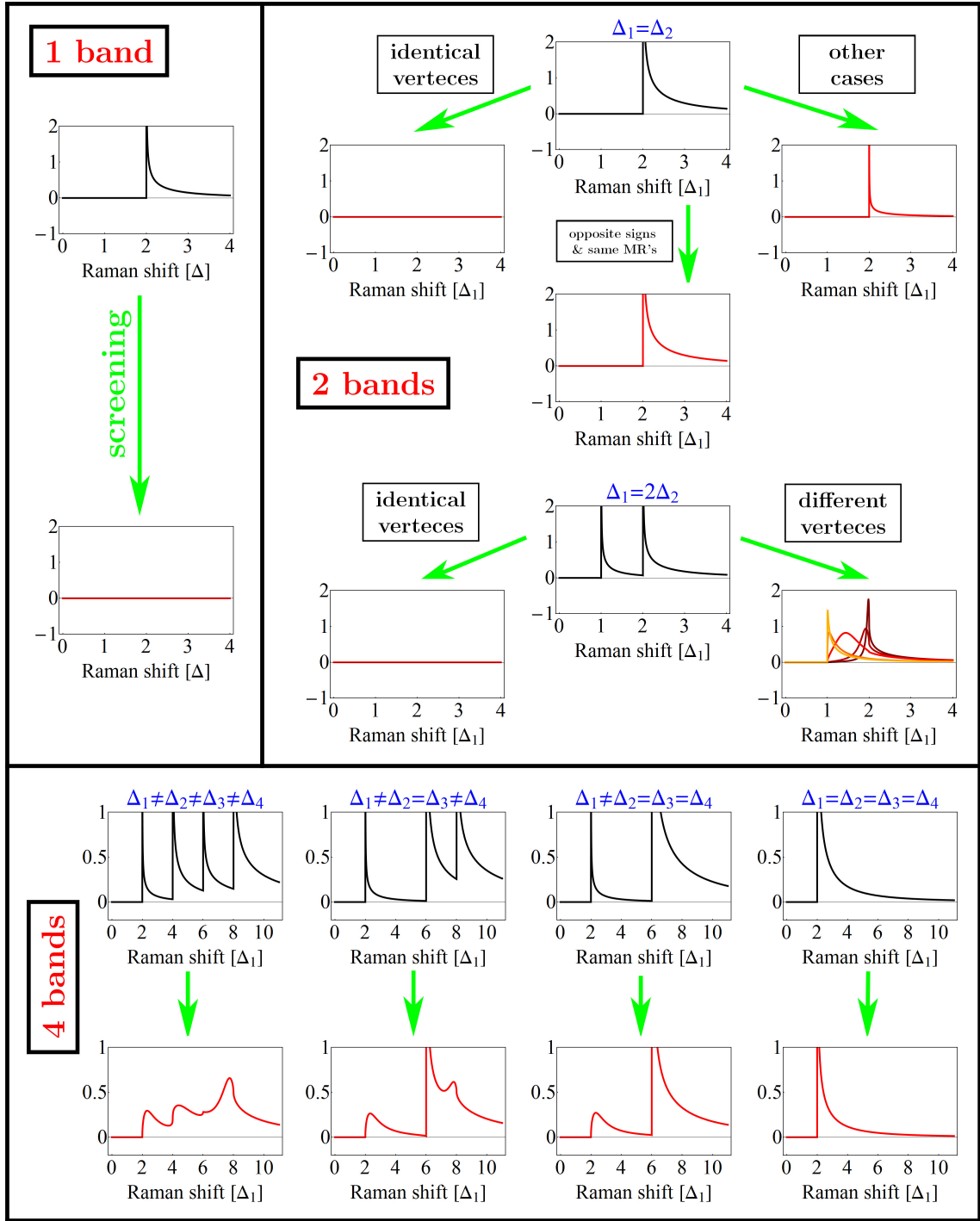
Figure 5.18: Summary map of the effect of screening on the Raman response of one, two and four bands in A_{1g} symmetry for all cases with a constant gap.

by analytical calculations. As a consequence of the applied free electron model with the effective mass approximation for the verteces the other symmetry channels (B_{1g} and A_{2g})

were vanishing or only had a contribution from the elliptical bands (B_{2g}). Fig. 5.18 shows a map that summarizes the different cases of the one, two and four band Raman responses in A_{1g} symmetry with a constant gap that can occur when screening is taken into account. One band shows a square root singularity at twice the gap value in the unscreened case (black curves) and is perfectly screened (screening is represented by the green arrow) hence the screened response (red curves) is vanishing. The same is true for two bands when their verteces are identical regardless of the two gaps being equal or different which is obviously seen in the representation of the screened two band Raman response in Eq. (5.35). The exact opposite namely vanishing screening is obtained if two bands with equal gap values have opposite signs (one electron-like the other one hole-like) and the two effective masses of both bands share the same mass ratio ($MR_n = \frac{m_{n2}^*}{m_{n1}^*}$, $m_{n1,2}^*$ are the effective masses of band n in $k_x + k_y$ and $k_x - k_y$ direction, see 5.2.1). Explicitly this means that two parabolic bands ($MR_n = 1$) of opposite signs are always entirely unscreened in the applied model no matter how different their effective masses are and that the same is true for two elliptical bands ($MR_n \neq 1$) of opposite signs as long as their MR's are equal (see Eq. (5.38)). All other cases for two bands with equal gap values (opposite signs and different MR's, equal signs and different verteces) lead to partial screening that is generally more effective for bands of equal signs and mainly depends on the vertex difference of the two bands (see Eq. (5.35)). A whole new shape is obtained for two screened bands with different gap values and any difference in the verteces. Both singularities are removed and a dome-like shape in between twice the two gap values remains with the exact shape depending on the combination of the effective masses of the two bands (see Fig. 5.8 and Fig. 5.9). Analytical calculations explaining this behavior are given from Eq. (5.40) to Eq. (5.47). By transforming the general form of the screened multiband response into the form presented in Eq. (5.52) it was shown that all combinations of terms of two bands, normalized by all n bands taken into account, sum up to the total n band Raman response. Thus all the results in the two band response investigations can be transfered to the multiband case except the removal of the singularities since this one is influenced by the n band normalization. It turned out that all singularities at twice the uniquely present gap values are removed while singularities at twice a gap value existent on more than one band remain. This is illustrated in the bottom

of Fig. 5.18 for all gaps being different, two being equal, two equal pairs and all gaps exhibiting the same value. The final result in the four band case for the effective masses and gap distribution obtained by ARPES measurements showed a screened A_{1g} response with the square root singularity at twice the smaller gap being removed and the one at twice the larger gap remaining. The B_{2g} response exhibits one simple square root singularity at twice the gap value of the blades since those are the only bands contributing to this channel while the other symmetry channels have no contribution at all (see Fig. 5.11).

In a next step a k-dependent gap was introduced of, the at this moment most promising, extended s-wave symmetry (see upper left of Fig. 5.19) which lead to a threshold at twice the minimum gap value and a log-singularity at twice the maximum gap value in the unscreened single band responses (see upper right Fig. 5.14). Calculations of the responses were done numerically since a completely analytical treatment was no longer possible but the nature of the threshold and the log-singularity could be obtained in an only slightly simplified model (see Eq. (5.70) to Eq. (5.75)). With the vertex and the density of states still being a constant one single band was still perfectly screened (see upper right Fig. 5.19). The two band cases of perfect and vanishing screening (see Fig. 5.15) could only be reproduced with two equal bands (perfect screening) and two equal bands with one of them transformed from hole-like into electron-like (vanishing screening). All other combinations of two different bands corresponded to the different gap and different vertex case since the Fermi momentum, which is different for all bands, determines the extremal gap values with a k-dependent gap. Thus all singularities were removed in the screened two band responses (see middle of Fig. 5.19) as expected from the analytical results in the constant gap case. The contribution of the two band responses to the sum forming the final four band Raman response of the whole 1st BZ (see bottom of Fig. 5.19) is dominated by the features of the terms containing the only electron-like band (see right side of the middle of Fig. 5.19). This was also not surprising since those terms are the ones with verteces of different signs that showed much larger responses in the constant gap cases already. This lead to a screened entire 1st BZ response in A_{1g} symmetry with a sharp peak slightly below twice the maximum gap value of the electron-like M-pocket and a flat broad continuum down to twice the minimal gap
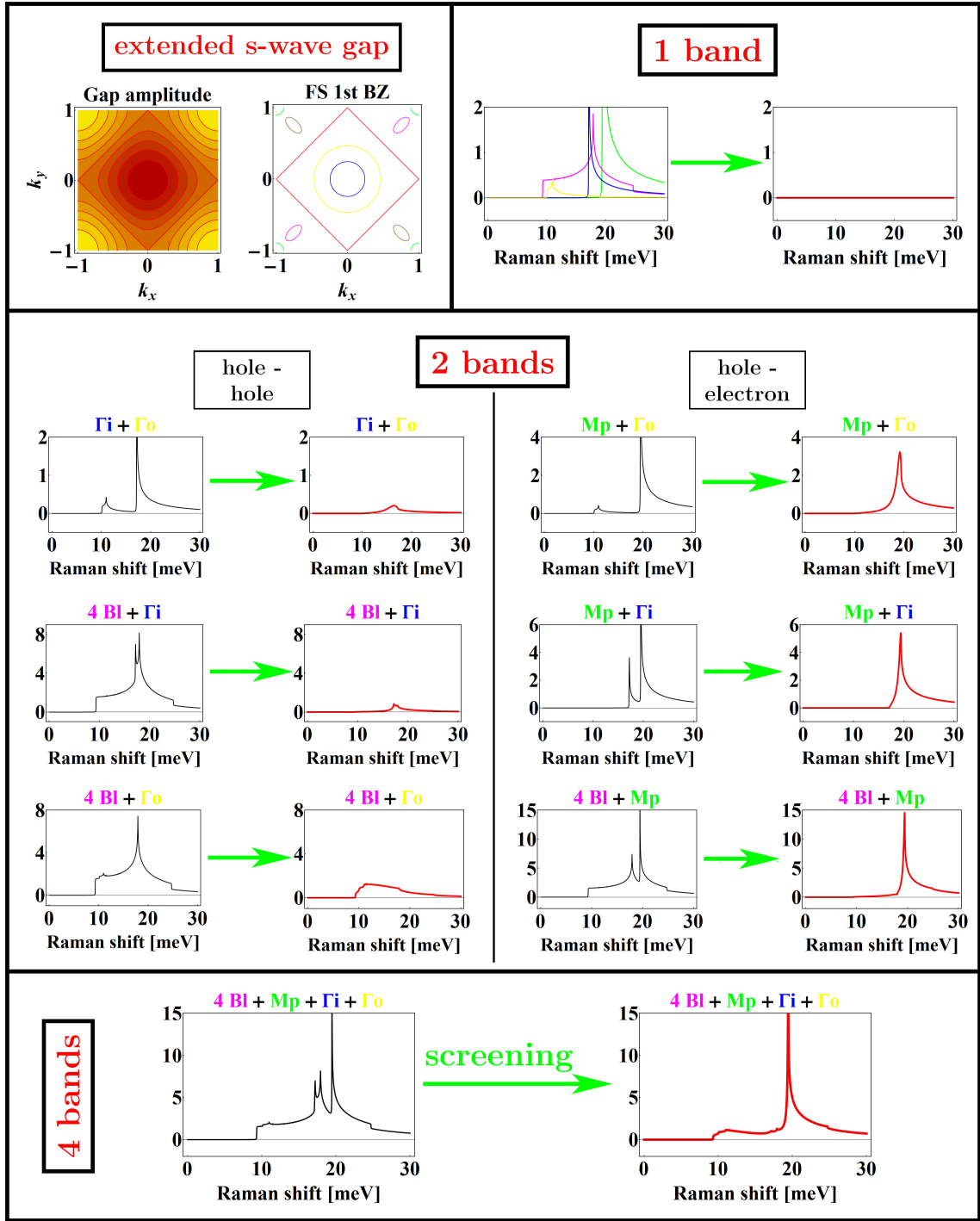
Figure 5.19: Summary map of the effect of screening on the Raman response of one, two and four bands in A_{1g} symmetry for all cases with the extended s-wave gap which is also displayed.

value of the blade (see bottom of Fig. 5.19). The B_{2g} symmetry response again showed the same character as the single band response of the blade with a broad threshold-log-singularity structure and all other channels were again vanishing (see Fig. 5.17). The effect of screening in A_{1g} symmetry on all four single band responses, all possible combinations of two band responses and the four band response is summarized in Fig. 5.19 together with a contour plot and the node of the extended s-wave gap in the 1st BZ.

In the end of this chapter the shortcomings of the applied model are discussed with the main missing feature being vertex corrections that take into account the final state interactions. Finally a comparison to the earlier work of Boyd et al. is done and it is discussed that this thesis provides detailed explanations to the origin of features seen in parts of that earlier publication.

References

[1] H. K. Onnes *Comm. Phys. Lab. Univ. Leiden* **Nos. 119, 120, 122** (1911).

[2] J. R. Schrieffer, *Theory Of Superconductivity*, ch. Appendix: Noble Lecture by J. R. Schrieffer.

[3] W. Meissner and R. Ochsenfeld *Naturwiss.* **21** (1933) 787.

[4] C. J. Gorter and H. G. B. Casimir *Phys. Z.* **35** (1934) 963.

[5] C. J. Gorter and H. G. B. Casimir *Z. Tech. Phys.* **15** (1934) 539.

[6] F. London and H. London *Proc. Roy. Soc. (London)* **A149** (1935) 71.

[7] F. London and H. London *Physica* **2** (1935) 341.

[8] V. L. Ginsburg and L. D. Landau *J. Exptl. Theoret. Phys. (USSR)* **20** (1950) 1064.

[9] E. Maxwell, "Isotope effect in the superconductivity of mercury," *Phys. Rev.* **78** (May, 1950) 477.

[10] C. A. Reynolds, B. Serin, W. H. Wright, and L. B. Nesbitt, "Superconductivity of isotopes of mercury," *Phys. Rev.* **78** (May, 1950) 487.

[11] H. Fröhlich, "Theory of the superconducting state. I. The ground state at the absolute zero of temperature," *Phys. Rev.* **79** (Sep, 1950) 845–856.

[12] A. B. Pippard *Proc. Roy. Soc. (London)* **A216** (1953) 547.

[13] J. Bardeen, "Theory of the meissner effect in superconductors," *Phys. Rev.* **97** (Mar, 1955) 1724–1725.

[14] *Encyclopedia Of Physics, Vol. 15.*

[15] L. N. Cooper, "Bound electron pairs in a degenerate fermi gas," *Phys. Rev.* **104** (Nov, 1956) 1189–1190.

[16] J. Bardeen, L. N. Cooper, and J. R. Schrieffer, "Microscopic theory of superconductivity," *Phys. Rev.* **106** (Apr, 1957) 162–164.

[17] J. Bardeen, L. N. Cooper, and J. R. Schrieffer, "Theory of superconductivity," *Phys. Rev.* **108** (Dec, 1957) 1175–1204.

[18] A. A. Abrikosov *J. Exptl. Theoret. Phys. (USSR)* **32** (1957) 1442. [Sov. Phys.–JETP 5, 1174 (1957)].

[19] L. P. Gor'kov *J. Exptl. Theoret. Phys. (USSR)* **36** (1959) 1918. [Sov. Phys.–JETP 9, 1364 (1959)].

[20] N. R. Werthamer, "Theory of a local superconductor in a magnetic field," *Phys. Rev.* **132** (Oct, 1963) 663–668.

[21] L. Tewordt, "Gap equation and current density for a superconductor in a slowly varying static magnetic field," *Phys. Rev.* **132** (Oct, 1963) 595–600.

[22] B. S. Deaver and W. M. Fairbank, "Experimental evidence for quantized flux in superconducting cylinders," *Phys. Rev. Lett.* **7** (Jul, 1961) 43–46.

[23] R. Doll and M. Näbauer, "Experimental proof of magnetic flux quantization in a superconducting ring," *Phys. Rev. Lett.* **7** (Jul, 1961) 51–52.

[24] F. London, *Superfluids, Vol. 1.* John Wiley & Sons, New York, 1950.

[25] B. D. Josephson, "Possible new effects in superconductive tunnelling," *Physics Letters* **1** (1962), no. 7, 251 – 253.

[26] J. R. Gavaler, "Superconductivity in Nb-Ge films above 22 K," *Applied Physics Letters* **23** (1973), no. 8, 480–482.

[27] J. G. Bednorz and K. A. Müller, "Possible high-T_c superconductivity in the Ba-La-Cu-O system," *Zeitschrift fr Physik B Condensed Matter* **64** (1986), no. 2, 189–193.

[28] Y. Kamihara, T. Watanabe, M. Hirano, and H. Hosono, "Iron-based layered superconductor $La[O_{1-x}F_x]FeAs$ ($x = 0.05 - 0.12$) with $T_c = 26K$," *Journal of the American Chemical Society* **130** (2008), no. 11, 3296–3297.

[29] C. Wang, L. Li, S. Chi, Z. Zhu, Z. Ren, Y. Li, Y. Wang, X. Lin, Y. Luo, S. Jiang, X. Xu, G. Cao, and Z. Xu, "Thorium-doping induced superconductivity up to 56K in $Gd_{1-x}Th_xFeAsO$," *EPL (Europhysics Letters)* **83** (2008), no. 6, 67006 (4pp).

[30] M. Tinkham, *Introduction to Superconductivity: Second Edition (Dover Books on Physics).* Dover Publications, June, 2004.

[31] E. Kaxiras, *Atomic and Electronic Structure of Solids.* Cambridge University Press, 1 ed., 2003.

[32] M. K. Wu, J. R. Ashburn, C. J. Torng, P. H. Hor, R. L. Meng, L. Gao, Z. J. Huang, Y. Q. Wang, and C. W. Chu, "Superconductivity at 93K in a new mixed-phase Y-Ba-Cu-O compound system at ambient pressure," *Phys. Rev. Lett.* **58** (Mar, 1987) 908–910.

[33] H. Maeda, Y. Tanaka, M. Fukutomi, and T. Asano, "A new high-T_c oxide superconductor without a rare earth element," *Japanese Journal of Applied Physics* **27** (1988), no. Part 2, No. 2, L209–L210.

[34] Z. Z. Sheng and A. M. Hermann, "Superconductivity in the rare-earth-free Tl-Ba-Cu-O system above liquid-nitrogen temperature," *Nature* **332** (1988) 55–58.

[35] T. P. Devereaux and R. Hackl, "Inelastic light scattering from correlated electrons," *Reviews of Modern Physics* **79** (2007), no. 1, 175.

[36] A. Koitzsch, *Spectroscopic investigation of many-body effects in hole and electron-doped cuprates.* PhD in Physics, Technische Universität Dresden, 2004.

[37] A. Yamanaka, T. Kimura, F. Minami, K. Inoue, and S. Takekawa, "Superconducting gap excitations in Bi-Sr-Ca-Cu-O superconductor observed by raman scattering," *Japanese Journal of Applied Physics* **27** (1988), no. Part 2, No. 10, L1902–L1905.

[38] G. Blumberg, A. Koitzsch, A. Gozar, B. S. Dennis, C. A. Kendziora, P. Fournier, and R. L. Greene, "Nonmonotonic $d_{x^2-y^2}$ superconducting order parameter in $Nd_{2-x}Ce_xCuO_4$," *Phys. Rev. Lett.* **88** (Feb, 2002) 107002.

[39] J. A. Skinta, M.-S. Kim, T. R. Lemberger, T. Greibe, and M. Naito, "Evidence for a transition in the pairing symmetry of the electron-doped cuprates $La_{2-x}Ce_xCuO_{4-y}$ and $Pr_{2-x}Ce_xCuO_{4-y}$," *Phys. Rev. Lett.* **88** (May, 2002) 207005.

[40] J. A. Skinta, T. R. Lemberger, T. Greibe, and M. Naito, "Evidence for a nodeless gap from the superfluid density of optimally doped $Pr_{1.855}Ce_{0.145}CuO_{4-y}$ films," *Phys. Rev. Lett.* **88** (May, 2002) 207003.

[41] C. Kittel, *Introduction to Solid State Physics.* John Wiley & Sons, Inc, 8 ed., 2005.

[42] T. E. Faber and A. B. Pippard *Proc. Roy. Soc. (London)* **A231** (1955) 336.

[43] J. R. Schrieffer, *Theory of superconductivity.* The Benjamin/Cummings Publishing Company, Inc., 3 ed., 1983.

[44] A. Altland and B. Simons, *Condensed Matter Field Theory.* Cambridge University Press, 1 ed., 2007.

[45] I. Giaever, "Energy gap in superconductors measured by electron tunneling," *Phys. Rev. Lett.* **5** (Aug, 1960) 147–148.

[46] L. C. Hebel and C. P. Slichter, "Nuclear spin relaxation in normal and superconducting aluminum," *Phys. Rev.* **113** (Mar, 1959) 1504–1519.

[47] H. Takahashi, K. Igawa, K. Arii, Y. Kamihara, M. Hirano, and H. Hosono, "Superconductivity at 43K in an iron-based layered compound $LaO_{1-x}F_xFeAs$," *Nature* **453** (2008), no. 7193,.

[48] F.-C. Hsu, J.-Y. Luo, K.-W. Yeh, T.-K. Chen, T.-W. Huang, P. M. Wu, Y.-C. Lee, Y.-L. Huang, Y.-Y. Chu, D.-C. Yan, and M.-K. Wu, "Superconductivity in the PbO-type structure α-FeSe," *Proceedings of the National Academy of Sciences* **105** (2008), no. 38, 14262–14264.

[49] X. Wang, Q. Liu, Y. Lv, W. Gao, L. Yang, R. Yu, F. Li, and C. Jin, "The superconductivity at 18K in LiFeAs system," *Solid State Communications* **148** (2008), no. 11-12, 538 – 540.

[50] M. Rotter, M. Tegel, and D. Johrendt, "Superconductivity at 38K in the iron arsenide $Ba_{1-x}K_xFe_2As_2$," *Physical Review Letters* **101** (2008), no. 10, 107006.

[51] H. Kito, H. Eisaki, and A. Iyo, "Superconductivity at 54K in F-free $NdFeAsO_{1-y}$," *Journal of the Physical Society of Japan* **77** (2008), no. 6, 063707.

[52] S. Matsuishi, Y. Inoue, T. Nomura, H. Yanagi, M. Hirano, and H. Hosono, "Superconductivity induced by Co-doping in quaternary fluoroarsenide CaFeAsF," *Journal of the American Chemical Society* **130** (2008), no. 44,.

[53] Y. Mizuguchi, F. Tomioka, S. Tsuda, T. Yamaguchi, and Y. Takano, "Superconductivity at 27K in tetragonal FeSe under high pressure," *Applied Physics Letters* **93** (2008), no. 15, 152505.

[54] K.-W. Yeh, T.-W. Huang, Y. lin Huang, T.-K. Chen, F.-C. Hsu, P. M. Wu, Y.-C. Lee, Y.-Y. Chu, C.-L. Chen, J.-Y. Luo, D.-C. Yan, and M.-K. Wu, "Tellurium substitution effect on superconductivity of the α-phase iron selenide," *EPL (Europhysics Letters)* **84** (2008), no. 3, 37002 (4pp).

[55] A. S. Sefat, R. Jin, M. A. McGuire, B. C. Sales, D. J. Singh, and D. Mandrus, "Superconductivity at 22K in Co-doped $BaFe_2As_2$ crystals," *Physical Review Letters* **101** (2008), no. 11, 117004.

[56] P. L. Alireza, Y. T. C. Ko, J. Gillett, C. M. Petrone, J. M. Cole, G. G. Lonzarich, and S. E. Sebastian, "Superconductivity up to 29K in $SrFe_2As_2$ and $BaFe_2As_2$ at high pressures," *Journal of Physics: Condensed Matter* **21** (2009), no. 1, 012208 (4pp).

[57] M. S. Torikachvili, S. L. Bud'ko, N. Ni, and P. C. Canfield, "Pressure induced superconductivity in $CaFe_2As_2$," *Physical Review Letters* **101** (2008), no. 5, 057006.

[58] D. J. Singh, "Electronic structure and doping in $BaFe_2As_2$ and $LiFeAs$: Density functional calculations," *Physical Review B (Condensed Matter and Materials Physics)* **78** (2008), no. 9, 094511.

[59] D. J. Singh and M.-H. Du, "Density functional study of $LaFeAsO_{1-x}F_x$: A low carrier density superconductor near itinerant magnetism," *Physical Review Letters* **100** (2008), no. 23, 237003.

[60] V. B. Zabolotnyy, D. S. Inosov, D. V. Evtushinsky, A. Koitzsch, A. A. Kordyuk, G. L. Sun, J. T. Park, D. Haug, V. Hinkov, A. V. Boris, C. T. Lin, M. Knupfer, A. N. Yaresko, B. Buchner, A. Varykhalov, R. Follath, and S. V. Borisenko, "Electronic order in iron arsenide superconductors," *Nature* **457** (2009) 569–572.

[61] D. V. Evtushinsky, D. S. Inosov, V. B. Zabolotnyy, A. Koitzsch, M. Knupfer, B. Büchner, M. S. Viazovska, G. L. Sun, V. Hinkov, A. V. Boris, C. T. Lin, B. Keimer, A. Varykhalov, A. A. Kordyuk, and S. V. Borisenko, "Momentum dependence of the superconducting gap in $Ba_{1-x}K_xFe_2As_2$," *Physical Review B (Condensed Matter and Materials Physics)* **79** (2009), no. 5, 054517.

[62] C. Liu, T. Kondo, M. E. Tillman, R. Gordon, G. D. Samolyuk, Y. Lee, C. Martin, J. L. McChesney, S. Bud'ko, M. A. Tanatar, E. Rotenberg, P. C. Canfield, R. Prozorov, B. N. Harmon, and A. Kaminski, "Fermi surface and strong coupling superconductivity in single crystal $NdFeAsO_{1-x}F_x$, url = http://www.citebase.org/abstract?id=oai:arXiv.org:0806.2147, year = 2008."

[63] L. X. Yang, Y. Zhang, H. W. Ou, J. F. Zhao, D. W. Shen, B. Zhou, J. Wei, F. Chen, M. Xu, C. He, Y. Chen, Z. D. Wang, X. F. Wang, T. Wu, G. Wu, X. H. Chen, M. Arita, K. Shimada, M. Taniguchi, Z. Y. Lu, T. Xiang, and D. L. Feng, "Electronic

structure and unusual exchange splitting in the spin-density-wave state of the $BaFe_2As_2$ parent compound of iron-based superconductors," *Physical Review Letters* **102** (2009), no. 10, 107002.

[64] H. Ding, K. Nakayama, P. Richard, S. Souma, T. Sato, T. Takahashi, M. Neupane, Y. M. Xu, Z. H. Pan, A. V. Federov, Z. Wang, X. Dai, Z. Fang, G. F. Chen, J. L. Luo, and N. L. Wang, "Electronic structure of optimally doped pnictide $Ba_{0.6}K_{0.4}Fe_2As_2$: a comprehensive ARPES investigation," 2008.

[65] H. Ding, P. Richard, K. Nakayama, K. Sugawara, T. Arakane, Y. Sekiba, A. Takayama, S. Souma, T. Sato, T. Takahashi, Z. Wang, X. Dai, Z. Fang, G. F. Chen, J. L. Luo, and N. L. Wang, "Observation of fermi-surface-dependent nodeless superconducting gaps in $Ba_{0.6}K_{0.4}Fe_2As_2$," *EPL (Europhysics Letters)* **83** (2008), no. 4, 47001 (6pp).

[66] D. V. Evtushinsky, D. S. Inosov, V. B. Zabolotnyy, M. S. Viazovska, R. Khasanov, A. Amato, H.-H. Klauss, H. Luetkens, C. Niedermayer, G. L. Sun, V. Hinkov, C. T. Lin, A. Varykhalov, A. Koitzsch, M. Knupfer, B. Buchner, A. A. Kordyuk, and S. V. Borisenko, "Momentum-resolved superconducting gap in the bulk of $Ba_{1-x}K_xFe_2As_2$ from combined arpes and μ-SR measurements," *New Journal of Physics* **11** (2009), no. 5, 055069 (13pp).

[67] T. J. Williams, A. A. Aczel, E. Baggio-Saitovitch, S. L. Budko, P. C. Canfield, J. P. Carlo, T. Goko, J. Munevar, N. Ni, Y. J. Uemura, W. Yu, and G. M. Luke, "Muon spin rotation measurement of the magnetic field penetration depth in $Ba(Fe_{0.93}Co_{0.07})_2As_2$: Evidence for multiple superconducting gaps," 2009.

[68] T. Y. Chen, Z. Tesanovic, R. H. Liu, X. H. Chen, and C. L. Chien, "A BCS-like gap in the superconductor $SmFeAsO_{0.85}F_{0.15}$," *Nature* **453** (2008), no. 7199,.

[69] H.-J. Grafe, D. Paar, G. Lang, N. J. Curro, G. Behr, J. Werner, J. Hamann-Borrero, C. Hess, N. Leps, R. Klingeler, and B. Buchner, "^{75}As NMR studies of superconducting $LaFeAsO_{0.9}F_{0.1}$," *Physical Review Letters* **101** (2008), no. 4, 047003.

[70] I. I. Mazin, D. J. Singh, M. D. Johannes, and M. H. Du, "Unconventional superconductivity with a sign reversal in the order parameter of $LaFeAsO_{1-x}F_x$," *Physical Review Letters* **101** (2008), no. 5, 057003.

[71] M. M. Korshunov and I. Eremin, "Theory of magnetic excitations in iron-based layered superconductors," *Physical Review B (Condensed Matter and Materials Physics)* **78** (2008), no. 14, 140509.

[72] A. D. Christianson, E. A. Goremychkin, R. Osborn, S. Rosenkranz, M. D. Lumsden, C. D. Malliakas, I. S. Todorov, H. Claus, D. Y. Chung, M. G. Kanatzidis, R. I. Bewley, and T. Guidi, "Unconventional superconductivity in $Ba_{0.6}K_{0.4}Fe_2As_2$ from inelastic neutron scattering," *Nature* **456** (2008), no. 7224,.

[73] C. T. Chen, C. C. Tsuei, M. B. Ketchen, Z. A. Ren, and Z. X. Zhao, "Integer and half-integer flux-quantum transitions in a niobium/iron-pnictide loop," 2009.

[74] D. Parker, O. V. Dolgov, M. M. Korshunov, A. A. Golubov, and I. I. Mazin, "Extended $s_{\pm}$ scenario for the nuclear spin-lattice relaxation rate in superconducting pnictides," *Physical Review B (Condensed Matter and Materials Physics)* **78** (2008), no. 13, 134524.

[75] C. de la Cruz, Q. Huang, J. W. Lynn, J. Li, W. R. II, J. L. Zarestky, H. A. Mook, G. F. Chen, J. L. Luo, N. L. Wang, and P. Dai, "Magnetic order close to superconductivity in the iron-based layered $LaO_{1-x}F_xFeAs$ systems," *Nature* **453** (2008), no. 899,.

[76] J. Zhao, Q. Huang, C. de la Cruz, S. Li, J. W. Lynn, Y. Chen, M. A. Green, G. F. Chen, G. Li, Z. Li, J. L. Luo, N. L. Wang, and P. Dai, "Structural and magnetic phase diagram of $CeFeAsO_{1-x}F_x$ and its relation to high-temperature superconductivity," *Nat Mater* **7** (2008), no. 12,.

[77] G. F. Chen, Z. Li, D. Wu, G. Li, W. Z. Hu, J. Dong, P. Zheng, J. L. Luo, and N. L. Wang, "Superconductivity at 41K and its competition with spin-density-wave instability in layered $CeO_{1-x}F_xFeAs$," *Physical Review Letters* **100** (2008), no. 24, 247002.

[78] H. Luetkens, H.-H. Klauss, M. Kraken, F. J. Litterst, T. Dellmann, R. Klingeler, C. Hess, R. Khasanov, A. Amato, C. Baines, M. Kosmala, O. J. Schumann, M. Braden, J. Hamann-Borrero, N. Leps, A. Kondrat, G. Behr, J. Werner, and B. Buchner, "The electronic phase diagram of the $LaO_{1-x}F_xFeAs$ superconductor," *Nat Mater* **8** (2009), no. 4,.

[79] X. F. Wang, T. Wu, G. Wu, R. H. Liu, H. Chen, Y. L. Xie, and X. H. Chen, "The peculiar physical properties and phase diagram of $BaFe_{2-x}Co_xAs_2$ single crystals," *New Journal of Physics* **11** (2009), no. 4, 045003 (11pp).

[80] H. Chen, Y. Ren, Y. Qiu, W. Bao, R. H. Liu, G. Wu, T. Wu, Y. L. Xie, X. F. Wang, Q. Huang, and X. H. Chen, "Coexistence of the spin-density wave and superconductivity in $Ba_{1-x}K_xFe_2As_2$," *EPL (Europhysics Letters)* **85** (2009), no. 1, 17006 (5pp).

[81] R. H. Liu, T. Wu, G. Wu, H. Chen, X. F. Wang, Y. L. Xie, J. J. Ying, Y. J. Yan, Q. J. Li, B. C. Shi, W. S. Chu, Z. Y. Wu, and X. H. Chen, "A large iron isotope effect in $SmFeAsO_{1-x}F_x$ and $Ba_{1-x}K_xFe_2As_2$," *Nature* **459** (2008), no. 7243,.

[82] K. Haule, J. H. Shim, and G. Kotliar, "Correlated electronic structure of $LaO_{1-x}F_xFeAs$," *Physical Review Letters* **100** (2008), no. 22, 226402.

[83] I. I. Mazin and J. Schmalian, "Pairing symmetry and pairing state in ferropnictides: Theoretical overview," 2009.

[84] M. V. Klein and S. B. Dierker, "Theory of raman scattering in superconductors," *Phys. Rev. B* **29** (May, 1984) 4976–4991.

[85] T. Strohm and M. Cardona, "Electronic raman scattering in $YBa_2\,Cu_3\,O_7$ and other superconducting cuprates," *Phys. Rev. B* **55** (May, 1997) 12725–12735.

[86] F. Schwabl, *Advanced Quantum Mechanics.* Springer-Verlag, 3 ed., 2005.

[87] T. Tsuneto, "Transverse collective excitations in superconductors and electromagnetic absorption," *Phys. Rev.* **118** (May, 1960) 1029–1035.

[88] R. Sooryakumar and M. V. Klein, "Raman scattering by superconducting-gap excitations and their coupling to charge-density waves," *Phys. Rev. Lett.* **45** (Aug, 1980) 660–662.

[89] S. B. Dierker, M. V. Klein, G. W. Webb, and Z. Fisk, "Electronic raman scattering by superconducting-gap excitations in Nb_3Sn and V_3Si," *Phys. Rev. Lett.* **50** (Mar, 1983) 853–856.

[90] R. Hackl, R. Kaiser, and W. Glser, "Electronic and phonon-mediated gap modes in A15 compounds," *Physica C: Superconductivity* **162-164** (1989), no. Part 1, 431 – 432.

[91] G. Blumberg, A. Mialitsin, B. S. Dennis, M. V. Klein, N. D. Zhigadlo, and J. Karpinski, "Observation of leggett's collective mode in a multiband MgB_2 superconductor," *Physical Review Letters* **99** (2007), no. 22, 227002.

[92] A. J. Leggett, "Number-phase fluctuations in two-band superconductors," *Progress of Theoretical Physics* **36** (1966), no. 5, 901–930.

[93] M. Rotter, M. Pangerl, M. Tegel, and D. Johrendt, "Superconductivity and crystal structures of $(Ba_{1-x}K_x)Fe_2As_2(x = 0 - 1)$," *Angewandte Chemie International Edition* **47** (2008), no. 41,.

[94] A. V. Chubukov, I. Eremin, and M. M. Korshunov, "Theory of raman response of a superconductor with extended s-wave symmetry: Application to the iron pnictides," *Physical Review B (Condensed Matter and Materials Physics)* **79** (2009), no. 22, 220501.

[95] M. V. Klein, "Shining light on iron pnictides with raman scattering," *Physics* **2** (Jun, 2009) 46.

[96] G. R. Boyd, T. P. Devereaux, P. J. Hirschfeld, V. Mishra, and D. J. Scalapino, "Probing the pairing symmetry of the iron pnictides with electronic raman scattering," *Physical Review B (Condensed Matter and Materials Physics)* **79** (2009), no. 17, 174521.